ANNUAL REPORT

to

National Aeronautics and Space Administration

covering research under NASA Grant

NGL 22-009-187

A STUDY OF LUNAR MODELS BASED ON APOLLO AND OTHER DATA

in the

Department of Earth and Planetary Sciences
Massachusetts Institute of Technology
Cambridge, Massachusetts 02139

for the period

1 March 1972 - 28 February 1973

TABLE OF CONTENTS

TABLE OF CONTENTS (cont.)

INTRODUCTION

This NASA Grant (NGL 22-009-187) covers the support of several MIT faculty members and some of their graduate students in research efforts concerned with the Moon. Primary emphasis is on the interpretation of lunar data developed during the Apollo Program with additional data being used as needed for greater understanding. The Attached Annual Report (covering the period 1 March 1972 through 28 February 1973) is presented in mixed form, including both finished papers and brief progress reports describing the efforts of various individuals being supported by the grant.

X-RAY EMISSION SPECTRA AND MOLECULAR ORBITAL BONDING MODELS OF LUNAR MATERIALS

by

J.A. Tossell, D.J. Vaughan and R.G. Burns

Objectives

The aim of the project is to calculate the electronic structures of important coordination polyhedra occurring in lunar minerals. These include the SiO_4^{-4} tetrahedron in olivines, the $Si_2O_7^{-6}$ group in pyroxenes, the MgO_6^{-10} and FeO_6^{-10} octahedra in ferromagnesian silicates and the FeO_4^{-4} tetrahedron in spinels. We plan to extend the computations to the TiO_6^{-9} and CrO_6^{-10} octahedra (containing Ti^{3+} and Cr^{2+}) believed to occur in the ferromagnesian silicate minerals which crystallized under very low oxygen fugacities on the moon. From accurate molecular orbital (MO) calculations, the energies (wavelengths) at which allowed and forbidden crystal-field bands, as well as metal-metal and metal-oxygen charge transfer transitions, occur may be predicted. Consequently, absorption spectral assignments may be clarified and information obtained on the oxidation states and crystal chemistry of Fe,Ti and Cr in lunar and terrestrial minerals.

A second approach has been to measure the soft x-ray emission spectra of Fe, Ti and Cr in lunar and terrestrial minerals. The positions of the peaks in the x-ray spectra not only can be predicted from the MO calculations and serve as a check on their validity, but they also provide an independent method for determining the oxidation states and coordination numbers of the elements in the lunar minerals. We have obtained excellent results for iron in terrestrial and lunar minerals, and are currently extending the measurements to Ti and Cr.

Molecular Orbital Project

J.A. Tossell
and
D.J. Vaughan

The molecular orbital (MO) interpretation of the x-ray emission spectra of minerals has been placed on a firm quantitative basis by a series of calculations on the spectra of Mg, Al and Si oxides. This work has resulted in two publications and one abstract, copies of which are enclosed. Our current work employs a new MO method for the study of oxidic minerals of both transition and non-transition metals. Our first paper using this method, on the spectra and electronic structure of quartz, is enclosed.

J. Phys. Chem. Solids 33 P1 Pergamon Press. Printed in Great Britain

MOLECULAR ORBITAL INTERPRETATION OF X-RAY EMISSION AND ESCA SPECTRAL SHIFTS IN SILICATES*

J. A. TOSSELL
Department of Earth and Planetary Sciences, 54-819, Massachusetts Institute of Technology, Cambridge, Mass. 02139, U.S.A.

(*Received* 27 *April* 1972)

Abstract—An approximate molecular orbital theory is presented, tested, and applied to silicon and aluminum oxyanions. The orbital structure of SiO_4^{-4} is calculated and is used to assign the X-ray emission spectra. Calculations are performed at several internuclear distances and semiquantitative agreement is found with experimentally observed trends in Al$K\alpha$ and Si$K\beta$ spectra. Calculations on $Si_2O_7^{-6}$ and $AlSiO_7^{-7}$ yield fair agreement with experimental trends relating to degree of SiO_4 polymerization and to Al/Si ratio. Charges for bridging and non-bridging oxygens in $Si_2O_7^{-6}$, combined with point charge potentials from metal ions in the orthopyroxene structure yield Ols binding energies in agreement with ESCA results.

1. INTRODUCTION

IN RECENT years molecular orbital (MO) theory has found increasing application in geochemistry. The need for using MO theory in the description of covalent minerals, such as sulfides, has been recognized for some time [1]. The application of MO theory to minerals generally considered to be ionic, such as oxides and silicates, has only recently become common[2–4].

A related development is the increased use of MO theory in solid state science generally, and particularly in X-ray spectroscopy. Several authors have suggested that the MO model is more appropriate than the atomic or band model for the interpretation of X-ray emission and absorption spectra[5–7]. Qualitative MO diagrams have been used to assign X-ray transitions and the experimental transition energies have then been employed to determine quantitative MO diagrams empirically. This procedure has been used extensively for compounds of the transition elements.

For $K\alpha$ spectra in compounds of the third period elements, ionic models have been used to relate experimental line shifts to effective atomic charges[8], with little use being made of MO theory since the $K\alpha$ transition presumably involves orbitals which are purely atomic. MO theory has been used qualitatively to assign $K\beta$ spectra in such compounds and to relate shifts in spectral lines to changes in bonding energies. $K\beta$ satellite lines have also been interpreted using MO theory. A large amount of information on the shift of X-ray lines with average interatomic distance and with the type of silicate linkage in silicates and aluminosilicates is available[9, 10] but has not yet been interpreted theoretically.

The only quantitative MO calculations previously applied to X-ray spectroscopy are those of Manne on sulfur and chlorine oxyanions[11, 23]. The care with which Manne treated core orbitals and the general adequacy of his method resulted in good agreement with experiment for $K\alpha_{1,2}$ shifts if the relaxation of the core ion states involved in the X-ray transition was taken into account. Recent *ab initio* self-consistent field (SCF) calculations[12] on the sulphate ion have yielded results similar to those of Manne. Although

*This work was supported in part by the National Aeronautics and Space Administration.

lines 3&4 should read
photoelectron spectra (PES) for SO_4^{-2} and
the other oxyanions he could not obtain

JCS 3971 P2.

Manne also considered the ESCA (Electron Spectroscopy for Chemical Analysis) or photoelectron spectra (PES) and the other oxyanions data for SO_4^{-2} he could not obtain any conclusive results due to a number of uncertainties in both the experimental situation and the theoretical model.

In this paper we present approximate non-empirical MO calculations on several silicate compounds. Our goal is to obtain knowledge about bonding in silicates and to reproduce and interpret trends in X-ray and ESCA transition energies. We present first the theory, then details of the computation, and finally our results.

2. THEORY

The present approximate MO calculations employ a method incorporating elements of the CNDO/2 method of Pople and Segal[13] and the NEMO method of Newton *et al.*[14]. The formulas used for diagonal and off-diagonal elements of the Fock–Hamiltonian (F matrix) are

$$F_{ii} = F_{ii}^{\circ} + \sum_{j \text{ on } A} \Delta P_j \left((\bar{i}\bar{i}|\bar{j}\bar{j}) - .5(\bar{i}\bar{j}|\bar{i}\bar{j}) \right) + \sum Q_B R_{AB}^{-1} \quad (1)$$

$$F_{ij} = T_{ij} + K_{ij} S_{ij} (U_{ii} + U_{jj})/2. \quad (2)$$

where F_{ii}° is the diagonal element for a free atom or ion with a specified electronic configuration, obtained from an atomic SCF calculation, ΔP_i is the change in the Mulliken orbital population of Slater orbital j, $(\bar{i}\bar{i}|\bar{j}\bar{j})$ and $(\bar{i}\bar{j}|\bar{i}\bar{j})$ are rotationally averaged one center Coulomb and exchange integrals, Q_B is the Mulliken charge of atom B, U_{ii} is the rotationally averaged element of the potential energy matrix and T_{ii} and S_{ij} are the kinetic energy and overlap integrals. The first equation is similar to that of [13] while (2) is obtained from [14]. The overlap, kinetic energy and one center electron repulsion integrals are calculated accurately and the K_{ij} parameters are obtained from *ab initio* SCF calculations on related molecules. This method is very similar to one presented by Hillier[15] and applied to SO_4^{-2}. However our method is wholly *non-empirical*, using non-empirical parameters in calculating the off-diagonal terms and non-empirical quantities in the diagonal terms. Also *all* electrons are included explicitly (and treated equivalently) and full self-consistency is required.

To test our method and programming we carried out a calculation on the SO_4^{-2} ion. Best atom minimum basis set exponents[16] were used. One center K's were taken from atomic SCF calculations and two center K's for the S–O bond were assigned values from an *ab initio* SCF calculation on PO (phosphorous monoxide)[17]. Calculations on the hydrides SiH_4[18], PH_3[17], H_2S[18] have shown that there is very little variation of either one center or two center K_{ij}'s within such a series. This suggests that a single set of K's will give reasonable results for the series SiO_4^{-4}, PO_4^{-3}, SO_4^{-2}. Also, other SCF calculation[19] have indicated relatively little K variation with charge, electronic configuration, internuclear distance or orbital exponent. Results were compared with *ab initio* minimum basis set[12a] and various approximate calculations[20]. The average absolute error of our valence orbital eigenvalues with respect to those of [12a] is 0·12 AU, very similar to that in Manne's calculation, with our values being systematically too positive. The average relative error in the numerical ordering of the MO's is only 0·05 AU. Inspection of the tabulated comparison of various methods given in [20] and reproduced with our addition in Table 1 shows that our method, as well as those of Manne and Hillier, give results similar to the minimum basis set *ab initio* calculation. Extended basis set calculations yield the opposite ordering for $1t_1$ and $5t_2$. Correct MO orderings are then obtained except for the $1c_1$ and $5t_2$ using all three methods. Although our method yields eigenvalues for 'core' orbitals, comparison

JACS 3994 P3 X-RAY EMISSION AND ESCA SPECTRAL SHIFTS

Table 1. Eigenvalues of SO_4^{-2} valence molecular orbitals using various methods

	Present method	*Ab initio* SCF[a]	Approx. MO[b]	SCC-LCAO[c]	EHMO[d]
$1t_1$	0·371	0·266	0·152	−0·070	−0·323
$5t_2$	0·434	0·270	0·122	−0·068	−0·306
$1e$	0·296	0·204	0·093	−0·105	−0·352
$4t_2$	0·019	−0·029	−0·216	−0·260	−0·426
$5a_1$	−0·002	−0·122	−0·276	−0·298	−0·294
$3t_2$	−0·512	−0·684	−0·634	−0·806	−0·991
$4a_1$	−0·718	−0·933	−0·848	−1·118	−1·138

[a]Ref. [12a].
[b]Ref. [11].
[c]Ref. [15] self-consistent charge LCAO.
[d]Ref. [20b] extended Hückel MO, better results have been obtained using the non-self consistent EHMO method Ref. [31].

with the *ab initio* results is not appropriate since they were obtained using Gaussian orbitals which yield poor energies for inner shells. A possible difficulty in our calculations is a somewhat exaggerated charge separation as illustrated by a S charge of 3·2 in SO_4^{-2}.

Computational model and details

The compounds we discuss in this paper involve Si coordinated with oxygen. We first present calculations on the perfect tetrahedral anion SiO_4^{-4} for various Si–O distances. A best atom minimum basis set (BA MBS) of Slater orbitals is used and K's are again taken from atomic SCF results and from PO. Calculations were assumed to have converged when the average F_{ii} variation was $< 0{\cdot}005$ AU. This required 4 or 5 cycles.

Some controversy has surrounded the use of $3d$ orbitals in MO calculations on third period compounds. We have chosen to neglect $3d$ orbitals for the following reasons: (1) comparison with accurate SO_4^{-2} calculations showed our method to give significantly poorer agreement when $3d$ orbitals were included. (2) use of a $3d$ function with a minimum s, p set exaggerates d orbital participation. (3) d orbitals are not needed for an adequate description of most properties of SO_4^{-2}. (4) an increase in the basis set size would increase computation time and severely limit the size of systems to be studied. From the *ab initio* calculation[12a] and the qualitative work of Cruickshank[21] we would expect the neglect of d orbitals to have a strong energetic effect only on MO's of e symmetry, although some d orbital participation in the higher t_2 orbitals is indicated by the L spectra of second-row oxyanions[22].

Orbital structure of SiO_4^{-4}

Eigenvalues and orbital composition for the SiO_4^{-4} unit are given in Table 2. The orbital structure is similar to that for SO_4^{-2}. As noted earlier our method does not obtain the proper ordering of the $5t_2$ and $1t_1$ orbitals in SO_4^{-2} and this ordering is presumably incorrect in SiO_4^{-4} as well. The inverted ordering of the $5a_1$ and the $4t_2$ in SiO_4^{-4} is also doubtful although some shift in this direction may occur. The valence orbitals fall into three groups: (1) $4a_1$ and $3t_2$; O2$_s$ (2) $4t_2$ and $5a_1$; σ bonding orbitals: (3) $1e$, $1t_1$, $5t_2$; non-bonding orbitals. The electronic configuration expressed as Mulliken orbital populations is Si(core)^{10} $3s^{0.39}$ $3p^{1.06}$ O(core)^2 $2s^{2.03}$ $2p^{5.62}$ silicon and oxygen.

should be caps same as Intro. and Theory

X-ray transitions

The quantitative MO results of Table 2 may be used to assign transitions in the X-ray

Table 2. Eigenvalues and orbital compositions of filled orbitals for SiO_4^{-4} (R(Si–O) = 1·603 Å)

i	ϵ_i(AU)	% composition
$5t_2$	1·07332	1% Si3p, 99% O2p
$1t_1$	1·02677	100% O2p
$1e$	0·96229	100% O2p
$5a_1$	0·85682	17% Si3s, 1% O2s 82% O2p
$4t_2$	0·84077	19% Si3p, 71% O2p
$3t_2$	0·18179	3% Si3p, 97% O2s
$4a_1$	0·11357	3% Si3s, 97% O2s
$2t_2$	−3·22745	99% Si2p, 1% Si3p
$3a_1$	−5·04019	100% Si2s
$1t_2$	−18·67688	100% O1s
$2a_1$	−18·67705	100% O1s
$1a_1$	−67·98569	100% Si1s

JPCS 399 P14. J. A. TOSSELL

spectra of Si and O in silicates. MO theory has previously been used for this purpose by Urch[6] and by Andermann and Whitehead [23]. X-ray spectra are produced by transitions from a higher level to an inner shell vacancy and may be classified as K, L or M depending upon the inner shell involved. The K_α line arises from the transition $2p \rightarrow 1s$ and the Si$K\alpha$ energy is thus given by the difference of the $2t_2$ and $1a_1$ eigenvalues in Table 2. Due to the approximate nature of the calculation and to the neglect of the important relaxation effects associated with core ion states agreement of the calculated absolute value of transition energy with experiment is only approximate. For example, we calculate $E_{SiK\alpha}$ as ~ 1761 eV while experiment gives ~ 1740 eV. (see the Appendix for further discussion). Therefore we will consider only the relative energies of the spectral transitions.

SiK_β

The SiK_β spectra nominally involve the transition $3p \rightarrow 1s$. In fact several bands in the K_β region are observed and by the dipole selection rules for tetrahedral geometry all molecular orbitals of t_2 symmetry can take part in the transitions. In SiO_2 three such transitions are observed, the main transition being called K_β and the lower energy transition K'_β. Table 3 contains experimental and calculated energies and intensities relative to K_β for SiO_2. The K_β and K'_β experimental values are taken from Urch[6] while the position and approximate intensity of the higher energy peak are obtained from the figures of Dodd and Glenn. Relative intensities are calculated in a simple way from the relative $3p$ percentage compositions of $3t_2$, $4t_2$ and $5t_2$ in Table 2, thus ignoring 'cross-over' contributions (e.g. O$2p \rightarrow$ Sil$s$) which Urch has shown to give a

Table 3. Experimental and calculated energies (eV) and intensities of SiK_β, Si$L_{2,3}$ and OK_α spectral components for tetrahedral Si–O coordination

SiK_β					
	Exper.[b]			Calculated[a]	
K_β	ΔE	I	Assignment	ΔE	I
	−13·7, −14·4	15–20	$3t_2 \rightarrow 1a_1$	−17·9	16
K_β	0	100	$4t_2 \rightarrow 1a_1$	0	100
shoulder	+5	~ 1–5	$5t_2 \rightarrow 1a_1$	6·3	5

Si$L_{2,3}$					
	Exper.[c]			Calculated	
ΔE		I	Assignment	ΔE	I
0		20–25	$4a_1 \rightarrow 2t_2$	0	18
12		100	$5a_1 \rightarrow 2t_2$	20·2	100
~ 17		~ 90	$1e, 5t_2 \rightarrow 2t_2$	22·9, 25·7	0, 42

OK_α					
	Exper.[d]			Calculated	
ΔE		I	Assignment	ΔE	I
0			$5t_2 \rightarrow (1t_2, 2a_1)$	0	99
−1·0		4	$1t_1 \rightarrow (1t_2, 2a_1)$	−1·2	100
−2·8			$1e \rightarrow (1t_2, 2a_1)$	−3·0	67
−5·8		1	$5a_1 \rightarrow (1t_2, 2a_1)$	−5·9	27
			$4t_2 (1t_2, 2a_1)$	−6·3	71

[a] SiO_4^{-4}, R = 1·603.
[b] Ref. [2] and [6].
[c] Ref. [22].
[d] Ref. [3].

small intensity. Manne[24] has shown this approach to give good results for hydrocarbons. Agreement of calculation and experiment is fairly good. We do not find it necessary to invoke a symmetry forbidden transition from the $2e$ as did Dodd and Glenn[2] in order to explain the high energy shoulder. Our assignment is supported by the results of calculations using the same method and BA MBS exponents on isoelectronic AlO_4^{-5}. The calculated separation of main K_β peak and high energy shoulder is about 1·6 eV less in AlO_4^{-5} than in SiO_4^{-4}, in agreement with the difference of 1·5 eV in separation observed between quartz and cordierite[32].

OK_α

OK_α spectra arise from $O2p \rightarrow O1S$ transitions. The upper orbitals contributing to OK_α are $4t_2$, $5a_1$, $1e$, $1t_1$ and $5t_2$. Table 3 gives calculated energies and intensities for the OK_α spectrum obtained in the same way as for the SiK_β. In this table the highest energy component is assumed to arise from $5t_2$ although the $1t_1$ may well lie higher. Agreement with the K_α structure as discussed by Urch is fairly good. A broad peak is found resulting from transitions from the non-bonding predominantly $O2p$ orbitals and a lower energy peak results from the σ bonding orbitals. The assignment of Urch also mentions an expected line at about 4 eV lower energy which has not been observed. Urch assigns this observed peak to the $5a_1$, but we find $4t_2$ and $5a_1$ to be so close in energy that they would generate only a single peak. The calculated intensity ratio for the two bands in the K_α spectra, summed over components, is approximately 2·7/1, somewhat smaller than experiment. We note that our MO diagram is not in agreement with that of O'Nions and Smith[3]. We feel that the high energy peak at 531 eV in [3] cannot be accomodated on a conventional MO diagram; it probably arises from doubly ionized atoms[24]. On the other hand if this peak is ignored, agreement of our calculations with O'Nions and Smith's reported spectra is good, as shown in Table 3.

$SiL_{2,3}$

$SiL_{2,3}$ spectra nominally involve the transitions Si $3s$, $3d \rightarrow$ Si$2p$. The upper levels involved are $4a_1$, $5a_1$ in our MO scheme, both having some Si$3s$ character. Clearly d orbital participation is required in this case to give the three or four strong lines observed.

Using our SiO_4^{-4} results in conjunction with the *ab initio* s, p, d results of Gelius *et al.* for SO_4^{-2} we can suggest the assignment of the peaks which is given in Table 3. We assign the low energy peak to $4a_1$ and the middle peak to $5a_1$. The peak at higher energy must then be assigned to $1e$ and/or $5t_2$. In the *ab initio* calculation on SO_4^{-2} substantial d orbital populations were found in $1e$ and $5t_2$. Our interpretation is also generally consistent with an *ab initio* SCF calculation on SiO_4^{-4}, currently in press[25].

Earlier MO assignments of the L spectra of S and Cl oxyanions ignored intensity considerations and claimed agreement of calculated L spectra with experiment using an s, p MO calculation[23]. However, although d orbital participation may not drastically affect the eigenvalues of the $1e$ and $5t_2$ orbitals it will drastically affect the intensity of the L spectral lines generated by them and so an s, p basis cannot yield both correct energies and correct intensities for Si $L_{2,3}$ spectra.

This is seen in the $L_{2,3}$ intensities calculated in Table 3. The intensity ratios of the two lower energy transitions were obtained from the %Si$3s$ character in $4a_1$ and $5a_1$. To obtain any intensity for the high energy peak we had to consider the elements of the dipole moment operator connecting the Si$2p$ and $O2p$ orbitals. These integrals were calculated accurately and we found the $O2p\sigma$ electrons of $5t_2$ to generate a transition ~ 42 per cent as intense as that from the $5a_1$. The intensity from the $O2p\pi$ orbitals of $1e$ was essentially zero. Our $L_{2,3}$ intensities are then in poor agreement with experiment, although the

energies are quite good. The poor intensities are clearly due to the neglect of d orbitals in our calculation.

Experimental and calculated variation of E_{SiK_α} and E_{SiK_β} with R(Si–O)

Calculations at the level of the present work are more appropriately applied to the study of trends in a series of similar compounds than to the calculation of absolute values of a quantity in a single compound. Therefore we have studied the variation of K spectral energies with variation of several different experimental quantities. We first varied R(Si–O) for tetrahedral SiO_4^{-4}. Trends in $E_{K\beta}$ are displayed in Fig. 1(b). The variation in $E_{K\alpha}$ is about $+5{\cdot}5 \times 10^{-4}$ AU/0·01 Å. Studies of SiK_α spectra by Koffman and Moll[26] have shown no discernable variation in $E_{SiK\alpha}$ over a large range of compounds. On the other hand Wardle and Brindley[10] have found E_{AlK_α} to increase as R(Al–O) increases in both tetrahedral and octahedral coordination. Their experimental slope of $E_{AlK\alpha}$ vs R(Al–O) for Al in Td coordination (R(Al–O) ~ 1·7–1·8) is $3\text{–}4 \times 10^{-4}$ AU/0·01 Å. We performed calculations for AlO_4^{-5}, analogous to those for isoelectronic SiO_4^{-4}, at R(Al–O) = 1·70, 1·75, 1·80 and obtained a slope of 5×10^{-4} AU/0·01 Å so that our agreement with experiment is good for $E_{AlK\alpha}$. Experimental and calculated $AlK\alpha$ results are given in Fig. 1(a). The SiK_α results will be discussed further later in this paper.

At this point we note for convenience that in the SiK_β energy range a variation of 1×10^{-4} Å in wavelength is closely equivalent to an energy difference of 0·001 AU. In the work of White and Gibbs on K_β shifts in silicates[9a] SiK_β shifts were given relative to SiO_2 (α-quartz) in units of 1×10^{-4} Å (their Δ scale). They found E_{SiK_β} to increase rapidly as R(Si–O) av increased and fitted a straight line to their plot of Δ vs R(Si–O). We feel that their plot of Δ vs R(Si–O) fails to distinguish between two separable, although related, factors which affect E_{SiK_β}: (1) R(Si–O) and (2)

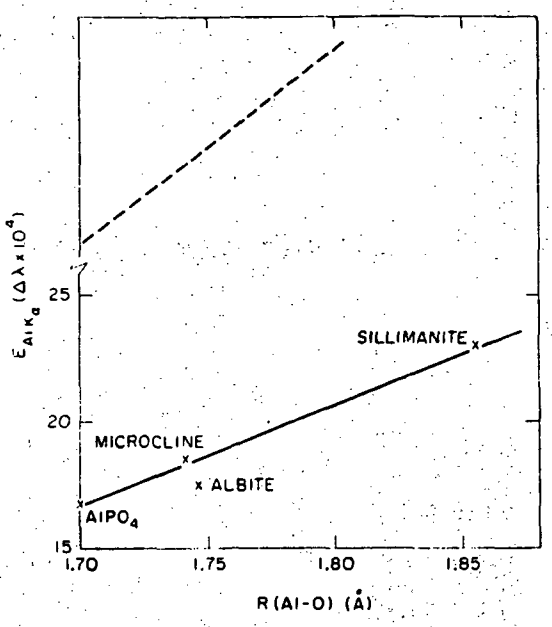

Fig 1A

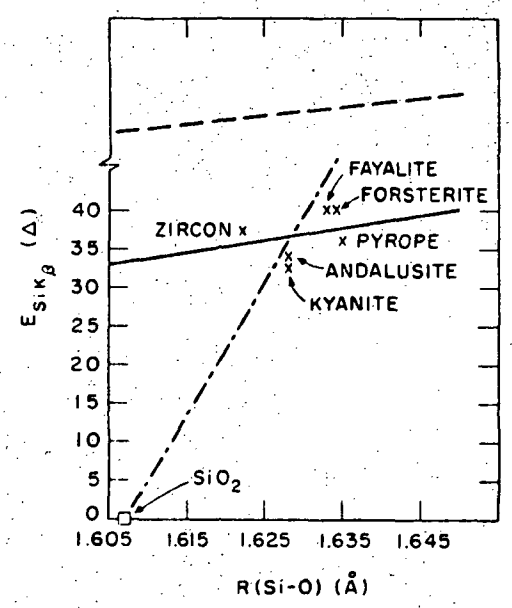

Fig 1B

Fig. 1. (a) Experimental E_{AlK_α} data from [10] compared with calculation. ——— experimental – – – calculation. (b) Experimental E_{SiK_β} data from [9a] compared with calculation. The zircon value of R(Si–O) is 1·6222 Å, the recently refined value of [30]. ——— new isolated tetrahedra line – – – calculation – – – original line from [9a].

the degree of polymerization of the silicate tetrahedra. We have therefore replotted their data for their isolated tetrahedra minerals only and obtained a line with a slope of ~ 1·4 Δ/0·01 Å (0·0014 AU/0·01 Å), much smaller than the slope of their original line. Over the range R(Si–O) = 1·643–1·603 Å we calculate a slope for K_β of 1·1 Δ/0·01 Å, in good agreement with the new line. This is shown in Fig. 1(b).

Since Al^{+3} minerals are substantially more complex than those of Si^{+4}, at the present time we must generally ignore them. However, we note that the slope of E_{SiK_β} with R(Al–O) in octahedral coordination is the same as that of $ESiK_\beta$ with R(Si–O) for silicon in tetrahedral coordination[9b]. We would expect Al or Si in octahedral or tetrahedral coordination to behave similarly and we have found similar K_α and K_β trends in calculations on Si and Al oxides in tetrahedral and octahedral coordination.

Calculated variation of E_{SiK_β} with degree of polymerization and with Al/Si ratio

An accurate determination of the E_{SiK_β} shift with degree of polymerization is impossible at this time, since very large polymeric systems would necessarily have to be considered. We can however perform a calculation for the smallest fragment of the linearly polymerized $(SiO_3)_n$ chain, i.e. $Si_2O_7^{-6}$. E_{SiK_β} values are given for several geometries in Table 4. For these calculations we generally find E_{SiK_β} to be lowered from its SiO_4^{-4} value. In this $C2_v$ system seven non-degenerate '$4t_2$-like' orbitals contribute to the transition and we must weight their eigenvalues by their per cent Si3p character to obtain an average E_{SiK_β}. The energy splitting of these '$4t_2$-like' orbitals in $Si_2O_7^{-6}$ is substantial. The energies of the resulting K_β spectral transitions are shown in Fig. 2 along with the %Si3p character of the orbitals. A later paper will discuss the splitting of the '$4t_2$-like' orbitals in more detail. The variation of E_{SiK_β} with $\theta \equiv \angle$ Si–O_{br}–Si is quite simple. Figures 3(a) and (b) and Table 4

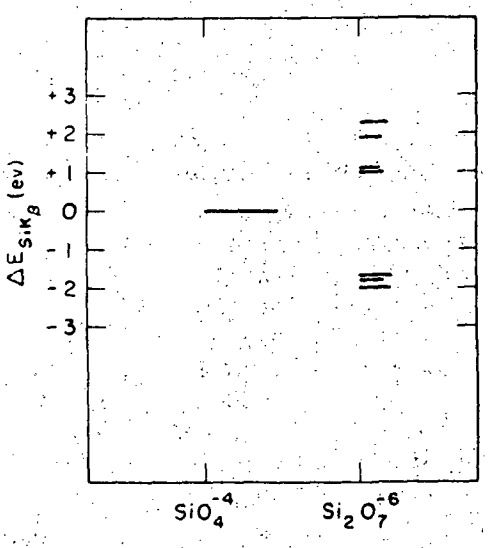

Fig. 2. Energies of SiK_β transitions in SiO_4^{-4} and $Si_2O_7^{-6}$ R(Si–O) = 1·603; θ = 141°.

Table 4. Values of E_{SiK_β} and related quantities for SiO_4^{-4}, $Si_2O_7^{-6}$ and $AlSiO_7^{-7}$

	SiO_4^{-4}		$Si_2O_7^{-6}$		R(Si–O) = 1·603		$Si_2O_7^{-6}$ $R(Si–O_{nbr}) = 1·603$ $R(Si–O_{br}) = 1·623$	$AlSiO_7^{-7}$
	R = 1·603	1·643	θ = 120°	141°	160°	180°		
ΔE_{SiK_β}	0	0·004	0·0066	−0·0033	−0·0057	−0·0018	−0·0030	0·0366
ΔE_{SiK_α}	0	0·0022	0·0033	0·0035	0·0021	0·0010	0·0026	0·0158
Q(Si)	2·582	2·328	2·666	2·664	2·664	2·653	2·631	2·664
m(Si–O_{br})	—	—	0·091	0·096	0·097	0·090	0·096	0·196
$1/2 \sum n_i \epsilon_i$	—	—	−268·64	−269·05	−269·14	−268·88	−269·19	

Energies are in AU.
m(Si–O_{br}) is a mulliken overlap population between Si and O_{br}.
All O_{br}–Si–O_{nbr} are

This figure contains an error. Newsprint is enclosed JPCS 397 PB

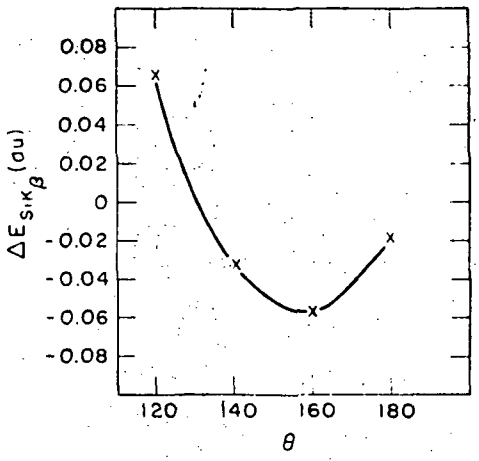

Fig. 3(a). Variation of $E_{SiK\beta}$ with θ (AU with respect to SiO_4^{-4}).

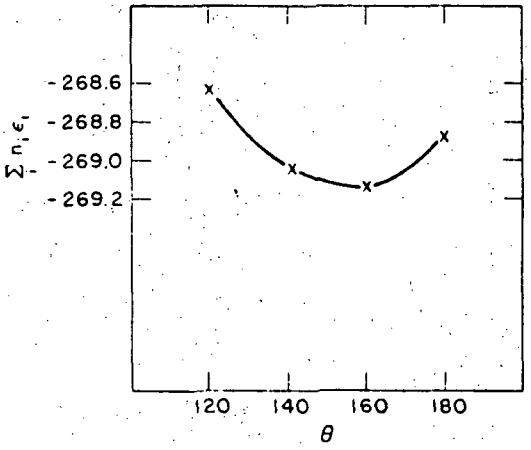

Fig. 3(b). Variation of $\sum n_i\epsilon_i$ with θ (AU).

show that E_{SiK_β} varies with θ in the same way as does the sum of the MO eigenvalues. Both quantities have a minimum near $\theta = 160°$ when all Si–O bond lengths are constrained to be 1·603 Å. For $\theta = 160°$ the lowering of E_{SiK_β} is about lending support to the hypothesis that the degree of polymerization is an important variable influencing E_{SiK_β} A very approximate formula for the K_β shift of a silicate relative to α-SiO_2 can then be given (in Δ units) as

$$\Delta E_{SiK_\beta} = 100\{R(\text{Si–O})_{\text{Av}}^{\text{silicate}} - 1{\cdot}607\}A + (4 - n_{\text{Obr}}^{\text{silicate}})B \quad (3)$$

where $n_{\text{Obr}}^{\text{silicate}}$ is the number of oxygens involved in bridging bonds in the silicate. Our calculations yield A and B values of about 1 and 3–6 respectively. The correlation of the eigenvalue sum with the eigenvalue of the $4t_2$ valence orbital is expected and is consistent with the interpretation of Dodd and Glenn[2]. To determine the relation of the eigenvalue sum to the total energy would require further calculations since the total SCF energy is given by the expression

$$E = E_{NR} + \sum_i n_i\epsilon_i + \sum_i n_i H_i \quad (4)$$

where E_{NR} is the nuclear-nuclear repulsion energy and H_i is the one electron energy ($H = T + V$) for MO i. Assuming that eigenvalue sums parallel total energies for variations of θ the results of Table 4 are consistent with the known relationship between R(Si–O_{br}) and θ [4]. Bridging oxygen bond lengths are generally larger than those for non-bridging oxygens. As R(Si–O_{br}) decreases toward non-bridging values θ increases. Therefore, if all Si–O bond lengths are set equal we would expect θ to increase from the value of 141° which results from linkage of two SiO_4^{-4} tetrahedra without any O–Si–O angular distortion. The calculated minimum energy value of 160° is quite reasonable. In later calculations we hope to explore the relationship between bond length and θ in more detail.

We find E_{SiK_α} to increase by about 0·003 AU in going from SiO_4^{-4} to $Si_2O_7^{-6}$, consistent with the higher Si charge, although E_{SiK_α} decreased as the silicon charge increased for R variation in SiO_4^{-4}. This suggests an explanation for the different behavior of E_{K_α} for Si and Al. For Si the variation of R(M–O) is quite small and smaller values of R are associated with increased polymerization. The effects of reduced R(Si–O) and increased polymerization on E_{SiK_α} are in opposite directions and tend to cancel. For Al the R(M–O) variation is considerably larger and its linkage to polymerization is more complex but generally in

the opposite direction, so that a clear trend in E_{AlK_α} results. For E_{SiK_β} the trends are additive and therefore substantial E_{K_β} variation is observed.

A final trend observed in SiK_β spectra is an increase in E_{SiK_β} with an increase in Al/Si ratio. For a $AlSiO_7^{-7}$ unit with $R(Al-O) = 1{\cdot}70$ and $R(Si-O) = 1{\cdot}603$ we find E_{SiK_β} to be raised in energy by about 37Δ with respect to SiO_4^{-4}. The variation found by White and Gibbs between framework aluminosilicates with Al/Si = 0 and those with Al/Si = 1 is about 25Δ. Our calculations therefore somewhat exaggerate the effect of Al substitution but give a trend of reasonable magnitude. The mixing of the Si3*p* orbitals with the higher energy Al3*p* orbitals is the reason for this result.

Some experimental data on SiK_β spectra also exists for a high pressure polymorph of SiO_2, stishovite, with Si in six-fold coordination in a framework structure. Calculations for the octahedral species SiO_6^{-8} will be discussed in detail in a later publication. We note here that E_{SiK_β} for SiO_6^{-8} at $R(Si-O) = 1{\cdot}80$ Å is higher than for SiO_4^{-4} by about 70 Δ. This is in fair agreement with the experimental E_{SiK_β} difference of about 50 Δ between α-quartz and stishovite and suggests that differences in K_β spectra arising from differences in coordination number may be reproduced fairly well by our method.

Charge distribution information from $SiK_{\alpha 3,4}$ shifts

The $SiK_{\alpha 3,4}$ satellite lines from doubly-ionized atoms can also yield information on electronic structure. Although Koffman and Moll[26] stated that there was no obvious correlation between their measured SiK_α energies and chemical nature in the group of silicates they studied, we find that their $K_{\alpha 3,4}$ data fall naturally into four groups: SiO_2, other framework silicates, chain silicates, and isolated tetrahedral silicates. The results are consistent with Si charge which increases with the degree of polymerization. In Table 5 we present our grouping of the $K_{\alpha 3,4}$ data of Koffman and Moll. From isolated tetrahedron (Fe_2SiO_4) to framework structure (SiO_2) we find a decrease in $\lambda_{K\alpha 3,4}$ of about $7\text{–}8 \times 10^{-4}$ Å. Using the value for the variation of $E_{K\alpha 3,4}$ with atomic charge given by Chun[8], we calculate a difference in effective Si charge between the two silicates of about 0·25 electrons, with Si more positive in SiO_2. The calculated $Q_{(SI)}$ values in Table 4 show a trend in agreement with these results both in direction and magnitude.

The results of Dodd and Glenn give very high values of Δ for some pyrosilicates ($Si_2O_7^{-6}$ groups), inconsistent with our results. However these minerals are unusual, e.g. in one of them, gehlenite, there are three T_d positions with $R(M-O) = 1{\cdot}63$, 1·63 and 1·87 Å.

Table 5. Regrouping of the $\lambda SiK_{\alpha 3,4}$ (Å) data of Koffman and Moll[26]

Group	$K\alpha_1$	$K\alpha_1$ group average	$K\alpha_1$	$K\alpha_1$ group average	Group structure type
SiO_2	7·0765	7·0765	7·0673	7·0673	Quartz
$KAlSi_3O_8$	7·0765		7·0678		Framework
$NaAlSi_3O_8$	7·0766	7·0765	7·0677	7·0677	aluminosilicates
$CaAl_2Si_2O_8$	7·0763		7·0677		
$Mg_2Si_2O_6$	7·0768		7·0680		
$CaSiO_3$	7·0770	7·0770	7·0680	7·0680	Chain silicates
$KAlSi_2O_6$	7·0772		7·0680		
$CaMgSi_2O_6$	7·0770		7·0682		
Fe_2SiO_4	7·0773	7·0773	7·0680	7·0680	Isolated tetrahedron
Si metal	7·0803	7·0803	7·0713	7·0713	Metal

$E_{K\alpha 3,4}$ increases as degree of linkage increases.

The distribution of silicon between the three sites is not known and so the effect of R(Si–O) variation cannot be determined. This may explain the discrepancy.

Predicted shift of other lines

Our results allow us to predict the shifts in other X-ray emission lines. The SiK'_β line should shift to higher energy with increasing R at about three times the rate of K. However with increasing polymerization $E_{\mathrm{Si}K'_\beta}$ increases so the effects tend to cancel and we expect little $E_{\mathrm{Si}K'_\beta}$ variation. In the Si $L_{2,3}$ spectra we associate the peaks with the $4a_1$, $5a_1$ and $5t_2$ orbitals. As R decreases and polymerization increases, the effects of the variations again cancels so these peaks should show little shift. For the OK_α peaks there is a general decrease in energy as R decreases, but $E_{\mathrm{O}K_\alpha}$ is higher for O_{br} than for O_{nbr} in $Si_2O_7^{-6}$. We feel that the effect of polymerization will predominate, leading to higher $E_{\mathrm{O}K_\alpha}$ as the degree of polymerization increases. Although such experimental comparisons are not available for silicates we can compare $E_{\mathrm{O}K_\alpha}$ for SiO_2 and Al_2O_3 [27]. The OK_α line is found at lower energies in Al_2O_3 by about 0·08 AU. This is consistent with out calculations which show O to be more negative in AlO_4^{-5} than in SiO_4^{-4} (the difference is about 0·07 electrons). For the inequivalent oxygens of $Si_2O_7^{-6}$ we find $E_{\mathrm{O}K_\alpha}$ to shift to lower energy as the oxygen becomes more negative at a rate of 1·5 AU/electron, so the calculated difference of O charges in SiO_2 and Al_2O_3 could yield the experimental result.

Simplified model for SiK shifts

Employing equations (1) and (2) as a basis, we can develop a simple model to explain SiK shifts. As noted by Manne the energy separations of core orbitals can be obtained from one center integrals alone, since the two center terms cancel (even in accurate calculations). We represent the dependence of the energy separation on the orbital populations by the following formula:

$$E_{i\to j} = E^\circ_{i\to j} + \sum_{k \text{ on } A} \Delta P_k \{[(ii/kk) - 0{\cdot}5(ik/ik)] - [(jj/kk) - 0{\cdot}5(jk/jk)]\} \quad (5)$$

where $E^\circ_{i\to j}$ is the transition energy in a reference state and ΔP_k is the difference in k orbital population. We can abbreviate this as

$$E_{K_{\alpha,\beta}} = E^\circ_{K\alpha,\beta} - \sum_k \Delta P_k \, \delta_k^{\alpha,\beta} \quad (6)$$

and in Table 6 we give values for $\delta_k^{\alpha,\beta}$. We see from Table 6 that while the effect of 3s and 3p populations on E_{K_α} will be appreciable the 3d population will have little influence. For this reason calculations with and without 3d orbitals, giving different Si charges but similar 3s and 3p populations, would probably give similar K_α shifts. The term involving δ^α_{2p} has normally been ignored, but this is an important term influencing the variation of E_{K_α} very strongly. It should be remembered that this 2p orbital is a Slater orbital rather than an atomic Hartree–Fock 2p orbital. Equation (6) has been found to give good results for E_{K_α} for all the systems considered in this paper, verifying the opinion that bonding effects (as opposed to charge distribution effects) may be neglected in determining $E_{\mathrm{Si}K_\alpha}$.

The values of δ^β are much larger than those of δ^α, consistent with the larger dependence of E_{K_β} on charge found in atomic SCF calculations. However since the Si3p is a valence orbital equation (6) is not accurate. A satisfactory simple formula for $E_{\mathrm{Si}K_\beta}$ has not been

Table 6. Values of δ_K^α and δ_K^β (AU)

K	δ_K^α	δ_K^β
$3s^{[a]}$	0·0020	0·1525
$3p^{[a]}$	0·0138	0·2917
$3d^{[b]}$	0·0006	0·0826
$2p^{[a]}$	1·5513	1·9922

[a] BA MBS exponents.
[b] $\xi = 1{\cdot}3$.

found. The main reason seems to be that the '$4t_2$-like' orbitals have both Si3p and O2p character and the dependence of their eigenvalues upon the F matrix elements is quite complex. In general increased Si3p, O2p overlap is associated with lower SiK_β values for the SiO_4^{-4} series. For θ variation in $Si_2O_7^{-6}$ E_{SiK_β} correlates with the eigenvalue sum which should roughly parallel the total molecular energy.

Discrepancies between calculation and experiment for Si X-ray emission spectra in SiO_2 and Si metal

Experimental data also exist for the SiK_α and K_β spectra of Si in silicon metal. In comparing SiO_2 with Si metal, experiment shows E_{SiK_α} to increase by 0·016 AU in going from metal to oxide and E_{SiK_β} to decrease by 0·160 AU. We find E_{SiK_α} for $Si_2O_7^{-6}$ to lie at 0·072 AU above the free Si atom ($2p^2$ ^1S) value. Although the Mulliken charge of Si must be zero in Si metal, we would expect the valence electron density to become more diffuse and $E_{K\alpha}$ to increase as though the Si possessed a partial positive charge. This explains part of the discrepancy, but another part must be due to an exaggeration of the Si–O charge separation in our calculations.

We find the E_{SiK_β} for $Si_2O_7^{-6}$ falls far below the line determined by the one center term of equation (6) alone, but is 0·27 AU above the free atom value since E_{K_β} increases rapidly with Si charge. The explanation for the discrepancy must be similar to that in the K_α case above. The K_α and K_β energies of $Si_2O_7^{-6}$ would both have the proper values with respect to Si metal if the difference in effective Si charge between $Si_2O_7^{-6}$ and the metal were about 1·1. The large lowering of E_{K_β} from the value given by equation (6) is essential to this result. This lowering is clearly associated with $Si3_p$, $O2_p$ overlap. Studies of transition metal $K_{\beta 5}$ spectra have lead some authors to calculate 'effective charges' of such atoms in the metal from the variation of $E_{K\beta 5}$ with oxidation state[5]. Charges around +1 are generally found. If Si is assigned an effective charge of about +1 in silicon metal, our results are in reasonable agreement with experiment.

ESCA shifts

The shift of the O1s ESCA line in silicates has been studied by Huntress and Wilson[28] and by Yin, Ghose and Adler[29]. Huntress and Wilson found the O1s binding energy (BE) to be lower in fayalite (Fe_2SiO_4, isolated tetrahedra, all oxygens non-bridging) than in SiO_2 (framework, all oxygens bridging) by 0·5 eV. Yin *et al.*, on the other hand, find non-bridging oxygens to have higher binding energies than bridging oxygens in orthopyroxenes. Such apparent inconsistency demonstrates that obtaining information on charge distributions from solid state ESCA results will often be difficult. In our $Si_2O_7^{-6}$ results we find O_{br} to be less negative than O_{nbr} by about 0·13 electrons. By Koopmans theorem[34] we equate ionization potentials and eigenvalues. The ϵ (O1s) difference between O_{br} and O_{nbr} is about 0·21 AU with O_{br} 1s more strongly bound. To calculate relative O1s BE's in orthopyroxene we must also consider the effect of the metal ions needed to produce charge balance: It is well known that the effect of these ions may be large[11], [35]. In pyroxene the distances of the bridging and non-bridging oxygens from the metal atoms are very different. The metal in the more distorted site (designated M2) is in 6-fold coordination with 4 O_{nbr} and 2 O_{br} with the distances to O_{br} being almost 0·5 Å greater. The metal in the more regular M1 site has only O_{nbr} in its first coordination sphere. Distances from M1 to the next nearest neighbor O_{br} are at least 1·3 Å greater. Using the X-ray diffraction data of Ghose[33] we have calculated the point charge potentials produced by two +2 charges, one in M1 and one in M2, at the positions of O_{br} and O_{nbr}. Point charge potentials from all more distant atoms were ignored since they should approximately cancel for O_{br} compared to O_{nbr}. We find the M1 and M2 point charges

JPCS 397 P12

to stabilize O_{nbr} by about 0·26 AU with respect to O_{br}. The point charge effect of the metal atoms is them approximately equal and opposite to the eigenvalue difference in free $Si_2O_7^{-6}$. Using free $Si_2O_7^{-6}$ with the point charge term added we find O_{br} 1s less strongly bound than O_{nbr} 1s by about 1 eV, in fortuitously good agreement with the results of Yin *et al.* considering the numerous approximations in our calculation.

CONCLUSIONS

Our results indicate that molecular orbital calculations at the present level can be useful for assigning X-ray emission spectra. They can also yield a great deal of semi-quantitative information on the relationship of Si K_α and K_β transition energies to the molecular and electronic structure of silicates. Calculated charge distributions are also found to be in agreement with ESCA results. Comparison with X-ray emission and ESCA data appears to be an excellent way of testing the accuracy of MO calculations. The reasonable agreement of our calculations with experiment suggests that chemical trends are given correctly, particularly trends in charge distributions. Our calculations indicate clearly that Si becomes more positive as R(Si–O) decreases and as polymerization increases and that bridging oxygens are less negative than non-bridging oxygens.

Table 7. Experimental and calculated X-ray transition energies (EV)

	Exp.	Calc. *A*	*B*	*C*
K_α	1740	1761	1757	1732
K_β	1832	1872	1858	1837
$L_{2,3}m$	89	111	100	98
OK_α	526	531	539	524

A uncorrected.
B correction (i) added
C corrections (i) and (ii) added.

APPENDIX

Calculated absolute values of X-ray transition energies are in fair agreement with experiment if corrections are made for (i) the difference of minimum basis set and near Hartree–Fock basis set atomic SCF eigenvalues and (ii) the electronic 'relaxation' of the core ion. In Table 7 we give experimental energies, and our calculated energies, uncorrected, and with corrections of type (i) and (ii) added. The eigenvalues of Si^{+2} and O^- from our minimum basis set and the near Hartree–Fock basis of Clementi [36] form the foundation for correction (i). The approximate formulas of Snyder [37] were used for correction (ii). Both upper and lower levels involved in the transition were corrected for relaxation.

Acknowledgements—The author is grateful for the interest and suggestions of Prof. Roger G. Burns and Dr. D. J. Vaughan. This research was supported in part by NASA grant NGL 22-009-187. Many of the computer programs employed were coded by Dr. E. A. Laws.

REFERENCES

1. VAUGHAN D. J., BURNS R. G. and BURNS V. M., *Geochim. Cosmochim. Acta* **35**, 365 (1971).
2. DODD C. G. and GLENN G. L., *J. appl. Phys.* **39**, 5377 (1968).
3. O'NIONS R. K. and SMITH D. G. W., *Nature (Phys. Sci.)* **231**, 130 (1971).
4. GIBBS G. V., HAMIL M. M., BARTELL L. S. and YOW H., *Am. Mineral.* (1972) in press.
5. KOSTER A. S. and MENDEL H., *J. Phys. Chem. Solids* **31**, 2511 (1970).
6. URCH D. S., *J. Phys. C.* **3**, 1275 (1970).
7. FISCHER, D. W., *J. Phys. Chem. Solids* **32**, 2455 (1971).
8. CHUN H. U., *Phys. Lett.* **31A**, 118 (1970).
9. (a) WHITE E. W. and GIBBS G. V., *Am. Mineral.* **52**, 985 (1967); (b) WHITE E. W. and GIBBS G. V., *Amer. Mineral.* **54**, 931 (1969).
10. WARDLE R. and BRINDLEY G. W., *Am. Mineral.* **56**, 2123 (1971).
11. Manne R., *J. Chem. Phys.* **46**, 4645 (1967).
12. (a) HILLIER I. H. and SAUNDERS V. R., *Int. J. Quant. Chem.* **4**, 203 (1970); (b) GELIUS U., ROOS B. and SIEGBAHN P., *Theor. Chim. Acta* **23**, 59 (1971).
13. POPLE J. A. and SEGAL G. A., *J. chem. Phys.* **44**, 3289.
14. NEWTON M. D., BOER F. P. and LIPSCOMB W. N., *J. Am. Chem. Soc.* **88**, 2353 (1966).
15. HILLIER I. H., *J. chem. Soc.* A, 878 (1969).
16. CLEMENTI E. and RAIMONDI D. L., *J. chem. Phys.* **38**, 2686 (1963).
17. BOYD D. B. and LIPSCOMB W. N., *J. chem. Phys.* **46**, 910 (1967).
18. BOER F. P. and LIPSCOMB W. N., *J. chem. Phys.* **50**, 989 (1969).
19. TOSSELL J. A. and LIPSCOMB W. N., *J. Am. Chem. Soc.* **94**, (1972) in press.
20. (a) SMITH F. C. and JOHNSON K. H., *Prog. Rept. #73 Solid State and Molecular Theory Group*, M.I.T.; (b) BISHOP D. M., RANDIC M. and

GALLEY No. 204--22

Geo Acta 2148 Pergamon Press, Oxford
1st Proof MS pages 1-28 Galleys 1-6
The Universities Press, Belfast 8.11.72

1

Geochimica et Cosmochimica Acta, 1973, Vol. 37, pp. ### to ###. Pergamon Press. Printed in Northern Ireland

Interpretation of K X-ray emission spectra and chemical bonding in oxides of Mg, Al and Si using quantitative molecular orbital theory

J. A. TOSSELL
Department of Earth and Planetary Sciences
Massachusetts Institute of Technology, Cambridge, Mass. 02140, U.S.A.

(*Received* 9 *June* 1972; *accepted in revised form* 23 *August* 1972)

Abstract—Quantitative molecular orbital calculations are reported for Mg, Al and Si in tetrahedral and octahedral coordination with oxygen. These calculations are employed to assign and interpret the MK_α, MK_β and OK_α X-ray emission spectra of the corresponding oxides. The interpretation of the MK_β spectrum reproduces the observed trends in main peak and satellite energies with variation of metal, ligand and geometry. The splitting of the main K_β peak, observed in many oxides, is found to be a result of interaction between adjacent metal atoms. The calculations also reproduce the observed trends in OK_α spectra. The electric structures of the various oxides are discussed briefly.

INTRODUCTION

MOLECULAR orbital (MO) theory is presently finding increased application in geochemistry. For example, several MO studies of bonding in silicates have recently appeared (GIBBS *et al.*, 1972; LOUISNATHAN and GIBBS, 1972). Qualitative MO diagrams have been used for some time to assign X-ray emission spectra (DODD and GLENN, 1968). Also, experimental X-ray transition energies have been used in conjunction with spectral assignments from qualitative MO theory to construct quantitative MO diagrams empirically (FISCHER, 1971). For the oxyanions of sulfur and chlorine approximate self-consistent-field linear combination of atomic orbitals molecular orbital (SCF LCAOMO) calculations are available (MANNE, 1967) and have been used in the interpretation of the X-ray emission spectra of these compounds (ANDERMANN and WHITEHEAD, 1971).

Since X-ray emission spectra yield well understood experimental quantities which can be easily compared with the results of MO calculations they provide an excellent method for testing the validity of such calculations. The different series of X-ray emission spectra (e.g. SiK_α, SiK_β, $SiL_{2,3}$, OK_α in SiO_2) can be combined to give information on the energies and charge distributions of almost all of the molecular orbitals of the sytem. These experimental results then allow us to assess the accuracy of the calculated quantum mechanical results for the whole set of MO's rather than for just a small subset (as is the case for most spectroscopies). Once agreement with the experimental X-ray emission data has been demonstrated we can have some confidence in our ability to describe accurately, using MO theory, those properties which are more difficult to determine experimentally. Examples of properties of this type are the binding energies of various geometrical configurations of mineral structures and the charge distribution in these structures. In this paper, MO results for oxides of Si, Al and Mg are presented and these results are used to assign and interpret data from X-ray emission spectroscopy. After agreement with experiment has been demonstrated a brief discussion is given of the calculated molecular charge distributions.

Theory

The molecular orbitals are obtained as solutions to the quantum mechanical Schrodinger equation in its Hartree–Fock–Roothaan form, suitable for SCF LCAO MO calculations (Roothaan, 1951). The equation to be solved is, in matrix form,

$$FC = \varepsilon SC \tag{1}$$

where F is the Fock Hamiltonian matrix; C is the vector of coefficients of atomic orbitals (AO's) in the MO's; S is the overlap matrix; and ε is a diagonal matrix giving the MO eigenvalues, which correspond to vertical ionization potentials. The F matrix, the essential quantity in equation (1), is rather difficult to calculate. Several schemes have been developed for approximating its elements. The method employed here is a refinement of the non-empirical molecular orbital (NEMO) method of Newton *et al.* (1966). It is a self-consistent-field version of this method which incorporates elements of the complete neglect of differential overlap method, version 2 (CNDO/2) of Pople and Segal (1966) and is called SCF NEMO.

In both the NEMO and the SCF NEMO methods the off diagonal elements of F are given as

$$F_{ij} = T_{ij} + KijSij\left(\frac{\bar{U}ii + \bar{U}jj}{2}\right) \tag{2}$$

where Tij is a kinetic energy integral, $\bar{U}ii$ is an averaged potential energy integral and Kij is a parameter chosen to reproduce Fij values obtained from accurate *ab initio* solutions to the Hartree–Fock–Roothaan equations for related molecules, in which all integrals are evaluated accurately and no approximations (beyond those leading to the Hartree–Fock–Roothaan equation) are made. Studies of the theoretical foundation of Extended Huckel MO (EHMO) theory by Newton *et al.* (1966) have indicated equation (2) to be superior to its Extended Huckel analog

$$Fij = KSij\left(\frac{Fii + Fjj}{2}\right) \tag{3}$$

For the diagonal elements of F the NEMO theory gives

$$Fii = \alpha i \tag{4}$$

where the αi are the diagonal elements from *ab initio* calculations on related molecules. In the SCF NEMO theory the diagonal elements depend upon the charge distributions in the molecule studied according to the formula (for a closed shell electronic state)

$$Fii + \mathring{Fii} + \sum_{i \text{ on } A} \Delta Pj\{(\overline{iijj}) - 0{\cdot}5\,(\overline{ijij})\} + \sum_{B \neq A} Q_B R_{AB}^{-1} \tag{5}$$

where $\mathring{Fii}$ is a reference value obtained from an atomic SCF calculation for a specified electronic configuration of the atom or ion, ΔPj is the change in the Mulliken population* of atomic orbital j, Q_B is the Mulliken charge on atom B and $(\overline{iijj})$ and $(\overline{ijij})$

* Definitions of the various charge distributions quantities are given in Mulliken (1955). The defining equations are (for closed shells): population of orbital j: $Pj = 2\sum_n \sum_k C_{nk}S_{kj}$

charge on atom B: $Q_B = Z_B - \sum_{k \text{ on } B} P_k$

overlap population of A and B

$$n(A - B) = 2\sum_n \sum_{i \text{ on } A} \sum_{k \text{ on } B} C_{ni}C_{nk}S_{ik}$$

are averaged values of the integrals of the electron repulsion operator $e^2 r_{12}^{-1}$, where r_{12} is the distance between electrons 1 and 2.

Earlier comparison of SCF NEMO with *ab initio* SCF results for the SO_4^{-2} anion has shown SCF NEMO to give relative MO energies to an accuracy of 1–2 eV. (TOSSELL, 1972). The SCF NEMO method includes all electrons so that energies are obtained for both valence and core MO's.

MO STRUCTURE OF Si OXIDES IN TETRAHEDRAL (T_D) AND OCTAHEDRAL (O_h) GEOMETRIES

The gross MO structure is found to be the same for both the tetrahedral and octahedral oxides of Si, Al and Mg. MO diagrams for these oxides are given in Fig. 1.

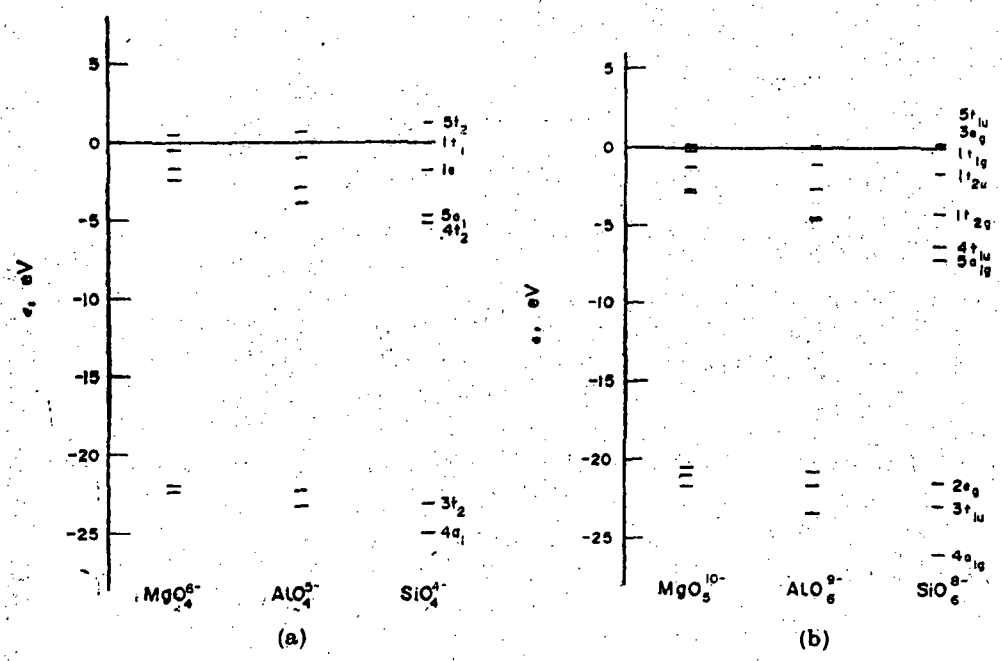

Fig. 1(a). Valence molecular orbital energy level diagrams for MgO_4^{-6} and SiO_4^{-5}* (with $1t_1$ eigenvalues set equal).

Fig. 1(b). Valence molecular orbital energy level diagrams for MgO_6^{-10}, AlO_6^{-9} and SiO_6^{-8}† (with $1t_{1g}$ eigenvalues set equal).

In Tables 1 and 2 the eigenvalues and percentage atomic orbital composition of the molecular orbitals are given for the anions SiO_4^{-4} and SiO_6^{-8}. The basis sets of atomic orbitals employed were the best atom minimum basis sets (BA MBS) of CLEMENTI and RAIMONDI (1963) and the M—O distances are given in Fig. 1. A tabular representation (Tables 1 and 2) is required in addition to the conventional MO diagrams given in Fig. 1 since the information on %AO composition is as important for our purposes as is the information on orbital eigenvalues. In the figures and tables the MO's are labeled by symmetry type and by number within a symmetry

* Distances used were R(Mg—O) = 1·89 Å, R(Al—O) = 1·75 Å, R(Si—O) = 1·60 Å.
† Distances used were R(Mg—O) = 2·12 Å, R(Al—O) = 1·93 Å, R(Si—O) = 1·80 Å.

Table 1. Eigenvalues and atomic orbital percentage compositions of filled molecular orbitals for SiO_4^{-4}

Orbital*	ε (eV)	AO % composition†
$5t_2$	-29·2	1 % Si3p, 99 % O2p
$1t_1$	27·9	100 % O2p
$1e$	26·2	100 % O2p
$5a_1$	23·3	17 % Si3s, 1 % O2s, 82 % O2p
$4t_2$	22·9	19 % Si3p, 71 % O2p
$3t_2$	4·9	3 % Si3p, 97 % O2s
$4a_1$	3·1	3 % Si3s, 97 % O2s
$2t_2$	−87·8	99 % Si2p, 1 % Si3p
$3a_1$	−137·1	100 % Si2s
$1t_2$	−508·2	100 % O1s
$2a_1$	−508·2	100 % O1s
$1a_1$	−1849·9	100 % Si1s

* Orbitals are labeled by symmetry type and in order of increasing energy within each symmetry type.

† The percentage of AO i in MO p is defined as

$$\sum_k C_{pk} S_{ik} / 2 (= P'_{ii})$$

where the sum on k is over all AO's.

Table 2. Eigenvalues and atomic orbital percentage compositions of filled molecular orbitals for SiO_6^{-8}

Orbital	ε (eV)	AO % composition
$5t_{1u}$	53·5	2 % O2s, 97 % O2p
$3e_g$	53·4	100 % O2p
$1t_{1g}$	53·3	100 % O2p
$1t_{2u}$	51·7	100 % O2p
$1t_{2g}$	49·1	100 % O2p
$4t_{1u}$	47·1	14 % Si3p, 1 % O2s, 85 % O2p
$5a_{1g}$	46·2	13 % Si3s, 4 % O2s, 82 % O2p
$2e_g$	31·9	100 % O2s
$3t_{1u}$	30·4	1 % Si3p, 99 % O2s
$4a_{1g}$	27·4	5 % Si3s, 95 % O2s
$2t_{1u}$	−64·6	98 % Si2p, 2 % Si3p
$3a_{1g}$	−112·6	99 % Si2s
$2a_{1g}$	−482·0	100 % O1s
$1e_g$	−482·0	100 % O1s
$1t_{1u}$	−482·0	100 % O1s
$1a_{1g}$	−1827·6	100 % Si1s

type in order of increasing energy. The symmetry types are determined by the irreducible representations of the tetrahedral or octahedral point group. Because of the excess negative charge on the systems, many of the filled MO's have positive eigenvalues. However, we shall be interested only in differences of eigenvalues, so this point will cause no difficulty.

The valence MO's for SiO_4^{-4} can be divided into three groups: (1) $4a_1$ and $3t_2$ which are predominantly O2*s* orbitals, (2) $4t_2$ and $5a_1$ which are σ-bonding orbitals with both Si and O character; (3) $1e$, $1t_1$ and $5t_2$ which are non-bonding and weakly π-bonding predominantly O2*p* orbitals. For SiO_6^{-8}, a similar division may be made with $4a_{1g}$, $3t_{1u}$ and $2eg$ being mainly O2*s* orbitals; $5a_{1g}$ and $4t_{1u}$ σ-bonding orbitals; and the five highest orbitals non-bonding or weakly π-bonding orbitals. More accurate SCF calculations on tetrahedral oxyanions (Gelius, *et al.*, 1971) indicate that the MO orderings in Table 1 are probably correct, except for the order of $5t_2$ and $1t_1$. The relative energy of these orbitals may be in error by several eV. The orbital order in SiO_6^{-8} should also be correct for the most part.

Assignment of X-ray Emission Spectra

A detailed discussion of the assignments of the SiK_α, K_β, $L_{2,3}$ and OK_α spectra for α-quartz is given elsewhere (Tossell, 1972) . Here the assignments of the MK_α and K_β and OK_α spectra for M = Mg, Al and Si in tetrahedral and octahedral coordination with oxygen are presented and calculated energies and intensities are compared with experimental results, where available. Group theory yields the selection rules needed to identify the allow transitions.

MK_α Spectra

The MK_α transition, nominally $M2p \rightarrow Mls$ in character, is identified with the $2t_2$ MO in tetrahedral and the $2t_{1u}$ MO in octahedral coordination. The K_α line is found at higher energies in oxides than in the corresponding metal. The calculations give E_{MK_α} values 2 to 3 eV larger in the oxides than in the free atoms. This trend is in the right direction but is substantially larger than the experimental metal to oxide difference, which is about 0·5 eV. Experiment also indicates that E_{K_α} increases with increasing M--O distance and with increasing coordination number of the metal. These trends are also reproduced by the calculations. Octahedral oxides are calculated to have higher E_{MK_α} than tetrahedral oxides by about 1 eV, which is, however several times larger than the experimental difference. The higher value of E_{K_α} in octahedral relative to tetrahedral oxides can be related to the higher Mulliken charge on the metal atom in octahedral coordination. In another place (Tossell, 1972) the K_α shifts for Si and Al are discussed in more detail and it is shown that the AlK_α peak shift, as a function of R(Al--O) for Al in tetrahedral coordination (as measured by Wardle and Brindley, 1972), is given by SCF NEMO calculations to within about a factor of 2.

MK_β Spectra

In Fig. 2 MK_β spectra are presented for SiO_2 and MgO. In the SiO_2 spectrum we observe three features: a satellite peak $K_{\beta'}$, a main peak K_β and a shoulder on the high energy side of K_β. In MgO the main K_β peak is split into two components.

Assignments and calculated energies and intensities for MK_β spectra are given in Table 3. Intensities are calculated from the % Si3*p* character in the individual MO's. Manne (1970) employed a similar method for hydrocarbon CK_α spectra. Agreement between calculation and experiment is fairly good. For example, the relative energies and intensities of the three peaks in the K_β spectrum of α-quartz are predicted with

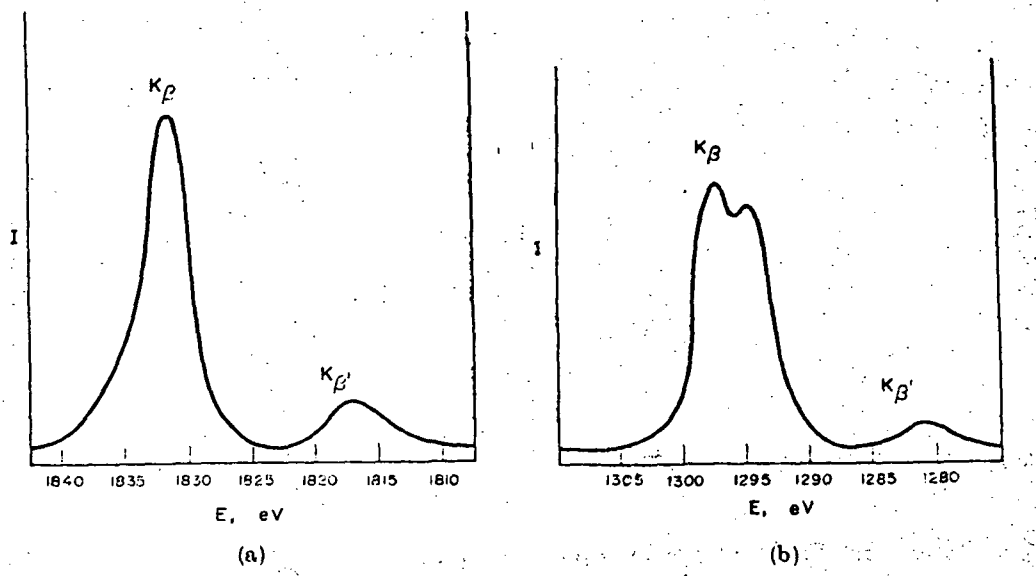

Fig. 2. Experimental* MK_β X-ray emission spectra for (a) α-quartz and (b) periclase.

Table 3. Experimental and calculated relative energies (eV) and intensities in MK_β spectra

	Exp.*		Calc.			Exp.		Calc.		
	Si T_d							Si O_h		
	ΔE	I	Assignment	ΔE	I	ΔE	I	Assignment	ΔE	I
$K_{\beta'}$	−13·7, −14·4	15	$3t_2 \rightarrow 1a_1$	−17·9	16	—	—	$3t_{1u} \rightarrow 1a_{1g}$	−16·6	9
K_β	0	100	$4t_2 \rightarrow 1a_1$	0	100	—	—	$4t_{1u} \rightarrow 1a_{1g}$	0	100
shoulder	+5·0	1·5	$5t_2 \rightarrow 1a_1$	+6·3	5	—	—	$5t_{1u} \rightarrow 1a_{1g}$	6·4	1
	Al T_d							Al O_h		
	ΔE	I		ΔE	I	ΔE	I		ΔE	I
$K_{\beta'}$				−18·6	17	−16·9	20		−17·1	8
K_β				0	100	0	100		0	100
shoulder				4·7	3	—	—		4·7	2
	Mg T_d							Mg O_h		
	ΔE	I		ΔE	I	ΔE	I		ΔE	I
$K_{\beta'}$				−19·6	24	−16·2	25		−18·2	28
K_β				0	100	0	100		0	100
shoulder				2·9	2	—	—		2·8	0

* Experimental values are taken from the tables of Urch (1970) and the figures of Dodd and Glenn (1968).

reasonable accuracy. The $K_{\beta'}$ peak is assigned to the $3t_2$ MO of mainly O2*s* character, yielding a peak of the proper energy and intensity. The high energy shoulder on the main K_β peak is assigned to the $5t_2$ MO, yielding an acceptable energy and intensity. It is not necessary to assign this peak to a symmetry forbidden transition from an orbital of *e* symmetry, as in Dodd and Glenn (1968). The separation of main K_β peak and the high energy shoulder is calculated to be 1·6 eV smaller for tetrahedral

* From Dodd and Glenn, 1968.

Si than for tetrahedral Al in close agreement with the experimental value of 1·5 eV (BROWN *et al.*, 1969).

URCH (1970a, b) has used qualitative MO theory to explain the observed variation in the K_β-$K_{\beta'}$ energy difference (here designated Δ) within a series of oxides as the cation changes from Mg to Cl. He observed that Δ decreased by 3–5 eV along this series and that the M3*p* orbital also decreased in energy; i.e. became more strongly bound, with Cl3*p* more stable than Mg3*p* by about 8 eV. The observed decrease in Δ was interpreted as a lowering in energy of the $4t_2$ MO of mostly M3*p* and M3*s* character relative to the $3t_2$ MO of mainly O2*s* character, which decreased in energy at a slower rate. Since the variation in M3*p* energy is about two or three times as large as the observed Δ variation, the $4t_2$ MO will probably be less than half M3*p* in character.

One also observes a change in Δ as the ligand, L, coordinating the central metal varies, with Δ increasing along the first row from C to F. The interpretation of URCH (1970a, b) indicates that this occurs because of the variation of the energy of the L2*s* and L2*p* orbitals. The difference of L2*p* and L2*s* energies for first row atoms increases at a rate of about 5 eV per unit increase in nuclear charge, similar in magnitude to the observed shift in Δ. Also, Δ values for oxides and fluorides range from 13·7–16·9 and 19–21, respectively, in good agreement with the L2*p*–L2*s* energy differences of 14·8 and 20·4 for O and F, respectively. This indicates that for oxides and fluorides the $4t_2$ MO (and its octahedral analog $4t_{1u}$) is predominantly L2*p* in character, in agreement with the results presented in Tables 1 and 2. The $4t_2$–$3t_2$ energy difference is then predominantly a L2*p*–L2*s* difference, modified by M3*p* participation in the $4t_2$ MO.

Since differences of L2*p* and L2*s* energies obtained from a minimum basis set atomic SCF calculation are substantially larger than the experimental values tabulated by URCH (1970), good absolute values of Δ can not be expected from the calculations. However, it is found that relative Δ values are given well. The quantitative MO results reported here give a decrease in Δ of ~0·85 eV per unit increase in nuclear charge, in good agreement with the experimental value of about 0·6–1·0 eV/unit charge. However, the experimental data are not good enough to establish whether the trend is as uniform as it is here calculated to be.

The value of $E_{MK_{\beta'}}$ is also found to decrease slightly from octahedral to tetrahedral oxides in our calculations, in agreement with the results of DODD and GLENN (1968). The calculated decrease is around 2 eV for Mg, increasing to 3 eV for Si. This is several times larger than the experimental value. Also, calculated E_{MK_β} values are lower for tetrahedral oxides than for octahedral by about half the magnitude of the $K_{\beta'}$ shifts. The calculated SiK_β peak shift between SiO_4^{-4} and SiO_6^{-8} is calculated to be about 40 per cent larger than the experimental difference between α-quartz and stishovite (WHITE and GIBBS, 1967). Our calculations indicate that Δ is lower in octahedral than in tetrahedral oxides by about 1 eV. Experimental data are presently not available to test this result except for those oxides in which the splitting of the main K_β peak renders such analysis difficult.

A rather curious feature of the MK_β spectrum is the splitting of the main K_β peak by several electron volts which occurs in several oxides. A related observation is that K_β peak widths are larger in octahedral oxides in which such splitting is more

commonly observed. The peak splitting in corundum (α-Al_2O_3), with Al in octahedral coordination, has been interpreted by DODD and GLENN (1968) as a result of transitions from the $4t_{1u}$ MO of Al $3p\sigma$ character and the $5t_{1u}$ MO of Al $3p\pi$ character. Although our calculated $5t_{1u}$-$4t_{1u}$ energy differences could be reconciled with this interpretation we must reject it since the %M $3p$ character in the $5t_{1u}$ MO is very small and the intensity of the peak generated by this MO is therefore quite low. The $5t_{1u}$ MO in octahedral symmetry is chemically almost identical to the $5t_2$ MO in tetrahedral symmetry which has been assigned to the weak high energy shoulder in the α-quartz spectrum. Another possible explanation for the K_β splitting is a distortion of the AlO_6 octahedron. However, SCF NEMO calculations show that even a distortion of 0·2 Å would yield a K_β splitting of less than 1 eV. The explanation must then lie in the interaction of neighbouring units in the structures. There is an important difference between the type of linkage of the fundamental metal–oxygen units in α-quartz and, for example, periclase (MgO) which shows a large K_β splitting. In α-quartz the SiO_4 units are linked by corner sharing. In periclase the linkage is by edge sharing. Interaction between Si atoms in α-quartz is therefore small since an oxygen core occupies the region between the two silicons. In MgO the oxygen ligands are at some distance from the Mg–Mg internuclear direction. The interaction of the Mg atoms is therefore essentially unimpeded. This geometrical difference is shown in Fig. 3 for the dimer geometries used in the calculations to described below.

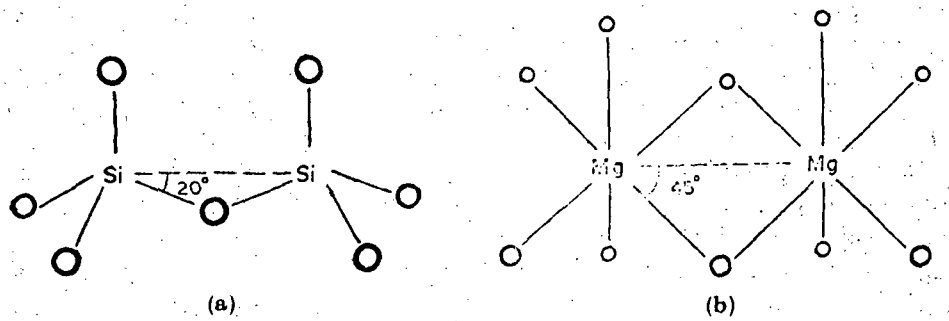

Fig. 3. Geometries employed for dimeric units $Si_2O_7^{-6}$ and $Mg_2O_{10}^{-16}$.

To test the qualitative hypothesis presented above SCF NEMO calculations were performed on the dimeric units $Si_2O_7^{-6}$ and $Mg_2O_{10}^{-16}$. The distances and angles chosen yielded essentially identical M—M distances [R(Si—Si) = 3·02 Å, R(Mg—Mg) = 3·00 Å]. The Mg valence orbitals were only slightly more diffuse than those of Si and yielded overlap integrals larger by only about 10 per cent. On the other hand, an extremely large difference was observed in M—M overlap populations [designated n(A—B)], with n(Si—Si) = −0·06 and n(Mg—Mg) = −0·44, indicating qualitatively different M—M interactions in the α-quartz and periclase models. In the periclase model the M—M interaction is very strongly antibonding.

The '$4t_2$ like' MO's in $Si_2O_7^{-6}$ are also spread over a smaller energy range than are the '$4t_{1u}$ like' MO's in $Mg_2O_{10}^{-16}$. However this may be due partly to the smaller number of oxygens engaged in bridge bonding in the Si dimer. The most important result of the calculations is clearly the difference in M—M overlap populations.

Although our dimeric results can only give a crude picture of the electronic structure of a complex solid, they quantitatively support the hypothesis proposed. The M---M interaction in edge shared $Mg_2O_{10}^{-16}$ is found to be much greater than that in corner shared $Si_2O_7^{-6}$. The large metal-metal interaction in MgO is hypothesized to be the cause of the MgK_β splitting.

OK_α

Our assignment of the OK_α emission spectrum of α-quartz (O'NIONS and SMITH, 1971; SMITH and O'NIONS, 1972a) is given in Table 4. The 531 eV peak in their spectrum has recently been interpreted by them as mainly a reflectivity spike, although

Table 4. Experimental and calculated relative energies (eV) and intensities of OK_α spectra for α-quartz

Exper.		Calc.		
ΔE	I	Valence orbital assignment	ΔE	I
0		$5t_2$	0	99
−1·0	4	$1t_1$	−1·2	100
−2·8		$1e$	−3·0	67
−5·8	1	$5a_1$	−5·9	27
		$4t_2$	−6·3	71

some characteristic intensity remains after correction for this effect. The remaining characteristic intensity probably arises from a double ionization process, which is outside the scope of our calculations (FISCHER, 1965). If this peak is disregarded, agreement between calculation and experiment is quite good. The division of the spectrum into a high energy and a low energy band is reproduced with reasonable energies and intensities.

The high energy OK_α band, at about 525 eV, arises from the non-bonding MO's and lies slightly higher in energy in Si oxides than in Al or Mg oxides. Also the lower energy peak, (520–522 eV), arising from the σ bonding orbitals, is separated from the high energy peak by different amounts in the Si, Al and Mg oxides (SMITH and O'NIONS, 1972). The separation increases along the series from Mg to Si, consistent with the calculated MO eigenvalues presented in Fig. 1. Experimental values of this separation (SMITH and O'NIONS, 1972) are 2·9 eV for periclase, 4·1 eV for corundum and 4·9 eV for α-quartz. The calculated separations between the ($1t_1$, $1t_{1g}$) MO and the ($4t_2$, $4t_{1u}$) MO for $Mg_6O_6^{-10}$, AlO_6^{-9} and SiO_4^{-4} are about 2·8, 4·6 and 5·1 eV, respectively. The agreement of calculation and experiment is therefore rather good. The increase in the peak separation along the series Mg to Si is indicative of an increase in the stability of the σ bonding orbitals along the same series. The analysis above is clearly dependent upon the decision to ignore the anomalous 531 eV peak and its success supports this decision.

ELECTRONIC STRUCTURE OF Mg, Al AND Si OXYANIONS

Having established the ability of SCF NEMO calculations to reproduce trends in X-ray emissions spectra we can have some confidence in the other properties obtained from them. Here some features of the calculated electronic structures are

discussed briefly. The variations of several charge distributions parameters for the systems considered are presented in Table 5. The metal charges are found to increase uniformly along the series Mg, Al, Si and in passing from tetrahedral to octahedral coordination. The variation in the M3*s* atomic orbital population is fairly small and the total number of electrons on the metal is fairly constant. However, a uniform increase in P_{M3s} is observed, indicating that the ratio of K_β intensity to K_α intensity should increase along the series Mg to Si. The charge on oxygen also decreases uniformly along the same series. However, this may well be a result of the decreasing charge on the oxyanion. The increase in unbalanced electron repulsions as the anionic charge increases will also tend to place too many electrons on the 'outside' of the molecule, i.e. upon the oxygens. If this effect is real it would manifest itself in higher energies for the OK_α peaks in oxides of Si than in the corresponding oxides of Al or Mg. As mentioned before, the experimental data is in general agreement with this result (SMITH and O'NIONS, 1972). However, the relative oxygen charges must be uncertain until larger clusters are studied.

Table 5. Charge distribution in MO_4 and MO_6 anions

	MgO_4^{-6}	MgO_6^{-10}	AlO_4^{-5}	AlO_6^{-9}	SiO_4^{-4}	SiO_6^{-8}
Q(M)	1·06	1·26	1·88	1·96	2·58	2·83
Q(O)	−1·77	−1·88	−1·72	−1·83	−1·64	−1·80
P_{M3s}	0·21	0·22	0·20	0·25	0·39	0·37
P_{M3p}	0·83	0·67	1·00	0·93	1·06	0·87
$\%M3p^{4t_2,4t_{1u}}$*	14·5	11·2	16·7	13·3	18·8	13·8

* The numbers given are $\%M3p$ in either the $4t_2$ or the $4t_{1u}$ MO, depending upon the coordination symmetry.

The higher values of E_{MK_β} in octahedral oxides, as compared with tetrahedral, seems to be connected with their lower covalency. The amount of M3*p* per cent character in the $4t_{1u}$ MO in octahedral oxides is consistently smaller than the M3*p* per cent character in the analogous tetrahedral point group orbital, the $4t_2$. The calculations also show a gradual increase in metal orbital participation in the σ bonding orbitals along the series Mg to Si for both tetrahedral and octahedral oxides (see Table 5). Figure 1 shows a substantial spreading of the MO energy level diagram along the same series. Noniterative NEMO calculations using neutral atom α's show the same trend. Therefore both MO compositions and MO energies indicate a substantial increase in covalency along the series Mg to Si for both tetrahedral and octahedral oxides. Figure 1a shows that as the covalency increases both the $4t_2$ and $3t_2$ MO's (as well as their octahedral analogs shown in Fig. 1b) are lowered in energy relative to the $1t_1$. However, the $4t_2$, the more strongly σ-bonding of the two, is lowered by a larger amount and the value of Δ, the K_β–$K_{\beta'}$ separation, is therefore decreased. The value of Δ is then a fairly direct measure of covalency.

CONCLUSION

The quantitative MO calculations presented here have been shown to be capable of assigning the $MK_{\alpha 1,2}$ peak and all the peaks normally observed in the MK_β and OK_α

spectra without invoking symmetry forbidden transitions or making *ad hoc* assumptions about bonding type. Trends in K_β–K_β energy differences resulting from variation of metal, ligand and geometry have been reproduced by the calculations and URCH's (1970a, 1970b) interpretation of MK_β spectra, which is qualitatively correct, has been made more quantitative. The splitting of the main MK_β peak in several oxides has been related to the type of linkage of their fundamental metal–oxygen units. This demonstration of good agreement between calculation and experiment for X-ray emission spectra suggests that the calculations reported here will generally yield an accurate picture of the electronic structure of oxidic compounds of Mg, Al and Si. The calculations show the gross MO structure of the various oxides to be quite similar. In all cases the valence MO's can be divided into three groups, defined in terms of energy and composition. Quantitative differences in the calculated electronic structures correspond closely with X-ray emission spectral results. In particular, Δ is shown to be closely related to the covalency, which increases substantially along the series Mg to Si.

Acknowledgements—The author is grateful for the interest and suggestions of Professor R. G. BURNS and Dr. D. J. VAUGHAN. This research was supported in part by NASA grant NGL 22-009-187. Many of the computer programs employed were coded by Dr. E. A. LAWS. Several helpful comments were made by the referees.

REFERENCES

ANDERMANN G. and WHITEHEAD H. C. (1971) Molecular X-ray spectra of sulfur and chlorine bearing substances. *Adv. X-ray Analysis*, Vol. **14**, Plenum Press.

BARTELL L. S., SU L. S. and YOW H. (1970). Lengths of phosphorus–oxygen and sulfur–oxygen bonds. An extended Hückel molecular orbital examination of Cruickshank's $d\pi$–$p\pi$ picture. *Inorg. Chem.* **9**, 1903–1912.

BROWN G. E., GIBBS G. V. and RIBBE P. H. (1969) The nature and the variation in length of the Si—O and Al—O bonds in framework silicates. *Am. Mineral.* **54**, 1044–1061.

CLEMENTI E. and RAIMONDI D. L. (1963) Atomic screening constants from SCF functions. *J. Chem. Phys.* **38**, 2686–2689.

DODD C. G. and GLENN G. L. (1968) Chemical bonding studies of silicates and oxides by X-ray K-emission spectroscopy. *J. Appl. Phys.* **39**, 5377–5384.

FISCHER D. W. (1965) Effect of chemical combination on the X-ray K emission spectra of oxygen and fluorine. *J. Chem. Phys.* **42**, 3814–3821.

FISCHER D. W. (1971) Soft X-ray band spectra and molecular orbital structure of Cr_2O_3, CrO_3, CrO_4^{-2} and $Cr_2O_7^{-2}$. *J. Phys. Chem. Solids* **32**, 2455–2480.

GELIUS U., ROOS B. and SIEGBAHN P. (1971) MO-SCF-LCAO studies of sulphur compounds. *Theoret. Chim. Acta* **23**, 59–66.

GIBBS G. V., HAMIL M. M., BARTELL L. S. and YOW H. (1972) Correlations between Si—O bond length, Si—O—Si angle and bond overlap populations calculated using extended Hückel molecular orbital theory. *Amer. Mineral.* in press.

LOUISNATHAN S. J. and GIBBS G. V. (1972) A Comparison of Si—O distances in the olivines with the bond overlap populations predicted by the extended Hückel theory. *Amer. Mineral.* in press.

MANNE R. (1967) Molecular orbitals and inner-electron-shell chemical shifts for sulfur and chlorine oxy-anions. *J. Chem. Phys.* **46**, 4645–4651.

MANNE R. (1970) Molecular orbital interpretation of X-ray emission spectra: simple hydrocarbons and carbon oxides. *J. Chem. Phys.* **52**, 5733–5739.

MULLIKEN R. S. (1955) Electron population analysis on LCAO-MO molecular wave functions. I. *J. Chem. Phys.* **23**, 1833–1840.

NEWTON M. D., BOER F. P. and LIPSCOMB W. N. (1966) Molecular orbital theory for large molecules. Approximation of the SCF LCAO Hamiltonian matrix. *J. Am. Chem. Soc.* **88**, 2353–2360.

O'NIONS R. K. and SMITH D. G. W. (1971) Bonding in SiO_2 and Fe_2O_3 by oxygen K_α X-ray emission spectra. *Nature (Phys. Sci.)* **231**, 130–133.

POPLE J. A. and SEGAL G. A. (1966) Approximate self-consistent molecular orbital theory. III CNDO results for AB_2 and AB_3 systems. *J. Chem. Phys.* **44**, 3289–3296.

ROOTHAAN C. C. J. (1951) New developments in molecular orbital theory. *Rev. Mod. Phys.* **23**, 69.

SMITH D. G. W. and O'NIONS R. K. (1972a) Investigation of bonding in some oxide minerals by OK_α emission spectroscopy. *Chem. Geol.* **9**, 29–41.

SMITH D. G. W. and O'NIONS R. K. (1972b) Investigations of bonding by OK_α emission spectroscopy: further evidence concerning the true character of the OK_α emission band. *Chem. Geol.* **9**, 145–146.

TOSSELL J. A. (in press) Molecular orbital interpretation of X-ray emission and ESCA spectral shifts in silicates. *J. Phys. Chem. Solids*, in press.

URCH D. S. (1970a) The origin and intensities of low energy satellite lines in X-ray emission spectra: a molecular orbital interpretation. *J. Phys., C., Solid State Physics* **3**, 1275–1291.

URCH D. S. (1970b) Low energy satellites in the X-ray fluorescence spectra of fluoro-anions. *Spectrochim. Acta* **25B**, 305–309.

WARDLE R. and BRINDLEY G. W. (1972) The dependence of the wavelength of AlK_α radiation from alumino-silicates on the Al—O distance. *Amer. Mineral.* **56**, 2123–2128.

WHITE E. W. and GIBBS G. V. (1967) Structural and chemical effects on the SiK_β X-ray line for silicates. *Amer. Mineral.* **52**, 985–993.

Geol. Soc. Amer., Ann. Meet., Minneapolis, Abstr., 4, (7) 692 (1972)

MOLECULAR ORBITAL (MO) INTERPRETATION OF THE METAL K_β, METAL L AND OK_α X-RAY EMISSION SPECTRA OF SOME OXIDE AND SILICATE MINERALS

Tossell, John A. and Vaughan, David J., Department of Earth and Planetary Sciences, Massachusetts Institute of Technology, Cambridge, Mass. 02139

Molecular orbital calculations, using an approximate SCF LCAOMO method, are presented for several oxides of Mg, Al, Si and Fe. The valence MO's for the tetrahedral third row oxides can be divided into three groups: (1) $4a_1$ and $3t_2$; O2s orbitals, (2) $4t_2$ and $5a_1$; σ-bonding orbitals, (3) $1e$, $1t_1$ and $5t_2$; non-bonding O2p orbitals. A similar division can be made for the octahedral oxides. The quantitative MO diagrams are used to assign the observed MK_β and OK_α X-ray emission spectral peaks for several oxide minerals. The trend in the MK_β-$MK_{\beta'}$ peak separation is calculated for the series MgO, Al_2O_3, SiO_2 and results are in agreement with experiment. The peak separations in the OK_α spectra show an increase along the same series, also given accurately by the calculations (exp. 2.9,4.1 and 4.9ev, calc. 2.8,4.6 and 5.1ev). The MK_β and OK_α peak separations are shown to be quantitatively related to the degree of metal-oxygen covalency. Fe L X-ray emission spectra are presented for several silicate minerals containing iron in different oxidation states and coordinations. The main L_α band is composed of four peaks which are assigned to the four valence MO's of e and t_2 type which possess substantial amounts of Fe3d character. An additional peak at lower energy is assigned to a MO which is predominantly O2s but has 1-2% 3d character. This peak is found to be significantly higher in energy in ferric compared to ferrous compounds.

D J Vaughan

X-ray Photoelectron, X-ray Emission and UV Spectra of SiO_2 Calculated by the SCF Xα Scattered Wave Method

J. A. Tossell and D. J. Vaughan
Dept. of Earth and Planetary Sciences,
Mass. Inst. of Tech. write out in full

and

K. H. Johnson
Dept. of Metallurgy and Materials Science,
Mass. Inst. of Tech. write out in full

(for submission to Chem. Phys. Letters)

Abstract

Photoionization , X-ray emission and UV excitation energies are calculated for SiO_2 by the SCF $X\alpha$ method and the transition-state procedure. In all cases agreement between calculation and experiment is good. The SiO_4^{-4} cluster is found to be adequate for describing localized excitations in quartz. The valence orbitals of this cluster are found to be naturally separable into three sets (1) O2s, nonbonding; (2) Si3s,3p and O2p, sigma bonding; (3) O2p nonbonding. The participation of Si3d type functions in the high energy O2p nonbonding orbitals is found to be very small.

Research by Aviva Brecher

An experimental study of magnetic properties of lunar rock (breccias) chips has been undertaken, complementary to current studies on them by Prof. Burns and coworkers. To date, I have examined the Apollo 16 samples 60315.51 and 62295.27. My non-destructive magnetic measurements are aimed at: 1) determining the intensity and stability of natural remanence in lunar rocks under study; 2) assessing the weight fraction of magnetic phases and the level of magnetic saturation; 3) identifying the minerals (oxides or native iron) carrying the remanence; 4) determining the size spectrum and associated magnetic behavior of carrier grains as a function of temperature. These have been achieved partly by studying coercivity, saturation moments and reduced saturation ratios.

Currently this experimental work entails great unnecessary effort, being carried out on improvised equipment, heavily used by workers in other departments at M.I.T. It is hoped to develop soon an adequate laboratory facility for studies of lunar and meteoritic paleomagnetism.

Theoretically, I intend to reexamine evidence on magnetism of lunar crystalline rocks, which is not consistent with the currently favored interpretation as thermoremanence, acquired in a global lunar field of $\sim$ 2000 γ. This interpretation has far-reaching implications regarding the thermal history of the moon and based only on remanence of breccias. Experimentally, it is hoped to carry out ferromagnetic resonance studies of lunar rock in order

to determine "in situ" relative volume fractions of grains of a given elongation. This will test Fuller's suggestions that remanence in lunar rocks and soils, although blocked at low temperatures in fine iron grains is stable under AF-cleaning because of their shape anisotropy.

It is also hoped to study the acquisition of inverse thermoremanence in lunar rocks, and the effect of thermal cycling (-80 to +140°C), stress and shock on it.

D. Leavy

Progress report on: Lunar Electrical Conductivity Project

The aim of this study is to invert the magnetic field spectrum ($f < 5 \times 10^{-2}$ hertz) observed in the solar wind and on the lunar surface in order to deduce the internal electrical conductivity of the moon. The electrical environment of the moon is modelled by a perfect conductor on its sunlit side and an empty cylinder on the downstream side. (See Fig. I.) A numerical scheme, detailed in App. I, is adopted in order to calculate the field induced by a layered moon.

Fig. 2. compared the data obtained by Sonett, et al. with the Apollo XII magnetometer with the field calculated by Sill and us for the same model. We see that as the frequency increases, Sill's calculation becomes inaccurate so that a large part of the spectrum cannot be used to model the moon response adequately.

In an attempt to model the asymmetry in the lunar plasma environment, Sonett et al. have recently modelled the moon as an infinite conducting core embedded in a non-conducting crust. We have tried to reproduce their results [Fig. 3, 4] within our theory and the result seems to agree quite well. Of course, our analysis is not constrained to such a model so we might expect that it will be a better tool to find the lunar conductivity.

Presently, we are trying to develop an inversion scheme and a resolution analysis of the data. This work should be completed, we hope, in early 1973.

Appendix I

Mathematical Theory

We consider a magnetic fluctuation of wavenumbers

$$k_1 = \frac{\omega}{V_{sw}} \tag{1}$$

impinging on the moon normally to the axis of the cylinder. I.e.,

$$\vec{H}^{inc} = \vec{a}_x H_o(\omega) e^{ik_1 z} \tag{2}$$

$$\vec{E}^{inc} = -\mu_o \vec{V}_{sw} \times \vec{H}^{inc} \tag{3}$$

The field inside the cylinder is given as the sum of two parts:

1) An inhomogeneous field satisfying the continuity of the tangential electric field at the plasma-cylinder boundary;

2) A field having no tangential electric field at the solar wind-cylinder boundary, but satisfying the continuity of the tangential electric and magnetic field at the moon-cylinder boundary.

Formally we have

$$\vec{H} = \frac{1}{i\omega\mu_o} \nabla \times \vec{E} \tag{4}$$

and

$$\vec{E} = \vec{a}_\rho \left[\sum_i - \alpha_i \cos\phi \frac{\partial J_i}{\partial \lambda_{1i}\rho}(\lambda_{1i}\rho)e^{-\lambda_{1i}z} + \sum_i \beta_i \cos\phi \frac{i\omega\mu_o}{\lambda_{2i}^2 \rho} J_1(\lambda_{2i}\rho)e^{-\lambda_{2i}} \right.$$

$$\left. + \mu_o H_o v_{sw} \cos\phi \frac{J_1(\lambda\rho)}{\lambda\rho} \frac{e^{ik_1 z}}{\frac{\partial J_1(\lambda a)}{\partial \lambda a}} \right]$$

$$+ \vec{a}_\phi \left[\sum_i \alpha_i \frac{\sin\phi}{\lambda_{1i}\rho} J_1(\lambda_{1i}\rho)e^{-\lambda_{1i}} - \sum_i \beta_i \frac{i\omega\mu_o}{\lambda_{2i}\rho} \frac{\partial J_1}{\partial \lambda_{2i}\rho}(\lambda_{2i}\rho)e^{-\lambda_{2i}z} \right.$$

$$\left. - \mu_o H_o v_{sw} \sin\phi \frac{\partial J_1}{\partial \lambda\rho}(\lambda\rho) \frac{e^{ik_1 z}}{\frac{\partial J_1(\lambda a)}{\partial \lambda a}} \right]$$

$$+ \vec{a}_z \left[\sum_i \alpha_i \cos\phi \; J_1(\lambda_{1i}\rho)e^{-\lambda_{1i}\rho} \right] \qquad (5)$$

where λ_{1i} and λ_{2i} are respectively the root of the cylindrical Bessel function J_1 and its derivative

$$\lambda = ik_1$$

and α_n and β_n are the coefficients of the TM and TE modes respectively.

Inside the moon, the field is expanded in a sum of toroidal and poloidal mode.

At the surface of the moon, we must meet the continuity of the tangential electric field on the front side. The continuity of the tangential electric and magnetic field must also be met inside the moon and on the back side.

Imposing these conditions at a certain number of points around the surface of the moon and including in the resulting system of equations only a finite number of modes, we can solve for the field by a least-square technique. The number of modes included in the analysis is determined by the criterion that only a few percent mismatch in the boundary condition is allowed.

MOON ELECTRICAL ENVIRONMENT

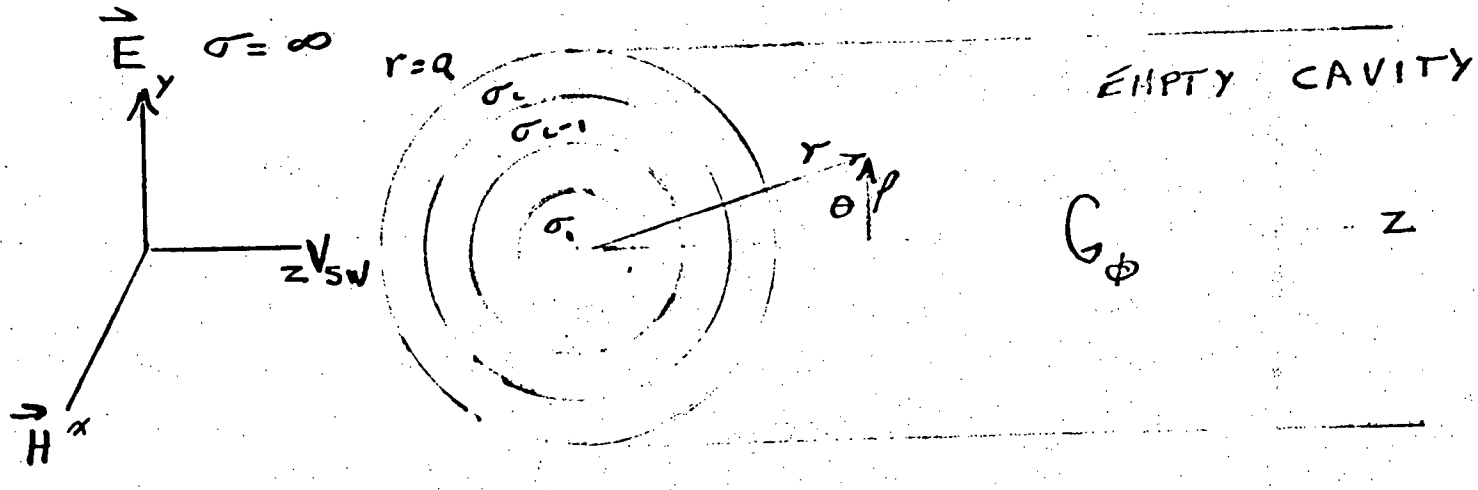

Fig. 1.

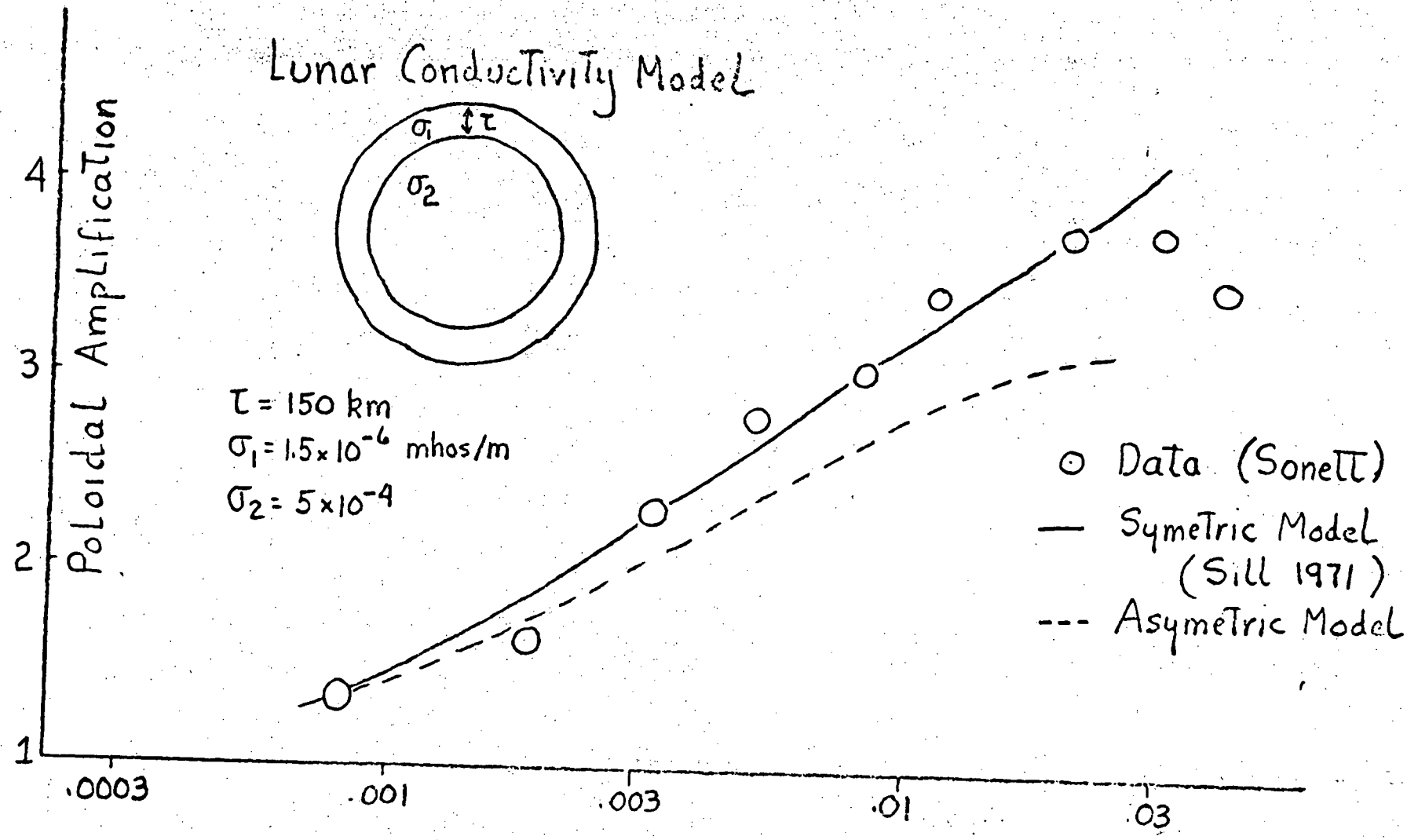

Fig 2. Lunar Front Side Responce to Interplanetary Magnetic Fields
Comparison of Symetric and Asymetric Models

FIG: 3

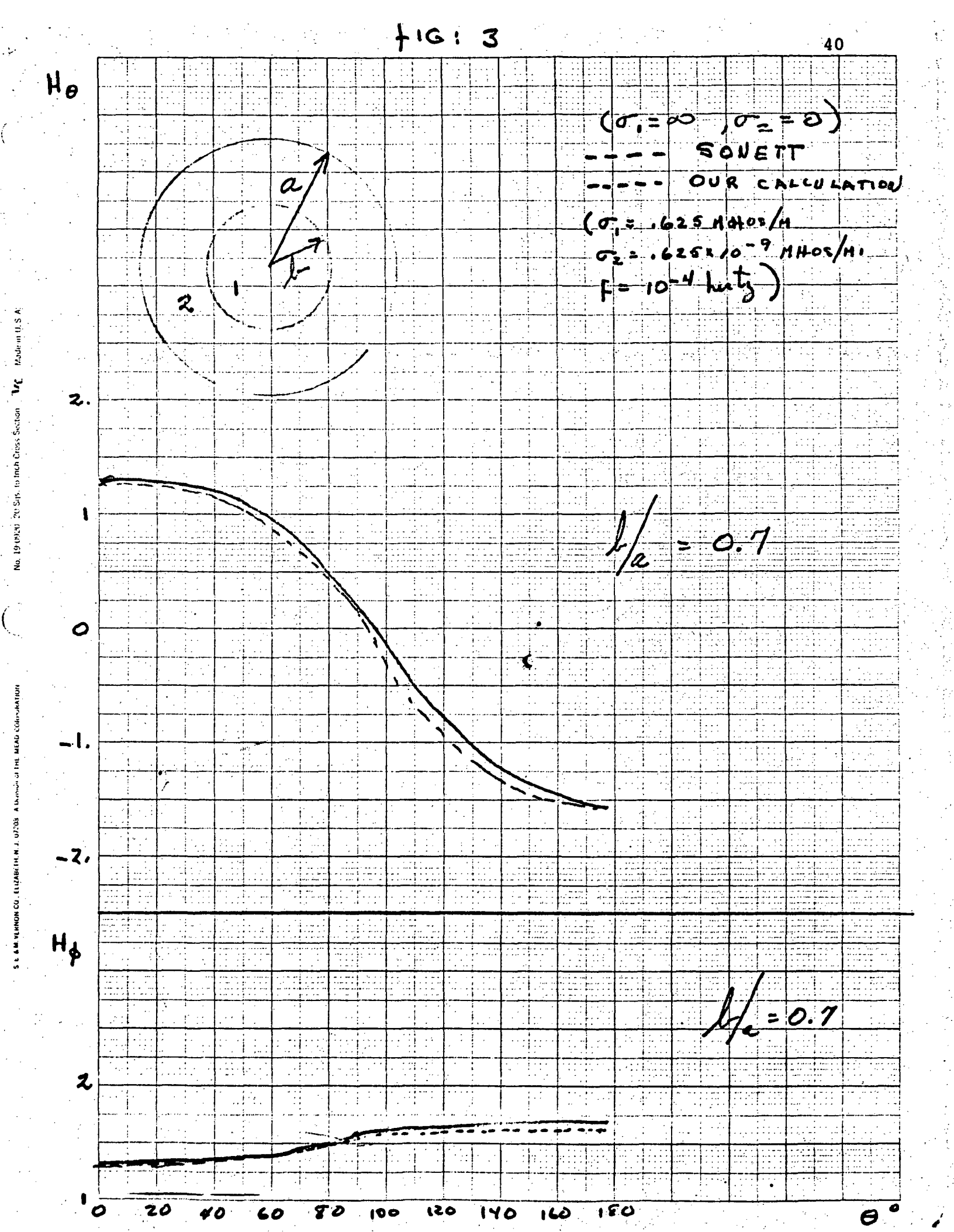

Fig: 4

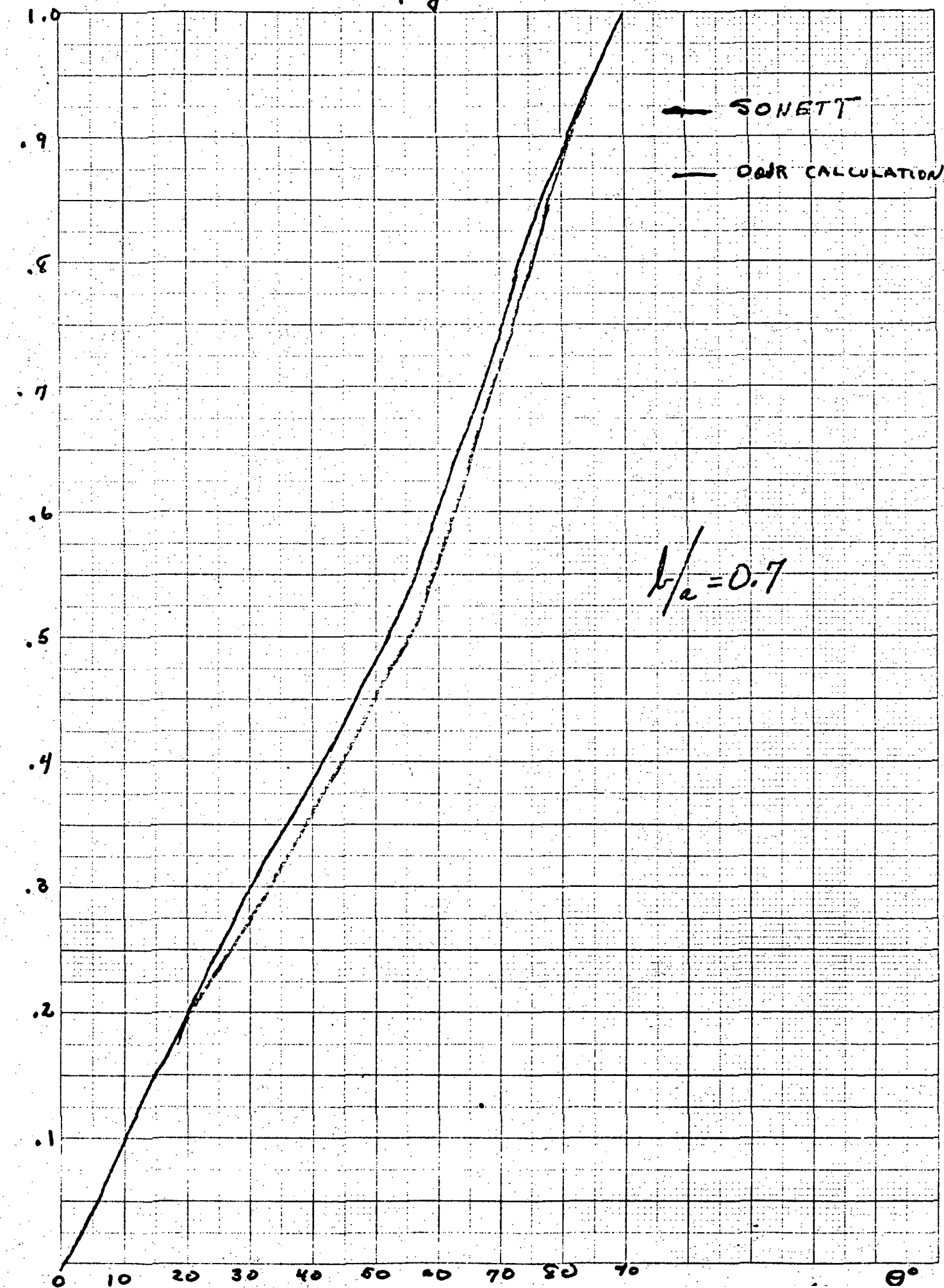

NATURE VOL. 238 JULY 21 1972

HIDDEN

LETTERS TO NATURE

PHYSICAL SCIENCES

On the Nature of the Tycho X-ray Source

Of the five X-ray sources which are identified with remnants of supernovae, the Tycho 1572 source is of particular interest. In this case the X-ray emission cannot be considered as the continuation of the synchrotron radio spectrum because it can easily be shown that, independent of the mechanism of injection, the spectrum must be "bent" in the frequency region $\nu < 10^{13}$ Hz. Also, it cannot be assumed that the observed X-radiation is thermal and caused by hot plasma behind the front of shock-wave produced by the expanding envelope of a remnant. This mechanism qualitatively explains X-radiation from Cassiopeia A if the undisturbed density n_0 of interstellar matter in the vicinity of the explosion is about 30 cm^{-3}. This value of n_0 is in excellent agreement with the density of the HII region which is observed around Cas A (ref. 1). But in the case of the Tycho remnant one must assume that $n_0 \sim 5$ cm^{-3} if the radiation is thermal. Such a value of n_0 contradicts the observed large dimensions of this remnant, which, according to all indications, has exploded in a relatively rare medium between the clouds of interstellar matter, where $n_0 \leq 0.1$ cm^{-3}. This excludes the possibility of explaining X-radiation from Tycho as thermal radiation from hot plasma.

It seems probable that this source should be identified with a young pulsar which originated after the explosion of the Tycho supernova. Because of "unfavourable" orientation of the rotation axis of this pulsar, coherent radio emission is not observed.

But there are good reasons to believe that young pulsars should generate synchrotron radiation in the optic and X-ray ranges (similar to NP 0532, ref. 2). The power of this radiation must be a very steeply diminishing function of the pulsar's age. *It is essential to note that the intensity of synchrotron* radiation of NP 0532 between pulses is not zero. For example, according to Vishvanathan[3], the intensity of radiation between the main and secondary "peaks" is about 1.5% of the maximum intensity in the main "peak". According to Bradt *et al.*[4], in the X-ray range the "interpulse" intensity is near 10%. In the 100–400 keV range this intensity is sufficiently larger (I. Kurfess, unpublished work). Consequently, one should remember that there is a "quasi-isotropic" component in the X-radiation of young pulsars. The time-averaged power of this component is at least equal to the "pulse" component. The X-ray flux from the Tycho supernova remnant is ~25 times smaller than that from the Crab Nebula[5] and, consequently, it is half the X-ray flux from NP 0532. Since the distance to SN Tycho is approximately 2.5 times that to the Crab, the observed X-radiation from the Tycho remnant can be explained if the power from the expected pulsar, which is situated inside Tycho, is three times that from NP 0532. This can be explained naturally by the youth of Tycho's pulsar. Recently Henriksen *et al.* (unpublished work) suggested that X-radiation from Tycho and some other sources can be interpreted as thermal radiation of his crust heated due to dissipation of rotation energy of a neutron star. In our case it should be supposed that the crust temperature is 25×10^6 K. But in this case the linear dimensions of the source must be unacceptably small—above 1 km.

The observable tests of our hypothesis are as follows: (*a*) measurement of angular dimensions of Tycho's X-ray source—according to our hypothesis, the upper limit of angular dimensions of this source must be essentially smaller than those of the radio source; (*b*) discovery of a small periodic modulation of X-ray flux from Tycho caused by expected anisotropy of radiation of Tycho's pulsar; (*c*) a study of 18th to 19th magnitude stars in the central part of the Tycho radio source with the object of discovering an optical pulsar with periodically modulated flux; (*d*) discovery of a "point" X-ray source in the remnant of Kepler's Supernovae 1604.

The "quasi-isotropic" component of pulsars' synchrotron radiation must play an essential role in the physics of the Crab Nebula. Evidently, this radiation generated by relativistic electrons closed in the radiation belts of NP 0532. The spectrum of this radiation is essentially harder than in the main pulse. This can explain the expected relation between pulsars and nebular synchrotronous spectra[2].

It should be noted that in connexion with Pacini's explanation of "glitch" in NP 0532, the systematic observation of "quasi-isotropic" component synchrotronous radiation of NP 0532 is desirable.

I. S. Shklovsky

Institute for Cosmic Research, Moscow

Received February 23, 1972.

1 Van den Bergh, S., *Astrophys. J.*, **165**, 259 (1971).
2 Shklovsky, I. S., *Astrophys. J. Lett.*, **159**, L77 (1970).
3 Vishvanathan, N., *The Crab Nebula*, 152 (Reidel, Dordrecht, 1971).
4 Bradt, H., *et al.*, *Nature*, **218**, 856 (1968).
5 Gorenstein, P., Kellog, E., and Gursky, H., *Astrophys. J.*, **160**, 199 (1970).

Lunar Electrical Conductivity

Sonett *et al.*[1,2] have inverted sunward lunar surface magnetometer data to obtain a lunar electrical conductivity profile, using the poloidal magnetic response to a spatially uniform source field of a radially structured conducting sphere immersed in an infinitely conducting plasma[3,4]. The experimentally determined lunar response expressed as the tangential magnetic spectral amplification factor is shown in Fig. 1 together with the best fit poloidal responses for a two-layer and a multi-layer Moon and their corresponding electrical conductivity profiles[5].

The spatial symmetry imposed on the boundary conditions by this model of the interplanetary magnetic field–Moon interaction neglects the solar wind plasma–Moon–void geometry and the finite application time of the interplanetary magnetic field which result from the solar wind flow past the Moon. We have studied qualitatively the effects of including these boundary condition asymmetries through numerical examinations of an asymmetric cylindrical model of the interaction (Fig. 2). In our model a cold, infinitely conducting

solar wind plasma is incident with velocity $v_0\hat{x}$ and the solar wind borne magnetic field $\mathbf{H}$ is aligned along the axis $\hat{z}$ of a cylindrical Moon[6].

Fig. 3 shows the numerically determined sunward surface response of the asymmetric model of the interaction for a three-crust conductivity model with a highly resistive thin outer layer added to eliminate the toroidal mode. The analytically determined cylindrical analogue of the poloidal response of the symmetric model[6] is also shown. Comparison reveals

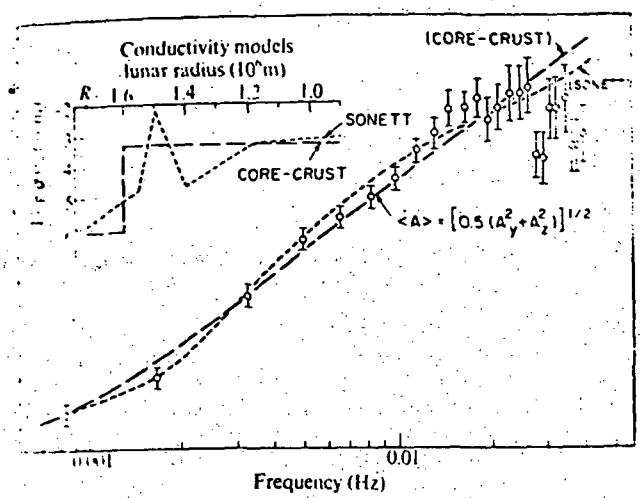

Fig. 1 Experimental tangential amplification factor from Sonett *et al.*[2], shown with the calculated poloidal responses for the inset conductivity profiles reproduced in part from ref. 5.

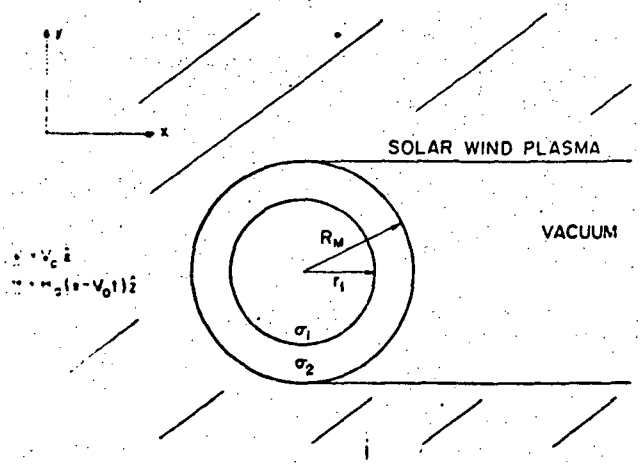

Fig. 2 Asymmetric model of solar wind borne magnetic field interaction with cylindrical Moon.

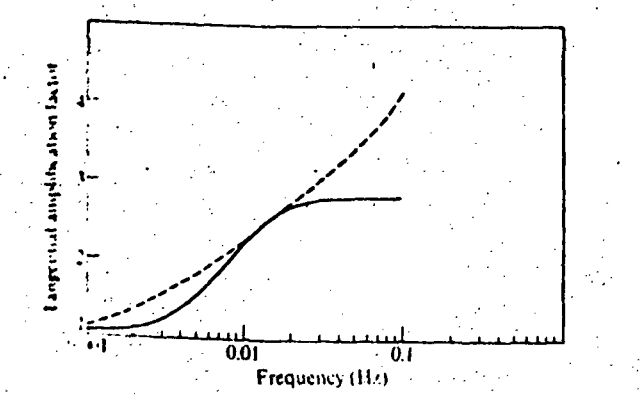

Fig. 3 Cylindrical analogue of poloidal response. - - -, Symmetric analytical; ——, asymmetric numerical, $v_0 = 3.0 \times 10^5$ m/s; $r_0 = 1.4 \times 10^6$ m; $\sigma_1 = 5.0 \times 10^{-4}$ mho/m; $\sigma_2 = 1.5 \times 10^{-6}$ mho/m.

first, the depressed asymmetric response at low frequencies resulting from diffusion of field lines around the core into the anti-solar cavity on a time scale $\mu_0\sigma_2 L^2$, where $L \sim R_M$ is the scale length of the diffusion process; and second, the flattened asymmetric response for high frequencies which results from application of the incident field to the sunward lunar surface on a time scale of R_M/v_0.

These features of the response of the asymmetric model are also present in the experimentally determined response (Fig. 1). An attempt to fit these features using the poloidal response of the symmetric model of the interaction resulted in the complicated conductivity profile obtained by Sonett *et al.* We also note that the response of the asymmetric model is insensitive to increases in the core conductivity σ_1, from which we conclude that the experimental sunward tangential magnetic response does not exclude a more conductive lunar interior.

A. COLBERT REISZ
DONALD L. PAUL
THEODORE R. MADDEN

Department of Earth and Planetary Sciences,
Massachusetts Institute of Technology,
Cambridge, Massachusetts 02139

Received February 9, 1972.

1 Sonett, C. P., Colburn, D. S., Dyal, P., Smith, B. F., Schubert, G., and Schwartz, K., *Nature*, 230, 359 (1971).
2 Sonett, C. P., Schubert, G., Smith, B. F., Schwartz, K., and Colburn, D. S., *Proc. Apollo 12 Lun. Sci. Conf.* (MIT, 1971).
3 Blank, J. L., and Sill, W. R., *J. Geophys. Res.*, 74, 736 (1969).
4 Sill, W. R., and Blank, J. L., *J. Geophys. Res.*, 75, 201 (1970).
5 Sill, W. R., *Bellcomm TM-71-2015-9* (1971).
6 Reisz, A. C., Paul, D. L., and Madden, T. R., *The Moon* (in the press).

Lunar Electrical Conductivity—Reply

REISZ *et al.*[1] consider, in the preceding letter, two conceptually important points regarding the lunar transfer function inversions which we reported[2,3]. That work used a symmetric confining current theory so that the dark hemisphere diamagnetic cavity effect was ignored, as we pointed out at that time; Blank and Sill[4] estimated that the effect upon the sunward hemisphere transfer function is small. Recently Schubert and Lee (private communication) have computed the fields associated with a magnetostatic configuration where confining currents exist sunward of the Moon, upon the surface of a perfectly conducting core and upon the walls of the diamagnetic cavity. Their results are applicable here by relating their core radius to an effective skin depth at a specified frequency. Approximate damping depths are given in ref. 3. For frequency $f \lesssim 0.001$ Hz and $R_c \sim 0.6\ R_m$ where R_c is the core radius and R_m the lunar radius, the cavity correction to front side data not adjacent to the terminator is about 4%. For $f \gtrsim 0.01$ Hz the correction increases to about 20%. The effect upon conductivity is trivial for $R_c \sim 0.6\ R_m$ and is a factor of about 3 for $f \gtrsim 0.01$ Hz; the resultant change in estimated deep temperature is insignificant. For the shell, dominated by the higher frequencies, a combined change in shell depth and conductivity takes place but is beyond the scope of this letter. So we do not agree that field line diffusion through the crust and past the core can account for the very large difference in transfer function in Fig. 3 of ref. 1 for $0.002 \lesssim f \lesssim 0.006$. We note also that the skin depth at $f \simeq 0.002$ Hz for the core conductivity[1] indicates a core radius of only 900 km, hardly sufficient to produce the effects described. Lastly, the difference between the two cases shown in Fig. 3 of ref. 1 is non-monotonic, which does not seem likely for various reasons. For example, higher harmonic effects ($l > 1$) are unimportant below $f \sim 0.008$ Hz (Fig. 1). On the basis of

MORPHOLOGY OF SELECTED LUNAR FEATURES USING EARTH-BASED RADAR

G.H. Pettengill and Pierre Biraben

One of the major difficulties lying in the way of using the full resolution possible in the preparation of lunar maps by radar at the Harstack Observatory has been inaccuracy in the working ephemeris. While the intrinsic lateral surface resolution is on the order of 2 km with an associated height measurement accuracy of about 200 m, inaccuracies in the standard values for the lunar orbital motion, physical libration and rotation led to lateral discontinuities of up to 15 km when maps prepared at different times were compared. The corresponding discrepancies in surface height were of the order of 2 km. As a result, the assembly of composite maps of topography and radar scattering characteristics were impaired.

In the course of other research at MIT, I.I. Shapiro and his students have developed a versatile planetary ephemeris program (PEP) which has some capability to accept observations of the Moon and to yield improved estimates of the necessary values listed above. During the course of the present reporting period, Pierre Biraben has developed a way of using PEP to produce corrections to the original working ephemeris which yield predictions of lateral

positions to an accuracy of about 2 km. He has developed the necessary intermediate digital programming to use the outputs obtained from PEP to calculate selenocentric latitude and longitude of the lunar subradar point, the position and doppler angles, and the apparent rotational velocity of the Moon at 5-minute intervals throughout each observation. A total of 50 days of observation were included, extending from October 1970 to August 1972. Comparison of these improved predictions with the measurements shows a lateral consistency of about 1 km, with only one case approaching a discrepancy of 5 km. Topography of adjacent areas seems to be consistent to within 100 m.

Further work under this grant has ceased as of 31 August 1972 because of the transfer of the personnel to other research.

Lunar Research Statement

H. F. Hinteregger

I have spent most of my time since the beginning of November 1972 constructing and testing 5 pairs of Differential Doppler Receivers (DDRs). These are semi-production versions of the 2 original prototypes which were developed by C. Counselman and myself in the preceding several months and which were successfully used in trial observations between STDN (NASA) Tracking Stations in Florida and California on Oct. 27 and 28, 1972. Three pairs of the new DDRs will be used within the next three weeks at the tracking stations in Madrid, Florida, and Ascension Island. In March, intensive observations using at least 6 tracking stations will be started and I will be responsible for readying at least a sufficient number of DDRs for this purpose.

Lunar Research Statement

R. W. King

My research work since Nov. 1 has been related to the determination of the lunar physical libration from differential VLBI tracking of the ALSEP transmitters. Most of my time during this period was spent reducing the data taken in a two-day test performed Oct. 27 and 28 using the STDN stations at Goldstone, Calif., and Merritt Island, Fla. From these data we have obtained post-fit residuals at the level of about 50 cm in equivalent distance on the moon. These results, together with some analysis of anticipated accuracies in the determination of lunar baselines and the physical libration, have been prepared for presentation at the Conference on Lunar Dynamics to be held at the Lunar Science Institute in Houston, Texas, Jan. 14-17, 1973.

In addition to analyzing the test data, I have spent some time in programming tasks related to the eventual processing of a significant amount of these data. In particular, the equations for the numerical integration of the rotation of the moon about its center of mass and the partial derivatives with respect to libration parameters have been coded, though not completely checked out. Finally, I have obtained from the Space Science Data Center at GSFC all of the lunar laser ranging data which have been released by the NASA LURE team, and I have compiled these data in a format which can be used with our program.

BK/jbu

Jack Pines

An ultrasonic seismic modeling set-up has been constructed and is in the process of being refined. Both surface and body waves have been observed before and after the introduction of various configurations of scatterers in the medium to determine the effect produced by them. The indication at this point is that a small number of surface scatterers will destroy surface wave propagation while a large number of randomly placed scatterers will generate energy envelopes and dispersion characteristics similar to those observed in lunar seismograms.

Gilbert Wayne Ullrich

During the past four months, work was accomplished comparing meteor impacts on the lunar surface to the impacts of man-made objects. Specifically addressed, was the question of the relationship between the seismic coupling coefficients of the two types of events. This information is important for it would allow the man-made impacts to serve as calibration events to determine, through seismic measurements, the energy of meteors impacting the surface. It was learned that, because of the lower peak shock pressures of the man-made impacts, they would be expected to have a higher seismic coupling coefficient. A more detailed study of the mechanics of impact events is required to estimate the relationship between the coupling of the two types of events.

for Z. Kopal, ed., Harold Urey
Anniversary Volume, D. Reidel

THERMAL HISTORY AND EVOLUTION OF THE MOON

M. Nafi Toksöz and Sean C. Solomon

Department of Earth and Planetary Sciences

Massachusetts Institute of Technology

Cambridge, Massachusetts 02139

U.S.A.

Copies: 2
Ms Pages: 73
Figures: 14
Tables: 2

Send Proofs to: M. Nafi Toksöz, Room 54-518, M.I.T.,
Cambridge, Massachusetts 02139, U.S.A.

ABSTRACT

Possible models for the thermal evolution of the Moon are constrained by a wide assortment of lunar data. In this work, theoretical lunar temperature models are computed taking into account different initial conditions to represent possible accretion models and various abundances of heat sources to correspond to different compositions. Differentiation and convection are simulated in the numerical computational scheme.

Models of the thermal evolution of the Moon that fit the chronology of igneous activity on the lunar surface, the stress history of the lunar lithosphere implied by the presence of mascons, and the surface concentrations of radioactive elements, involve extensive differentiation early in lunar history. This differentiation may be the result of rapid accretion and large-scale melting or of primary chemical layering during accretion. Differences in present-day temperatures for these two possibilities are significant only in the inner 1000 km of the Moon and are not resolvable with presently available data.

If the Apollo 15 heat flow is a representative value, the average uranium concentration in the moon is 65 ± 15 ppb. This is consistent with achondritic bulk composition (between howardites and eucrites) for the Moon.

1. INTRODUCTION

The development of the thermal regime is the most important factor in the evolution of a planetary body. For the Moon, as well as other planetary objects, magmatization, differentiation, and other processes of evolution are controlled by the thermal history. The interpretation of geological, geochemical and geophysical data from the Moon requires temperature information since bulk properties of materials are dependent on temperature. The purpose of this paper is to investigate the thermal evolution and present-day temperature models for the Moon as currently constrained by the vast amount of data from the lunar missions.

The most serious studies of the thermal evolution and heat balance of the Moon started with the pioneering efforts of Urey (1951, 1952, 1955, 1957, 1962). Other studies that followed (MacDonald, 1959, 1963a; Levin, 1962; Anderson and Phinney, 1967; Fricker et al., 1967; McConnell et al., 1967; Hanks and Anderson, 1969) benefitted from and built upon those of Urey. The successful missions to the Moon have provided a large amount of new data and strong constraints on the present-day and past temperatures in the lunar interior. These data have led to renewed interest in evolutionary and thermal models of the Moon (Urey and MacDonald, 1971;

Papanastassiou and Wasserburg, 1971a; Hays, 1972; Wood, 1972; Reynolds et al., 1972; McConnell and Gast, 1972; Toksöz et al., 1972c; Tozer, 1972; Hanks and Anderson, 1972). A common theme for most of these models has been to explain the early magmatism indicated by the lunar chronology and feldspathic crust, and the relatively cool present-day internal temperatures as suggested by the low electrical conductivity, high viscosity and paucity of tectonic activity.

In this paper, we present lunar thermal models based on all data (including Apollo 16) and realistic computational schemes. The constraints which are most important for evolution models are discussed in Section 2. The computational procedure and input parameters are given in Section 3. In Section 4, the thermal models are presented, and this is followed by a discussion of the results.

2. CONSTRAINTS ON THERMAL EVOLUTION MODELS

The data from lunar missions, especially those from Apollo experiments and samples, impose a wide range of constraints. Some of these (such as the electrical conductivity, heat flow, seismic velocities and tectonism) pertain to present-day temperatures inside the Moon. Some others (such as the history of differentiation and large scale magmatism, the existence of lunar mascons) indirectly point to the thermal state early in lunar history.

These data impose some boundary conditions, and at times, what might appear to be conflicting requirements on the past and present-day temperature models of the lunar interior. For example, interpretation of electrical conductivity appears to suggest relatively low temperatures (Sonnet et al., 1971, 1972; Dyal and Parkin, 1971; Dyal et al., 1972), in agreement with low seismicity (Latham et al., 1971, 1972a,b) and high viscosity (Baldwin, 1971; Arkani-Hamed, 1972). In contrast to such information is the high value of surface heat flow, 33 erg/cm^2-sec (Langseth et al., 1972). To better understand the limits of these major constraints, we discuss each one briefly, starting from those that relate to the initial conditions and going on to those that bear on the present-day temperatures.

2.1 Lunar Differentiation and Choonology

The Moon went through a period of major igneous activity and differentiation at an early age, during the first 1.5 billion years after formation. A feldspar-rich, 60-km thick crust has been detected by seismic studies in the Oceanus Procellarum region (Toksöz et al., 1972a, b, d). From the orbital x-ray fluorescence experiment (Adler et al., 1972a, b), from seismic velocities and from analyses of surface rocks at or derived from highland sites (Wood et al., 1970, 1971; Turkevich, 1971; Reid et al., 1972), the original crust is thought to be largely feldspathic in composition, gabbroic anorthosites with some norite (KREEP) component.

The chronology of lunar igneous activity starts from the formation of the original crust about 4.6 b.y. ago as deduced from model ages of lunar rocks and soils (Wasserburg and Papanastassiou, 1971; Tatsumoto, 1970; Tatsumoto et al., 1972; Silver, 1970). Although the record of pre-mare volcanism has been obscured by subsequent events, there is evidence for activity in the time between the appearance of the original crust and the filling of the mare basins. The formation ages of KREEP basalts are thought to be about 4.4 b.y. (Meyer et al., 1971; Papanastassiou and Wasserburg, 1972b; Schonfeld and Meyer, 1972). From these ages and Rb-Sr systematics (Papanastassiou and Wasserburg, 1971a) it can be concluded that the original crust differentiated before

the formation of KREEP basalts; i.e. within the first few hundred million years of lunar history.

To create a 60-km thick feldspathic crust requires the melting and differentiation of at least one half the total volume of the Moon (Wood et al., 1971). This is an important constraint which we will use in this study for the choice of the initial lunar temperature profile.

The igneous activity of the Moon which resulted in the filling of mare basins has been well documented by age-dating of lunar samples, particularly using Rb-Sr and Ar^{40}-Ar^{39} techniques (Papanastassiou and Wasserburg, 1970, 1971a, b, 1972a; Wasserburg and Papanastassiou, 1971; Turner, 1970, 1972; Turner et al., 1972; Husain et al., 1972a, b; York et al., 1972; and others). To date, the well-determined ages of mare basalts span a time interval between 3.16 and 3.71 b.y. ago (Wasserburg and Papanastassiou, 1971). Ages for Apollo 14 rocks are about 3.9 b.y. (Papanastassiou and Wasserburg, 1971b; Tatsumoto et al., 1972; Turner et al., 1972; Murthy et al., 1972) and ages of the crystalline rocks from Apollo 16 are greater than 3.8 b.y. (Schaeffer et al., 1972; Papanastassiou and Wasserburg, 1972b). Along with the 4.1 b.y. age (implacement or recrystallization) for the sample 15415 (Husain et al., 1972a) and 4.0 b.y. for 12013 (Papanastassiou and Wasserburg, 1971b) the above chronology indicates a continuum of activity in the Moon from the time of formation of the original crust to the time of the

implacement of mare basalts. The span of igneous activity is shown in Figure 1.

The failure to discover lunar igneous rocks younger than about 3.16 b.y. ago is an important constraint on the Moon's thermal history (Papanastassiou and Wasserburg, 1971a). If melting occurred since that time, it must have been very localized in extent or confined to depths in excess of several hundred kilometers.

2.2 Magnetism of Lunar Rocks

The lunar crust has an extensive but extremely variable magnetization. This has been verified by steady magnetic fields measured on the lunar surface (Dyal et al., 1970, 1972) and by magnetic anomalies observed by the Apollo 15 orbital magnetometer (Coleman et al., 1972). Further, many returned lunar samples display a fairly stable remanent magnetization (Strangway et al., 1970; Nagata et al., 1970, 1972; Helsley, 1970; Runcorn et al., 1970; Pearce et al., 1972; Collinson et al., 1972; Dunn and Fuller, 1972; and others). On the basis of these observations, which appear to require 1000-γ fields on the lunar surface during the emplacement of rocks spanning a time interval of almost 1 b.y., several workers (Runcorn et al., 1970; Pearce et al., 1971, and others) have suggested that the fields are internal in origin,

and thus indicate a molten conducting core or extensively molten pockets that could sustain dynamos between 3.2 and 4.0 b.y. ago. There is debate over this conclusion, and many other explanations of the magnetization, including fields associated with the earth, with the solar wind, or with shock or thermal effects, have been offered (Hide, 1972).

2.3 Lunar Mascons

The lunar mascons (Muller and Sjogren, 1968) are generally interpreted as arising from higher density mare basalts filling the basins excavated in the lower-density, anorthositic, initial crust (Sjogren et al., 1972). The time of the mascon formation then can be dated by the ages of mare basalts, and it is about 3.3 b.y. for Mare Imbrium (Wasserburg and Papanastassiou, 1971).

Thus the excess masses at mare basins have not been totally compensated over a three billion year time span. This requires that (1) at the time of the mascon emplacement (mare flooding) the lunar lithosphere was thick enough to support the loads (Urey, 1968; Solomon and Toksöz, 1972), and (2) the viscosity of the outer layers of the Moon must be about 10^{27} poise in order that the stresses have not relaxed since mascon formation (Urey and MacDonald, 1971; Baldwin,

1971; Arkani-Hamed, 1972). Even in the absence of water and volatiles, this high viscosity requires temperatures significantly lower than the melting curve in the outer several hundred kilometers of the Moon.

2.4 Electrical Conductivity and Present-Day Temperature

The electrical conductivity structure and related properties of the lunar interior have been deduced from the analysis of the Moon's response to transient magnetic field events using simultaneous magnetometer measurements on the anti-solar surface and in the free-streaming solar wind (Dyal and Parkin, 1971; Dyal et al., 1972), and analysis of the frequency-dependent transfer function of sunlit lunar surface to the free-stream magnetic field (Sonett et al., 1971, 1972). The electrical conductivity profiles were compared to laboratory measurements (England et al., 1968; Kobayashi and Maruyama, 1971) to show that temperatures in the outer 700 to 800 km of the Moon must be less than 1000°C (Sonett et al., 1971, 1972; Dyal and Parkin, 1971; Dyal et al., 1972). When more resistive material is assumed for interpreting the electrical conductivity (Duba et al., 1972; Anderson and Hanks, 1972; Housley and Morin,1972), temperatures in excess of 1000°C at depths greater than 350 km are possible. The suggested temperature limits of Dyal et al. (1972) and Duba et al. (1972) are shown in Figure 2. The

original temperature profile of Sonett et al. (1971) is also indicated.

One property common to all temperature models inferred from the electrical conductivity profile is that, at least in the outer 600 km, the temperatures are below the solidus of anhydrous basalts. This constraint must be satisfied by the thermal evolution models.

2.5 Seismic Velocities and Lunar Tectonism

The propagation of both compressional and shear waves in the lunar mantle requires that to the lowest limit of penetration of these waves the mantle must be solid (Toksöz et al., 1972b,d). From all evidence, moonquakes occur at depths as great as 800 km (Latham et al., 1972a,b). The lunar mantle must be solid at that depth to sustain the stresses that cause moonquakes. Nearly constant velocity in the upper mantle and the relatively high Q values (Latham et al., 1972b) further support the idea that the temperatures do not reach the melting point in the upper several hundred kilometers of the Moon.

The low level of tectonic activity on the Moon is also consistent with low temperatures and high strength in the lunar mantle. Although a number of small moonquakes have been recorded by the lunar seismic network, the total seismic

energy release within the Moon is about eight orders of magnitude less than that in the earth (Latham et al., 1972b). The absence of large moonquakes and the small amount of total energy release imply the absence of significant dynamic activity in the Moon.

2.6 Lunar Surface Heat Flux

The Apollo 15 heat flow value of 33 ± 5 ergs/cm^2-sec (Langseth et al., 1972) places narrow limits on the total radioactivity, and to a lesser extent, on the temperatures in the Moon. Caution is advisable in adopting this single measurement of heat flow as an average value for the Moon, especially in light of the variation of KREEP abundances detected by the orbital γ-ray experiment (Metzger et al., 1972). However, the absence of water and of extensive tectonic activity argues against strong local variability of sub-surface temperature and surface heat flux. The local variability of heat flow due to KREEP abundance is probably less than a factor of two. Thus we will utilize the measured heat flow value as a strong constraint in our thermal models.

3. MODEL PARAMETERS AND COMPUTATIONAL PROCEDURE

To calculate theoretically the thermal evolution of the Moon, one must specify the initial conditions, the sources of heat energy, and the mechanisms of heat transfer. The heat sources largely fall into two classes: those that affect only the very early history of the Moon and can be incorporated in the initial temperature distribution, and those that are important throughout lunar history. Heat transferred by lattice conduction and radiation can be fully accounted for; convective transport must be modeled in an approximate fashion. In this section we discuss in detail the necessary physical parameters and the particulars of our computational scheme.

3.1 Initial Temperature

The initial temperature distribution in the Moon is a function of the process of lunar formation and of the immediate environment of the Moon during and shortly after its origin. The evidence favoring an early episode of extensive near-surface melting in the Moon has been outlined above. Energy sources which might have heated the Moon to solidus or near-solidus temperatures include gravitational energy liberated during accretion, tidal dissipation, solar wind flux, short-lived radioactivity and adiabatic compression.

The latter two heat sources are likely of small consequence. The energy released by adiabatic compression in the Moon does not raise the temperature by more than a few tens of degrees. The effect of short-lived radioactive isotopes depends on the difference in time between nucleogenesis and the accretion of the Moon. The work of Schramm et al. (1970) has demonstrated that Al^{26}, previously thought to be perhaps the most likely radioactive source of substantial heat in the early history of the solar system (Fish et al., 1960), was not an important heat source in meteorites or in the Moon.

Both tidal dissipation and solar-wind flux can, under favorable circumstances, heat most or all of the Moon to melting temperatures. The effect on lunar temperature of tidal dissipation is small (Kaula, 1966) except when the Earth-Moon distance is only a few earth radii. This might have occurred during a short time interval after a capture event or after the Moon formed in close proximity to the earth (Singer, 1970). How this heat would be distributed with depth is uncertain, though we might qualitatively expect that most of the anelastic losses occur in those portions of the Moon that are at the highest temperatures before the tidal heating episode began. Heating of the Moon by the electric currents produced by a uni-polar generator driven by the solar wind

might be sufficient to melt the Moon if the Sun passed through a T-Tauri stage (Sonett and Colburn, 1970), otherwise the effect would be small. The likelihood that either of these energy sources was important is difficult to assess. Neither is explicitly included in our models, but recognition is made of the possibility that virtually the entire Moon could have melted early in its history.

Since it is reasonable to assume that the Moon formed by some accretion process, the most promising initial heat source for providing energy sufficient to melt the near-surface regions of the Moon is gravitational energy of accretion. Suppose that at some time t during accretion the proto-moon has radius r, and that during a time increment dt an outer shell of thickness dr is added to the lunar mass. Then the temperature T within that shell may be estimated by equating the additional gravitational potential energy to radiated energy plus heat:

$$\rho\frac{GM(r)}{r}\,dr = \varepsilon\sigma(T^4 - T_b^4)dt + \rho C_p(T - T_b)dr \qquad (1)$$

where ρ is the density of the accreting particles, G is the gravitational constant, $M(r)$ is the mass of the body within radius r, σ is the Stefan-Boltzman constant, ε is the emissivity (here taken equal to 1), and C_p is the

specific heat. T_b is the base temperature of the accreting particles, or the equilibrium temperature of the cloud of material within which the Moon formed. It will reflect whether the Moon formed as an aggregation of cold particles or condensed from a cooling gas; any effects of short-lived radioactivity can be included. T(r) can be calculated from Equation (1) by specifying ρ, C_p, T_b and the accretion rate dr/dt. An ad hoc but physically reasonable model for accretion was suggested by Hanks and Anderson (1969), and it has been adopted in this paper (Figure 3a). The accretion rate is expected to be slow when the Moon is just beginning to form, to increase as the accreted mass increases and then to taper off to zero as the material is depleted and the final lunar radius is achieved. These ideas are adequately represented by an accretion rate

$$dr/dt = ct^2 \sin \gamma t. \qquad (2)$$

The constants c and γ are determined from the Moon's final radius and the total duration of accretion.

If the accretion time is considered arbitrary, then it may be adjusted so as to give an initial temperature profile in excess of the solidus in the outer portions of the Moon. Using Equations (1) and (2), it can be shown that the near-

surface temperatures never exceed the basalt melting curve for accretion times greater than about 1000 years. This conclusion was also reached by Mizutani et al. (1972) from a more detailed analysis of the accretion process. One can estimate the duration of accretion by matching this model to the temperatures required to cause melting to specified depth. To differentiate a 60-km crust composed largely of feldspar probably requires melting to a depth of at least 500 km; i.e., involving at least half of the Moon's volume. This can be achieved if the total accretion time is about 100 years. The duration of accretion may be made arbitrarily long, however, by appropriately lowering the assumed emissivity of the lunar surface. The temperature profile resulting from Equations (1) and (2) for a 100-year accretion time is given in Figure 3b for two separate base temperatures; these profiles are adopted as starting temperatures in the calculations below.

3.2 Heat Sources

The most important heat source in the thermal history calculations is the heat generated by the long half-life radioactive isotopes U^{238}, U^{235}, Th^{232}, and K^{40}. The abundances of these isotopes measured in many lunar samples and the orbital γ-ray spectrometer results (Metzger et al., 1972) will

permit surface concentrations to be estimated over much of the Moon. While we can certainly conclude that the abundances at the Moon's surface must be considerably higher than at depth (Papanastassiou and Wasserburg, 1971a; and others), the bulk radioactivity of the Moon and the distribution of the radioactive isotopes with space and with time are difficult to constrain because of the complexities introduced by melting and crystal-liquid fractionation processes. To guide our estimates we consider the radioactivity measured in lunar samples and meteorites and the determination of heat flow at the Apollo 15 site.

In Figure 4, total K and U abundances are plotted for Apollo samples and some terrestrial basalts and meteorites. This figure is an updated version of one given by Hays (1972). For all lunar rocks (including basalts, breccias and soils) a constant K/U ratio of about 2000 is a good approximation although there are small, systematic departures from this average and the absolute abundances vary. This value compares with K/U = 10,000 for the earth and 80,000 for chondrites. The low K/U ratio for the Moon is linked to a general depletion of volatile elements (LSPET, 1969; 1972). Clearly neither terrestrial nor chondritic abundances should be used for lunar calculations. Chondrites can also be rejected on the basis of Rb abundances as a model for the

primitive lunar material (Papanastassiou and Wasserburg, 1971a). The Th/U ratio for lunar rocks is about 3.6 to 4.0, consistent with terrestrial and meteorite values.

As a possible handle on the average abundances of radioactive isotopes in the Moon we consider the achondrites, especially howardites and eucrites. A genetic relationship between achondrites and the Moon has been suggested by several investigators (Duke and Silver, 1967; and others). On the average, howardites have a U abundance of about .035 ppm while for (brecciated) eucrites, which are enriched in refractory elements, the value is about .130 ppm (Mason, 1971). It is of interest that the K/U ratio of eucrites is close to that for lunar rocks, while that of howardites (based on fewer samples) is somewhat higher.

In this paper we adopt the scaling of radioactive elements K/U = 2000 and Th/U = 4 throughout the present-day Moon. The average radioactivity of the Moon is then a single-valued function of the bulk uranium content. We consider models with U concentrations appropriate to howardites and eucrites and also concentrations set so as to match the Apollo 15 heat flow value of 33 erg/cm^2-sec (Langseth et al., 1972). The relevant decay constants, decay energies and isotopic abundances are taken from Clark (1966).

We should note that we ignore tidal dissipation as a possible long-term heat source of some significance. This

is done because of both the difficulty in quantitatively modeling the phenomenon and the uncertainty in past lunar orbit characteristics. As a result, we may be underestimating the heat generation in the early history of the lunar interior.

3.3 Thermal Conductivity and Other Parameters

In the absence of convective flow, transport of heat is governed by an effective thermal conductivity equal to the sum of lattice conduction and radiation terms. The effective thermal conductivity for some lunar and terrestrial materials as well as theoretical estimates (MacDonald, 1963b; Schatz and Simmons, 1972) are shown in Figure 5. Clearly, the values for lunar mare basalts should not be used since these rocks do not represent the bulk of lunar composition. (Ringwood and Essene, 1970; Gast, 1972). In this study we adopt the curve proposed by Schatz and Simmons (1972) for a hypothetical dunite in which radiative transfer is somewhat suppressed by grain-boundary extinction. At low temperatures, the conductivity is primarily due to lattice conduction and it decreases with increasing temperatures. At higher temperatures, the radiative term, roughly linear with temperature, is dominant. Previous studies of thermal evolution of the Moon have generally used MacDonald's formulation and

assumed that the opacity is constant with temperature. This gives the radiative contribution a cubic dependence on temperature. The pressure effects are probably small at lunar pressures and are neglected. In the calculations an analytic expression has been used for the curve marked "S" and conductivity is adjusted at each step for appropriate temperature.

The melting curve, surface temperature, specific heat, heat of fusion, and density must be specified for calculations. The melting curve used in this paper is the solidus from the melting range of mare basalts (Ringwood and Essene, 1970). We used only one curve to specify both partial and total melting. A constant density of 3.34 g/cm^3 and a constant surface temperature of -20°C (Langseth et al., 1972) have been used. A summary of the parameters common to all models is given in Table I.

3.4 Computational Technique

The thermal calculations are carried out for a spherically symmetric moon (parameters varying with radius only at a given time), taking into account melting, simulated convection and differentiation. In this section these steps are described briefly.

Temperature evolution models are calculated using the finite-difference solution of the heat conduction equation

$$C_p \rho \frac{\partial T}{\partial t} = \frac{1}{r^2} \frac{\partial}{\partial r} \left(r^2 K \frac{\partial T}{\partial r} \right) + H(r,t) \qquad (3)$$

where C_p is the specific heat, ρ is the density, T is the temperature, r is the radius, K is the thermal conductivity and $H(r,t)$ is the heat-source term, which in general depends on radius and on time. K is taken to be temperature-dependent as discussed above.

The finite-difference analog of Equation (3) which conserves heat flux is

$$T_n^{m+1} = T_n^m + \frac{\alpha}{n^2 p^2} \left[(n + 1/2)^2 \frac{(K_{n+1}^m + K_n^m)}{2} (T_{n+1}^m - T_n^m) - (n - 1/2)^2 \frac{(K_n^m + K_{n-1}^m)}{2} (T_n^m - T_{n-1}^m) \right] + \alpha H_n^m \qquad (4)$$

where

$$p = \Delta r \qquad \alpha = \Delta t / C_p \rho$$

$$r = np \qquad T_n^m = T(np, m\Delta t)$$

$$t = m\Delta t$$

Since the scheme is explicit, a stability condition relating the time increment and the grid spacing must be fulfilled. Questions of stability, convergence and accuracy of Equation

(4) are discussed fully by Toksöz et al. (1972c). The stability condition which is developed in the appendix of that paper is

$$\Delta t < \frac{C_p \rho \Delta r^2}{2K_{max}} \quad \frac{n^2}{(n + 1/2)^2} \tag{5}$$

where K_{max} is the maximum value of the conductivity at a given time step. The time increment is computed at each time step using Equation (5) with a factor of 4 instead of 2 in the denominator. Generally a grid spacing of 20 km is used.

To avoid a temperature singularity at the center of the Moon ($r = 0$), the solution was started at $r = 20$ km. Heat flux was taken as zero at the grid point corresponding to $r = 20$ km by setting $T_1^n = T_2^n$ where T_1^n is the temperature at $r_1 = 20$ km and T_2^n is the temperature at $r_2 = r_1 + r$. Temperature was held constant (-20°C) at the surface of the Moon. Surface heat flux was computed by adding the heat flow at the boundary between the upper two finite-difference cells to the steady-state heat flow due to heat production in the uppermost half-cell; the former quantity was corrected for the slightly greater area of the lunar surface.

Simulation of Melting and Convection. The effects of melting and convection on temperature were modeled using a technique described by Reynolds et al. (1966). In this technique, the temperature profile at some time $m\Delta t$ is compared with a given melting-point curve. If the temperature T_n^m is above the melting point, T_n, the temperature increment above the melting point $(T_n^m - T_n)$ is converted to its heat equivalent, ΔH, by dividing by the specific heat and the density. If ΔH is not equal to or greater than a specified heat of fusion, the material is taken as partially molten, the temperature at point $n\Delta r$ is held at T_n and another iteration in time performed. The material at point $n\Delta r$ remains partially molten at temperature T_n until the sum of the ΔH's from $m\Delta t$ to some $(m + p)\Delta t$ equals the heat of fusion. At this point in time the material is completely molten and temperature is allowed to increase above T_n. Provision is made for the phase change to run either way so that molten material may solidify by releasing heat equal to this heat of fusion.

Simulation of convection of molten material follows the technique outlined above except that once the material has become completely molten, temperature is held at the melting point. Any increase in temperature which would raise the temperature above the melting point is converted

into its heat equivalent and transferred upward to the next grid point as an equivalent temperature increment due to convection. The conversion to equivalent heat and back to temperature is necessary since the volume element increases with radius.

The main assumption underlying this technique is that convection occurs on complete melting and limits the temperature in the region of complete melting to the melting temperature. This scheme accounts for the transfer of heat which would have taken place under convection without actually using the mass transfer terms in the equation. Convection in a partial melt can be approximated by adopting an appropriately lower heat of fusion. Convection by solid-state creep can be roughly approximated by redefining the "solidus" (see below).

Differentiation. In the regions where melting occurs, the magma would be enriched with U, Th and K and eventually would transfer these heat sources toward the surface. To account for this, at discrete time steps all heat sources to the depth of deepest melting are differentiated upwards. Where no melting has occurred, no differentiation is carried out and initial radioactive abundances are maintained.

The concentration of radioactive heat sources after

each differentiation is assumed to decrease exponentially with depth (Lachenbruch, 1968):

$$H(r) = A_o \exp\left[-\frac{(R-r)}{h}\right] \qquad (6)$$

where A_o is the surface abundance and R is the lunar radius. The skin depth h is presumed to decrease with time. The skin depth of the last differentiation is set so that the present-day radioactivity at the lunar surface equals that of the average of soil samples from mare sites, about 1 ppm (Silver, 1970; 1972; and Figure 2), with the exception that the skin depth is never taken less than the finite-difference grid size. Differentiation is carried out in 1 to 4 steps, starting with h in the range 100 to 200 km and ending with h = 20 to 60 km. The time of last differentiation is taken to lie in the range 3.0 to 3.7 b.y. ago. Thermal models calculated by these prodedures are discussed in the next section.

4. TEMPERATURE MODELS

In this section we present specific models for the thermal evolution of the Moon. An assortment of initial conditions and bulk concentrations of radioactive isotopes are employed both to demonstrate the effect such parameters have on thermal history and to assess whether the constraints discussed in Secion 2 can limit models of lunar formation or constitution. A quick overview of all models presented below is given in Table II.

We begin by considering the evolution in a uniform, initially cold (T = 0°C everywhere) Moon. While such a model is unrealistic, it is a standard output of those presenting thermal history calculations and serves to verify the computational scheme. In Figure 6 is shown the present-day temperature profile in an initially cold Moon as a function of the present-day concentration or uranium. For $U \leq 37$ ppb (parts per billion), the temperature is below the basalt solidus throughout the Moon and has been so since the Moon's formation. Clearly models such as those in Figure 6 that begin with an everywhere-cold moon cannot generate enough heat from long-lived radioactivity alone to provide the necessary melting and differentiation in the Moon's upper few hundred kilometers.

As a model with an antithetical initial state, we show the thermal evolution in an initially molten Moon in Figure 7. As mentioned in Section 3, complete melting in the Moon shortly after its formation could have been produced by close approach of the Moon to the Earth or by immersing the Moon in the solar-wind flux of a Sun passing through a T-Tauri phase. Upon complete melting in the model, all the radioactive elements are concentrated near the lunar surface. In such a model, iron or dense iron compounds (such as FeS) would differentiate to the Moon's center to form a core. Because of the depletion of heat sources in the interior and because of the efficient heat transfer in molten regions, the Moon cools relatively rapidly and is everywhere solid after 2 billion years. At present the Moon is cooling throughout; the average concentration of uranium is 60 ppb (corresponding, perhaps, to a mixture of howardite and eucrite compositions) and the surface heat flow is 29 erg/cm^2-sec, within the range of uncertainty of the Apollo 15 measurement. A similar model with less radioactivity was given in Toksöz et al. (1972c).

Though early melting throughout the Moon can probably be produced only by a catastrophic event, the normal process of accretion can yield melting of the near-surface regions sufficient to segregate an early crust and to

differentiate the radioactive elements. We now consider a series of thermal history models with one of the initial temperature profiles from Figure 3. The primary variable of interest will be the concentration of radioactive heat sources.

A thermal evolution model with average present-day uranium concentration equal to that of howardites (35 ppb) is shown in Figure 8. The initial temperature profile is derived from Equations (1) and (2) with a base temperature of 500°C and a total accretion time of 100 years. Melting initially extends to 600 km depth, and the interior is relatively cool. In this model, the outer portions of the Moon cool monotonically with time while the interior progressively warms. Between 0.5 and 1.5 b.y. after lunar origin, a solid lithosphere on the Moon grows from 150 to 310 km in thickness. Partial melting occurs at some depth over the entire lunar history, though upwards differentiation of radioactivity was arbitrarily stopped in the model 3.7 b.y. ago. The inner 950 km is partially or completely molten at present, with heat coming from undifferentiated material below 900 km depth. The average heat flow at the Moon's surface in the model is currently 18 erg/cm^2-sec.

In Figure 9 is given a thermal evolution model with the same initial temperature profile as in Figure 8 but

with an average present-day concentration of uranium equal to that of eucrites (130 ppb). In this model, the entire Moon below 50 km depth becomes completely or partially molten within 0.5 b.y. after lunar formation. The lunar lithosphere grows very slowly; at 1.5 b.y. it is only 70 km thick. Such a value is probably much too small if the mascon-generated stresses were supported in the lithosphere. At the present time in the model, the Moon is partially or completely molten below 200 km depth, except for a small solid core, and the surface heat flow is 55 erg/cm^2-sec. Models similar to that of Figure 9 have been proposed elsewhere (Hanks and Anderson, 1972).

We feel that the thin lithosphere in the first 3 b.y. of lunar history, the high heat-flow, and the difficulty of explaining moonquakes 700 to 800 km deep make such a model an unlikely candidate. While eucrites might be linked to lunar rocks, the average radioactivity of the Moon cannot be as high as that of eucrites.

Since the present-day heat flow scales approximately as average uranium concentration in thermal history models in which other parameters are held fixed (Solomon and Toksöz, 1972), we can determine the radioactivite element content necessary to match the single measurement of heat flow at the Moon's surface, 33 ± 5 erg/cm^2-sec (Langseth et al.,

1972). We should caution that the γ-ray spectrometer results (Metzger et al., 1972) indicate that the region surrounding the Apollo 15 site is significantly more radioactive than most of the lunar surface, so the average heat flow on the Moon may be less than the Apollo 15 value.

A model giving a present-day surface heat flow of 33 erg/cm^2-sec is shown in Figure 10. The initial temperature profile is from the accretion model of Figure 3; a base temperature of 0°C and a total accretion time of 100 years were used. The last differentiation of radioactive heat sources was taken to occur 3.7 b.y. ago. The present-day uranium concentration averages to 70 ppb. The time sequence of melting in the model is shown in Figure 11.

It may be seen that the model satisfies the major constraints upon lunar evolution. The zone of melting deepens with time. The lithosphere during the first 2 b.y. thickens at the rate of about 160 km/b.y. In particular, the shallowest melting progresses from 155 to 245 km depth during the period of mare filling, in agreement with the depth of origin of mare basalts (Ringwood and Essene, 1970) and with the need for a reasonably thick lithosphere to sustain the stresses associated with mascon gravity anomalies. Between 1 and 2 b.y. in the model, a convecting core develops due to the undifferentiated and relatively radioactive primordial

material near the Moon's center. The convecting core grows to a radius of 1200 km at 3 b.y. and then slowly shrinks as the concentration of heat sources decays with time. The Moon is molten below 580 km depth at present in the model. This is in apparent conflict with the occurrence of moonquakes at 700 to 800 km depth, unless such events are not representative of the average Moon, and implies that a Moon with somewhat less radioactivity, and somewhat lower heat flow, is more appropriate. The feature of a molten convecting core is absent in models (such as those of Figures 7 and 9) in which the Moon differentiates completely and concentrates all of the radioactive heat sources toward the surface.

Models similar to that of Figure 10 except starting at a higher base temperature and involving more recent segregation of radioactive heat sources from the partially molten regions of the Moon can match the Apollo 15 heat flow value with a somewhat lower average uranium concentration. With a range of initial temperature profiles from accretion models, a present-day surface heat flow of 33 ± 5 erg/cm^2-sec implies an average uranium concentration in an originally homogeneous Moon of 65 ± 15 ppb (Solomon and Toksöz, 1972).

The hypothesis of a stable magnetic dynamo in a liquid, iron-rich lunar core from 3 to 4 b.y. ago would require the deep interior of the Moon to begin at temperatures at least in excess of the Fe-FeS eutectic or to have formed at lower temperatures with substantial radioactivity at depth (cf. Brett, 1972). The thermal history models of Figures 7 and 10 are consistent with this idea. In Figure 10, temperatures .5 b.y. after lunar origin exceed the Fe-FeS eutectic (Brett and Bell, 1969). throughout most of the Moon. Thus core formation by melting, sinking and aggregation of iron-rich droplets is achieved prior to the formation of the oldest lunar rocks possessing remanent magnetization.

Except for models which are initially molten and segregate all radioactivity upwards toward the surface, thermal history models beginning with uniform distribution of radioactivity and satisfying the Apollo 15 heat flow value are presently partially molten or at temperatures within 100°C of the solidus at depths below about 500 km (Solomon and Toksöz, 1972). Thus for such models the heat flow and deep moonquakes are difficult to reconcile. One means of avoiding the dilemma is to make an additional postulate: the concentration of radioactivity in the Moon decreases with depth as a primary feature associated with chemically inhomogeneous accretion, as suggested by several investigators (Gast, 1972; Green et al., 1972; and others).

Shown in Figures 12 and 13 is a thermal history model following closely one proposed by McConnell and Gast (1972). The radioactivity is stratified: if no differentiation had been allowed, the present-day abundance of uranium would be 120 ppb in the uppermost 200 km, 50 ppb in the next 250 km, and 10 ppb in the remainder of the Moon. The average present-day uranium concentration is thus 53 ppb. The ratios K/U and Th/U are held constant. The initial temperature profile is from the accretion model of Hanks and Anderson (1969) with a base temperature of 0°C and an accretion time of 1000 years. The initial temperature barely exceeds the solidus between 40 and 140 km depth; a shorter accretion time would have raised the initial temperature. Differentiation of radioactive elements is accomplished in four discrete steps between 0 and .9 b.y. The temperature evolution in the upper few hundred kilometers of the Moon is similar to models of comparable bulk radioactivity discussed earlier. The present-day heat flow is 32 erg/cm^2 sec and the Moon is everywhere at least 200°C below the solidus.

The difference in the behavior of the model of Figure 12 from those discussed earlier is that the center of the Moon in this model is tacitly assumed to have been relatively depleted in radioactive elements at cold temperatures. Thus the lunar center heats slowly and the Moon is everywhere

solid at present. Whether a cold accretion can accompany primary chemical layering is an important question. Such an origin is incompatible with a molten iron-rich core at an early stage in lunar history. If questions such as these can be resolved and if the Apollo 15 heat flow value holds up, then the temperatures in the deep lunar interior, if discernible, offer the only possible means by which thermal history calculations can distinguish primary accretional zoning from extensive in situ differentiation.

In all of the models above, heat transfer by convective mass transport was ignored at sub-solidus temperatures. This may be quite unreasonable, particularly for the deep lunar interior. Several authors (Runcorn, 1962; Kopal, 1962; Turcotte and Oxburgh, 1969b; Tozer, 1972) have argued that convection by solid-state creep should be at least as efficient a heat-transfer mechanism as lattice conduction and radiation at temperatures considerably below the solidus. Inclusion of the effect of solid-state creep should produce present-day temperature profiles that are cooler than those given above. Tozer (1972), in fact, has stated that the relatively cool lunar temperature profiles proposed by Sonett et al. (1971) and others interpreting the electrical conductivity distribution are a natural consequence of a convecting interior.

While we do not wish to attempt to solve the complete problem of thermal evolution in a realistically convecting Moon, we can make some simplifying assumptions that allow us to make a rough estimate of the effect of solid-state creep on our thermal history calculations. Convective solutions to the present day temperature profile in the Moon generally show a stable shell of a few hundred kilometers overlying a convecting interior of nearly constant viscosity (Turcotte and Oxburgh, 1969b; Tozer, 1972), a consequence of the low pressures and small adiabatic temperature gradient in the Moon. We therefore postulate in our thermal evolution models that solid-state creep will be an efficient heat transfer mechanism when the temperature in the bulk of the lunar interior is such that the viscosity exceeds a critical value. This temperature is essentially the 'stabilization temperature' of Tozer (1970, 1972). Convection is simulated, as before, as a 100-percent-efficient process: all heat in excess of that required to maintain the viscosity of the material at the critical value is transferred upward in the model. We assume a rheology proposed by Turcotte and Oxburgh (1969a) for diffusion creep in the earth's mantle; whether or not this is compatible with our assumed solidus is debatable. Thus we ignore the probable complication of non-Newtonian viscosity (Weertman, 1970), an uncertain

increase in viscosity associated with the depletion of volatiles in the Moon relative to the earth (Orowan, 1965), and the apparent conflict between geophysical constraints on the rheology of the earth's mantle and presently available laboratory measurements of high-temperature creep in rocks (Goetze and Brace, 1972). For the critical value of viscosity we chose 10^{24} poise. This value is an estimate, obtained from marginal stability theory in a uniform gravitating sphere, of the maximum value permissible if the Moon is currently convecting (Turcotte and Oxburgh, 1969b). We found that using lower values for the critical viscosity did not alter significantly the thermal evolution from models similar in all respects but neglecting solid-state creep; this is because the temperatures at which such viscosities are reached, according to the viscosity-temperature relationship of Turcotte and Oxburgh (1969a), are near the basalt solidus. Tozer (1972) has proposed that a viscosity near 10^{21} poise and less creep resistant rheologies are more appropriate.

A thermal evolution model following such a scheme is shown in Figure 14. This model begins with an accretion-generated initial temperature curve from Figure 3, and is treated as all earlier models for the first 2 billion years. At that time, almost all of the Moon below 250 km depth is at a temperature high enough to give a viscosity less than

10^{24} poise. Although the viscosity was less than that value over a more limited depth range at times less than 2 b.y., we argue that solid-state creep was probably unimportant at these early stages by appealing qualitatively to the very strong dependence of the Rayleigh number, a criterion for hydrodynamic instability, on the characteristic length (depth interval) of the convective cell (e.g. Turcotte and Oxburgh, 1969b). After 2 b.y. in the model, the temperature in the convecting interior is stabilized at that temperature necessary to maintain a viscosity of 10^{24} poise; the gradient is slightly superadiabatic. All excess heat is transferred to the non-convecting outer shell, which is slowly cooling and thickening with time. The present-day average uranium concentration is 23 ppb and the heat flow at the lunar surface in this model is 13 erg/cm^2 sec. For a higher uranium concentration, the heat flow will be higher and the only change in the present-day temperature profile from that given in Figure 14 will be a slightly thinner lithosphere.

All of the thermal models discussed above and summarized in Table II demonstrate the importance of the initial conditions and composition for the evolution and present-day properties of the Moon. With additional data, it is probable that the early history of the Moon can be reasonably well understood from computations such as these.

5. CONCLUSIONS

A wide assortment of data now constrain models of the evolution of the Moon's interior. We have quantitatively examined some of these constraints and the suite of lunar thermal models consistent with them. From these we can conclude:

(1) Models of the thermal evolution of the Moon that fit the chronology of surface igneous activity, the need for a cool, rigid lithosphere since the formation of mascons, and the surface concentrations of radioactive elements all require extensive differentiation and upwards concentration of radioactive heat sources early in lunar history. This differentiation may be either a primary accretional feature or a product of nearly Moon-wide melting.

(2) A model of the Moon which is initially hot, and extensively or totally molten can satisfy most of the constraints described in Section 2. A totally molten Moon cools faster than other models due to complete and early differentiation.

(3) The early history of the Moon is characterized by strong magmatic and tectonic activity. Convection must have played an important role in lunar differentiation and

dynamics. Patterns of convective flow will introduce lateral heterogeneities which cannot be modeled with a radially symmetric Moon.

(4) If the Apollo 15 heat flow value of 33 ± 5 erg/cm^2-sec (Langseth et al., 1972) is representative of the Moon, then the average concentration of uranium in the Moon is currently 65 ± 15 ppb, assuming the Th/U and K/U ratios of lunar surface rocks hold throughout the interior. This uranium concentration is intermediate between the average values for howardites and eucrites, although closer to howardites. Such an achondritic composition would satisfy the bulk of the geochemical data as well as the mass and moment of inertia constraints for the Moon.

(5) Thermal history calculations are only marginally useful for distinguishing between primary accretional zoning of radioactive heat sources and an early melting episode including extensive differentiation. The major difference between the two sets of models is the temperature of the innermost 1000 km, a region of the Moon for which independent information from seismic velocity or electrical conductivity studies is currently lacking.

(6) Better understanding of the thermal evolution of the

Moon requires further constraints on heat sources, improved computational techniques for convection models, and additional data limiting present-day internal temperatures.

ACKNOWLEDGMENTS

We thank David Johnston and John Minear for their contributions to the computations. This research was supported by NASA Grant NGL 22-009-187 and by NASA Grant NAS 9-12334.

REFERENCES

Adler, I., Trombka, J., Gerard, J., Lowman, P., Schmadebeck, R., Blodget, H., Eller, E., Yin, L., Lamothe, R., Gorenstein, P., and Bjorkholm, P.: 1972a, Science 175, 436.

Adler, I., Trombka, J., Gerard, J., Lowman, P., Schamdebeck, R., Blodget, H., Eller, E., Yin, L., Lamothe, R., Osswald, G., Gorenstein, P., Bjorkholm, P., Gursky, H., and Harris, B.: 1972b, Science 177, 256.

Anderson, D.L. and Phinney, R.A.: 1967, in Mantles of the Earth and Terrestrial Planets, (ed. by S.K. Runcorn), Interscience, p. 113.

Anderson, D.L. and Hanks, T.C.: 1972, Science, in press.

Arkani-Hamed, J.: 1972, The Moon, in press.

Baldwin, R.B.: 1971, Phys. Earth Planetary Int. 4, 167.

Brett, R.: 1972, Geochim. Cosmochim. Acta, in press.

Brett, R. and Bell, P.M.: 1969, Earth Planetary Sci. Letters 6, 479.

Clark, S.P., Jr.: 1966, Handbook of Physical Constants, Geol. Soc. Am. Memoir 97.

Coleman, P.J., Jr., Lichtenstein, B.R., Russell, C.T., Sharp, L.R., and Schubert, G.: 1972, Geochim. Cosmochim. Acta, Suppl. 3, 2271.

Collinson, D.W., Runcorn, S.K., Stephenson, A., and Manson, A.J.: 1972, Geochim. Cosmochim. Acta, Suppl. 3, 2343.

Cremers, C.J.: 1971, AIAA J. 9, 2180.

Duba, A., Heard, H.C., and Schock, R.N.: 1972, Earth Planetary Sci. Letters 15, 301.

Duke, M.B. and Silver, L.T.: 1967, Geochim. Cosmochim. Acta 31, 1637.

Dunn, J.R. and Fuller, M.: 1972, Geochim. Cosmochim. Acta, Suppl. 3, 2363.

Dyal, P. and Parkin, C.W.: 1971, Geochim. Cosmochim. Acta, Suppl. 2, 2391.

Dyal, P., Parkin, C.W., and Sonett, C.P.: 1970, Science 169, 762.

Dyal, P., Parkin, C.W., and Cassen, P.: 1972, Geochim. Cosmochim. Acta, Suppl. 3, 2287.

England, A.W., Simmons, G., and Strangway, D.: 1968, J. Geophys. Res. 73, 3219.

Fish, R.A., Goles, G.G., and Anders, E.: 1960, Astrophys. J. 132, 243.

Fricker, P.E., Reynolds, R.T., and Summers, A.L.: 1967, J. Geophys. Res. 72, 2649.

Gast, P.W.: 1972, The Moon 5, 121.

Goetze, C. and Brace, W.F.: 1972, Tectonophysics 13, 583.

Green, D.H., Ringwood, A.E., Ware, N.G., and Hibberson, W.O.: 1972, Geochim. Cosmochim. Acta, Suppl. 3, 197.

Hanks, T.C. and Anderson, D.L.: 1969, Phys. Earth Planet. Interiors 2, 19.

Hanks, T.C. and Anderson, D.L.: 1972, Phys. Earth Planet. Interiors, in press.

Hays, J.F.: 1972, Phys. Earth Planet. Interiors 5, 77.

Helsley, C.E.: 1970, Geochim. Cosmochim. Acta, Suppl. 1, 2213.

Hide, R.: 1972, The Moon 4, 39.

Horai, K., Simmons, G., Kanamori, H., and Wones, D.: 1970, Geochim. Cosmochim. Acta, Suppl. 1, 2243.

Housley, R.M. and Morin, F.J.: 1972, The Moon 4, 35.

Husain, L., Schaeffer, O.A., and Sutter, J.F.: 1972a, Science 175, 428.

Husain, L., Schaeffer, O.A., Funkhouser, J., and Sutter, J: 1972, Geochim. Cosmochim. Acta, Suppl. 3, 1557.

Kaula, W.M.: 1966, in The Earth-Moon System, (ed. by B.G. Mardsen and A.G.W. Cameron), Plenum Press, New York, p. 46.

Kobayashi, Y. and Maruyama, H.: 1971, Earth Planetary Sci. Letters 11, 415.

Kopal, Z.: 1962, Planetary Space Sci. 9, 625.

Lachenbruch, A.H.: 1968, J. Geophys. Res. 73, 6977.

Langseth, M.G., Jr., Clark, S.P., Jr., Chute, J.L., Jr., Keihm, S.J., and Wechsler, A.E.: 1972, The Moon 4, 390.

Latham, G., Ewing, M., Dorman, J., Lammlein, D., Press, F., Toksöz, N., Sutton, G., Duennebier, F., and Nakamura, Y.: 1971, Science 174, 687.

Latham, G., Ewing, M., Dorman, J., Lammlein, D., Press, F., Toksöz, N., Sutton, G., Duennebier, F., and Nakamura, Y.: 1972a, The Moon 4, 373.

Latham, G., Ewing, M., Dorman, J., Lammlein, D., Press, F., Toksöz, N., Sutton, G., Duennebier, F., and Nakamura, Y.: 1972b, Geochim. Cosmochim. Acta, Suppl. 3, 2519.

Levin, B.J.: 1962, in The Moon, (ed. by Z. Kopal and Z.K. Mikhailov), Academic Press, New York, p. 157.

LSPET (Lunar Sample Preliminary Examination Team): 1969, Science 165, 1211.

LSPET (Lunar Sample Preliminary Examination Team): 1972, Science 175, 363.

LSPET (Lunar Sample Preliminary Examination Team): 1973, Science, in press.

MacDonald, G.J.F.: 1959, J. Geophys. Res. 64, 1967.

MacDonald, G.J.F.: 1963a, Space Sci. Rev. 2, 473.

MacDonald, G.J.F.: 1963b, Rev. Geophys. 1, 587.

Mason, B.: 1971, Handbook of Elemental Abundances in Meteorites, Gordon and Breach, New York.

McConnell, R.K., Jr. and Gast, P.W.: 1972, The Moon 5, 41.

McConnell, R.K., Jr., McClaine, L.A., Lee, D.W., Aronson, J.R., and Allen, R.V.: 1967, Rev. Geophys. 5, 121.

Metzger, A.E., Trombka, J.I., Peterson, L.E., Reedy, R.C., and Arnold, J.R.: 1972, Geochim. Cosmochim. Acta, Suppl. 3, v. 3 frontispiece.

Meyer, C., Jr., Brett, R., Hubbard, N.J., Morrison, D.A., McKay, D.S., Aitken, F.K., Takeda, H., and Schonfeld, E.: 1971, Geochim. Cosmochim. Acta, Suppl. 2, 393.

Mizutani, H., Matsui, T., and Takeuchi, H.: 1972, The Moon 4, 476.

Muller, P.M. and Sjogren, W.L.: 1968, Science 161, 680.

Murase, T. and McBirney, A.R.: 1970, Science 170, 165.

Murthy, V.R., Evensen, M.M., Jahn, B., and Coscio, M.R., Jr.: 1972, Geochim. Cosmochim. Acta, Suppl. 3, 1503.

Nagata, T., Ishikawa, Y., Kinoshita, H., Kono, M., Syono, Y., and Fisher, R.M.: 1970, Geochim. Cosmochim. Acta, Suppl. 1, 2325.

Nagata, T., Fisher, R.M., and Schwerer, F.C.: 1972, The Moon 4, 160.

Orowan, E.: 1965, Phil. Trans. Roy. Soc. London, Ser. A, 258, 284.

Papanastassiou, D.A. and Wasserburg, G.J.: 1970, Earth Planetary Sci. Letters 8, 269.

Papanastassiou, D.A. and Wasserburg, G.J.: 1971a, Earth Planetary Sci. Letters 11, 37.

Papanastassiou, D.A. and Wasserburg, G.J.: 1971b, Earth Planetary Sci. Letters 12, 36.

Papanastassiou, D.A. and Wasserburg, G.J.: 1972a, Earth Planetary Sci. Letters 13, 368.

Papanastassiou, D.A. and Wasserburg, G.J.: 1972b, Earth Planetary Sci. Letters, 16, in press.

Pearce, G.W., Strangway, D.W., and Larson, E.E.: 1971, Geochim. Cosmochim. Acta, Suppl. 2, 2451.

Pearce, G.W., Strangway, D.W., and Gose, W.A.: 1972, Geochim. Cosmochim. Acta, Suppl. 3, 2449.

Reid, A.M., Warner, J., Ridley, W.I., Johnston, D.A., Harmon, R.S., Jakes, P., and Brown, R.W.: 1972, Geochim. Cosmochim. Acta, Suppl. 3, 363.

Reynolds, R.T., Fricker, P.E., and Summers, A.L.: 1966, J. Geophys. Res. 71, 573.

Reynolds, R.T., Fricker, P.E., and Summers, A.L.: 1972, in Thermal Characteristics of the Moon, (ed. by J.W. Lucas), M.I.T. Press, Cambridge, Massachusetts, p. 303.

Ringwood, A.E. and Essene, E.: 1970, Geochim. Cosmochim. Acta, Suppl. 1, 769.

Runcorn, S.K.: 1962, Nature 195, 1150.

Runcorn, S.K., Collinson, D.W., O'Reilly, W., Battey, M.H., Stephenson, A., Jones, J.M., Manson, A.J., and Readman, P.W.: 1970, Geochim. Cosmochim. Acta, Suppl. 1, 2369.

Schonfeld, E. and Meyer, C., Jr.: 1972, Geochim. Cosmochim. Acta, Suppl. 3, 1397.

Schatz, J.F. and Simmons, G.: 1972, J. Geophys. Res. 77, in press.

Schramm, D.N., Tera, F., and Wasserburg, G.J.: 1970, Earth Planetary Sci. Letters 10, 44.

Silver, L.T.: 1970, Geochim. Cosmochim. Acta, Suppl. 1, 1533.

Silver, L.T.: 1972, in Lunar Science-III, Revised Abstracts of Papers Presented at the Third Lunar Science Conference, (ed. by C. Watkins), Lunar Science Institute, Houston, Texas, 704.

Singer, S.F.: 1970, EOS, Trans. Amer. Geophys. Union 51, 637.

Sjogren, W.L., Muller, P.M., and Wollenhaupt, W.R.: 1972, The Moon 4, 411.

Solomon, S.C. and Toksöz, M.N.: 1972, Phys. Earth Planet. Interiors 5, in press.

Sonett, C.P. and Colburn, D.S.: 1970, The Moon 1, 483.

Sonett, C.P., Colburn, D.S., Dyal, P., Parkin, C.W., Smith, B.F., Schubert, G., and Schwartz, K.: 1971, Nature 230, 359.

Sonett, C.P., Smith, B.F., Colburn, D.S., Schubert, G., and Schwartz, K.: 1972, Geochim. Cosmochim. Acta, Suppl. 3, 2309.

Strangway, D.W., Larson, E.E., and Pearce, G.W.: 1970, Geochim. Cosmochim. Acta, Suppl. 1, 2435.

Tatsumoto, M.: 1970, Geochim. Cosmochim. Acta, Suppl. 1, 1595.

Tatsumoto, M., Hedge, C.E., Doe, B.R., and Unruh, D.M.: 1972, Geochim. Cosmochim. Acta, Suppl. 3, 1531.

Toksöz, M.N., Press, F., Anderson, K., Dainty, A., Latham, G., Ewing, M., Dorman, J., Lammlein, D., Sutton, G., Duennebier, F., and Nakamura, Y.: 1972a, Science 176, 1012.

Toksöz, M.N., Press, F., Anderson, K., Dainty, A., Latham, G., Ewing, M., Dorman, J., Lammlein, D., Nakamura, Y., Sutton, G., Duennebier, F.: 1972b, The Moon 4, 490.

Toksöz, M.N., Press, F., Dainty, A., Anderson, K., Latham, G., Ewing, M., Dorman, J., Lammlein, D., Sutton, G., and Duennebier, F.: 1972d, Geochim. Cosmochim. Acta, Suppl. 3, 2527.

Toksöz, M.N., Solomon, S.C., Minear, J.W., and Johnston, D.H.: 1972c, The Moon 4, 190 and 5, 249.

Tozer, D.C.: 1970, Phys. Earth Planetary Int. 2, 393.

Tozer, D.C.: 1972, The Moon 5, 90.

Turcotte, D.L. and Oxburgh, E.R.: 1969a, J. Geophys. Res. 74, 1458.

Turcotte, D.L. and Oxburgh, E.R.: 1969b, Nature 223, 250.

Turkevich, A.L.: 1971, Geochim. Cosmochim. Acta, Suppl. 2, 1209.

Turner, G.: 1970, Geochim. Cosmochim. Acta, Suppl. 1, 1665.

Turner, G.: 1972, Earth Planetary Sci. Letters 14, 169.

Turner, G., Huneke, J.C., Podosek, F.A., and Wasserburg, G.J.: 1972, Geochim. Cosmochim. Acta, Suppl. 3, 1589.

Urey, H.C.: 1951, Geochim. Cosmochim. Acta 1, 209.

Urey, H.C.: 1952, The Planets, Their Origin and Development, Yale University Press, New Haven, Connecticut.

Urey, H.C.: 1955, Proc. Natl. Acad. Sci. U.S. 41, 127.

Urey, H.C.: 1957, in Physics and Chemistry of the Earth 2, (ed. by L.H. Ahrens, F. Press, K. Rankama, and S.K.

Runcorn), Pergamon Press, New York, p. 46.

Urey, H.C.: 1962, in Physics and Astronomy of the Moon, 1st Ed., (ed. by Z. Kopal), Academic Press, New York, p. 481.

Urey, H.C.: 1968, Science 162, 1408.

Urey, H.C. and MacDonald, G.J.F.: 1971, in Physics and Astronomy of the Moon, 2nd Ed., (ed. by Z. Kopal), Academic Press, New York, p. 213.

Wasserburg, G.J. and Papanastassiou, D.A.: 1971, Earth Planetary Sci. Letters 13, 97.

Weertman, J.: 1970, Rev. Geophys. Space Phys. 8, 145.

Wood, J.A.: 1972, Icarus 16, 229.

Wood, J.A., Dickey, J.S., Jr., Marvin, J.B., and Powell, B.N.: 1970, Geochim. Cosmochim. Acta, Suppl. 1, 965.

Wood, J.A., Marvin, U.B., Reid, J.B., Jr., Taylor, G.J., Bower, J.F., Powell, B.N., and Dickey, J.S., Jr.: 1971, Smithsonian Astrophysical Observatory Special Report 333, 275 pp.

York, D., Kenyon, W.J., and Doyle, R.J.: 1972, Geochim. Cosmochim. Acta, Suppl. 3, 1613.

Table I

Parameters Used in All Thermal Models

Radius	1740 km
Density	3.34 g/cm^3
Thermal Conductivity	Curve "S" in Figure 5
Heat of fusion	400 joules/g
Specific heat	1.2 joules/g°C
Surface temperature	-20°C
K/U ratio	2000
Th/U ratio	4

Table II

A Summary of Parameters and Results for Thermal History Models

Fig. No.	Base Temp. °C	Accretion heating included?	Average U concentration ppb	Solid-state convection?	Melting at present?	Surface heat flux erg/cm^2 s
6	0	No	11-33	No	No	--
7	Initially molten		60	No	No	29
8	500	Yes	35	No	Yes	18
9	500	Yes	130	No	Yes	55
10	0	Yes	70	No	Yes	33
12	0	Yes	53 (initially inhomogeneous)	No	No	32
14	0	Yes	23	Yes	No	13

FIGURE CAPTIONS

FIGURE 1. A summary of igneous activity at the lunar surface from Rb-Sr and Ar^{39}-Ar^{40} ages of returned lunar samples. Samples from different missions are designated by "A" for Apollo (A-11 is Apollo 11) and L-16 for Luna-16. Special rocks are designated by numbers. Sources for this summary are given in full in the text.

FIGURE 2. Some estimates of present-day temperatures in the Moon using the lunar electrical conductivity profile. Included are the temperature curve of Sonett et al. (1971), an interpretation of the Sonett et al. (1971) conductivity distribution using the temperature-conductivity relation of an olivine with little or no Fe^{3+} (Duba et al., 1972), and the estimates by Dyal et al. (1972) of bounds on temperature from their most recent conductivity models.

FIGURE 3. a) Two proposed models for the increase in lunar radius r with time t during accretion (from Hanks and Anderson, 1969). τ is the total accretion time.

b) Initial temperature profiles for a Moon accreting with a time-dependent radius growth and with base temperatures of 0° and 500°C. Total accretion time is 100 years. The solidus of mare basalt (Ringwood and Essene, 1970) is assumed to be an upper limit for possible initial temperatures.

FIGURE 4. Potassium and uranium concentrations in selected meteorites and lunar and terrestrial rocks, updated from Hays (1972). Points for average chondrites, eucrites and howardites are from Mason (1971). Values for Apollo 15 and 16 rocks are from LSPET (1972) and LSPET (1973), respectively.

FIGURE 5. Thermal conductivity of selected materials. Sources of measured data (solid lines) are Cremers (1971) for Apollo 11 fines, sample density 1.64 g/cm^3; Horai et al. (1970) for Apollo 11 basalt; Murase and McBirney (1970) for synthetic Apollo 11 basalt; Schatz and Simmons (1972) for sintered, polycrystalline forsterite and for single-crystal olivine (Fo_{86} Fa_{14}) and enstatite. Theoretical (dashed) curves include those of MacDonald (1963b),

for two different values of the mean extinction coefficient or opacity ε, and one proposed by Schatz and Simmons (1972) for polycrystalline olivine of approximate composition $Fo_{90}\ Fa_{10}$. The Schatz and Simmons curve, labeled S above, was adopted in this paper.

FIGURE 6. Present-day temperature profiles in an initially-cold Moon (0°C at all depths) as a function of present-day concentration of uranium. The solidus of anhydrous mare basalt (Ringwood and Essene, 1970) is also shown.

FIGURE 7. A model of the evolution of the lunar temperature profile as a function of time for an initially molten Moon. See the text for other parameters. Time, in billions of years since lunar origin, is indicated by the number adjacent to each profile. On this and later figures, the Moon is partially or completely molten at those depths where the temperature profile lies along the solidus of mare basalt (Ringwood and Essene, 1970); the depth range for complete melting is delimited by the small arrows above the solidus.

FIGURE 8. Thermal evolution in a Moon accreted in 100 years at a base temperature of 500°C with average present-day uranium concentration equal to that of howardites. All symbols are described in the caption to Figure 7.

FIGURE 9. Thermal evolution in a Moon similar to that of Figure 8 except with average present-day uranium concentration equal to that of eucrites. All symbols are described in the caption to Figure 7.

FIGURE 10. Thermal evolution in a Moon accreted in 100 years at a base temperature of 0°C with average present-day uranium concentration chosen to match the Apollo 15 heat flow value (Langseth et al., 1972). Shown also are the Fe-FeS eutectic temperature (Brett and Bell, 1969) and the phase boundary (dotted line) between feldspathic and spinel pyroxenite in the model lunar mantle composition of Ringwood and Essene (1970). Other symbols are described in the caption to Figure 7.

FIGURE 11. The extent of melting in the thermal model of Figure 10. Heavy stippling denotes complete

fusion; lighter stippling indicates partial fusion.

FIGURE 12. Thermal evolution in a Moon derived from inhomogeneous accretion. The initial temperature profile follows from a presumed cold (0°C) accretion over a 1000 year time interval. Primary zoning of radioactivity is assumed (see text for details). Other parameters and symbols are explained in the caption to Figure 7.

FIGURE 13. The extent of melting as a function of time in the thermal model of Figure 12. Shading follows the notation of Figure 11.

FIGURE 14. The effect of convection by solid-state creep on the later stages of thermal evolution in the Moon (see text). From 0 to 2 b.y., this model follows a conventional thermal history route beginning with a 100-year accretion at 0°C.

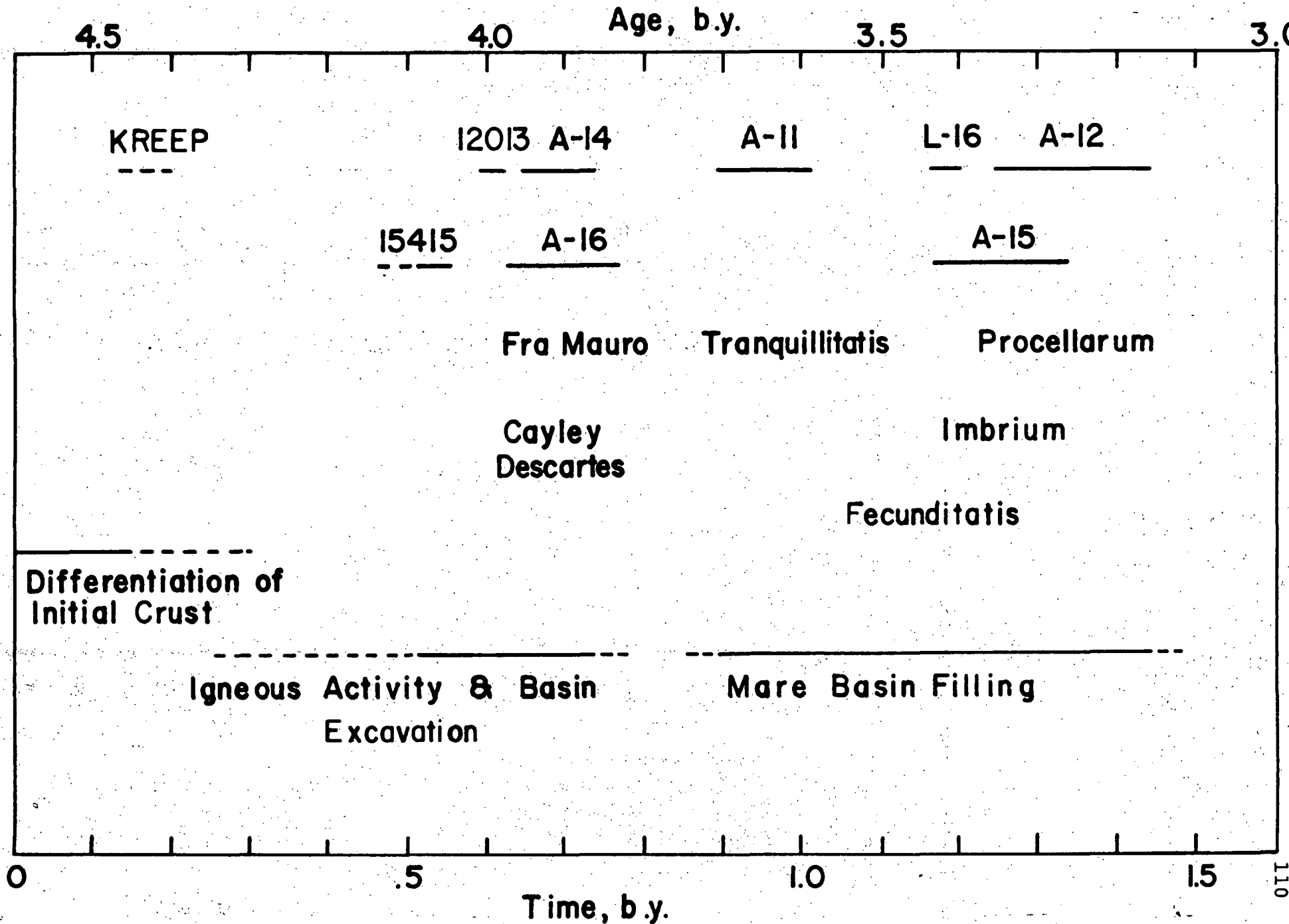
Age, b.y.
4.5
4.0
3.5
3.0
KREEP
12013
A-14
A-11
L-16
A-12
15415
A-16
A-15
Fra Mauro
Tranquillitatis
Procellarum
Cayley
Descartes
Imbrium
Fecunditatis
Differentiation of
Initial Crust
Igneous Activity & Basin
Excavation
Mare Basin Filling
0
.5
1.0
1.5
Time, b.y.

Figure 1

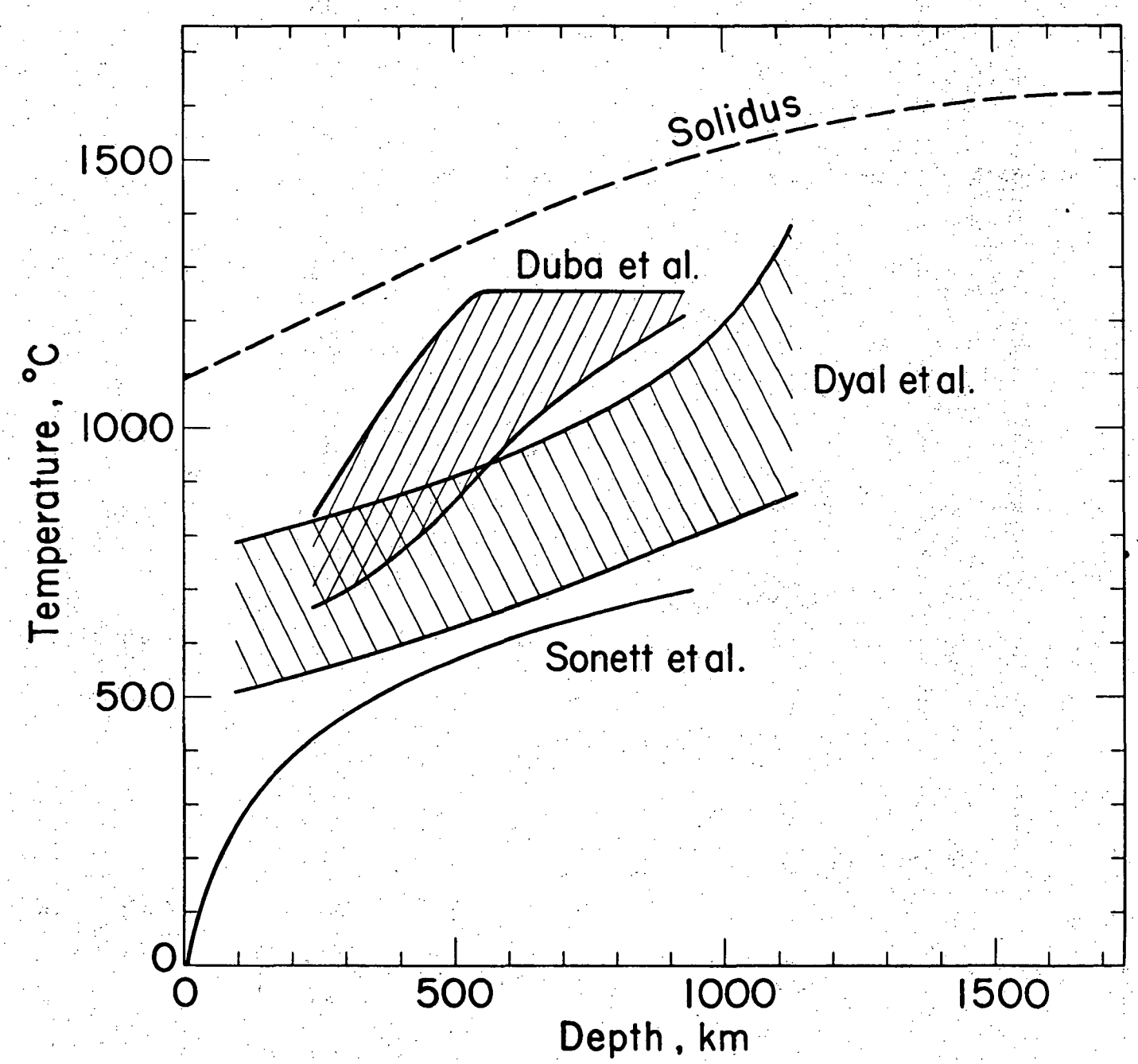
Solidus
Duba et al.
Dyal et al.
Sonett et al.
Temperature, °C
1500
1000
500
0
0
500
1000
1500
Depth, km

Figure 2

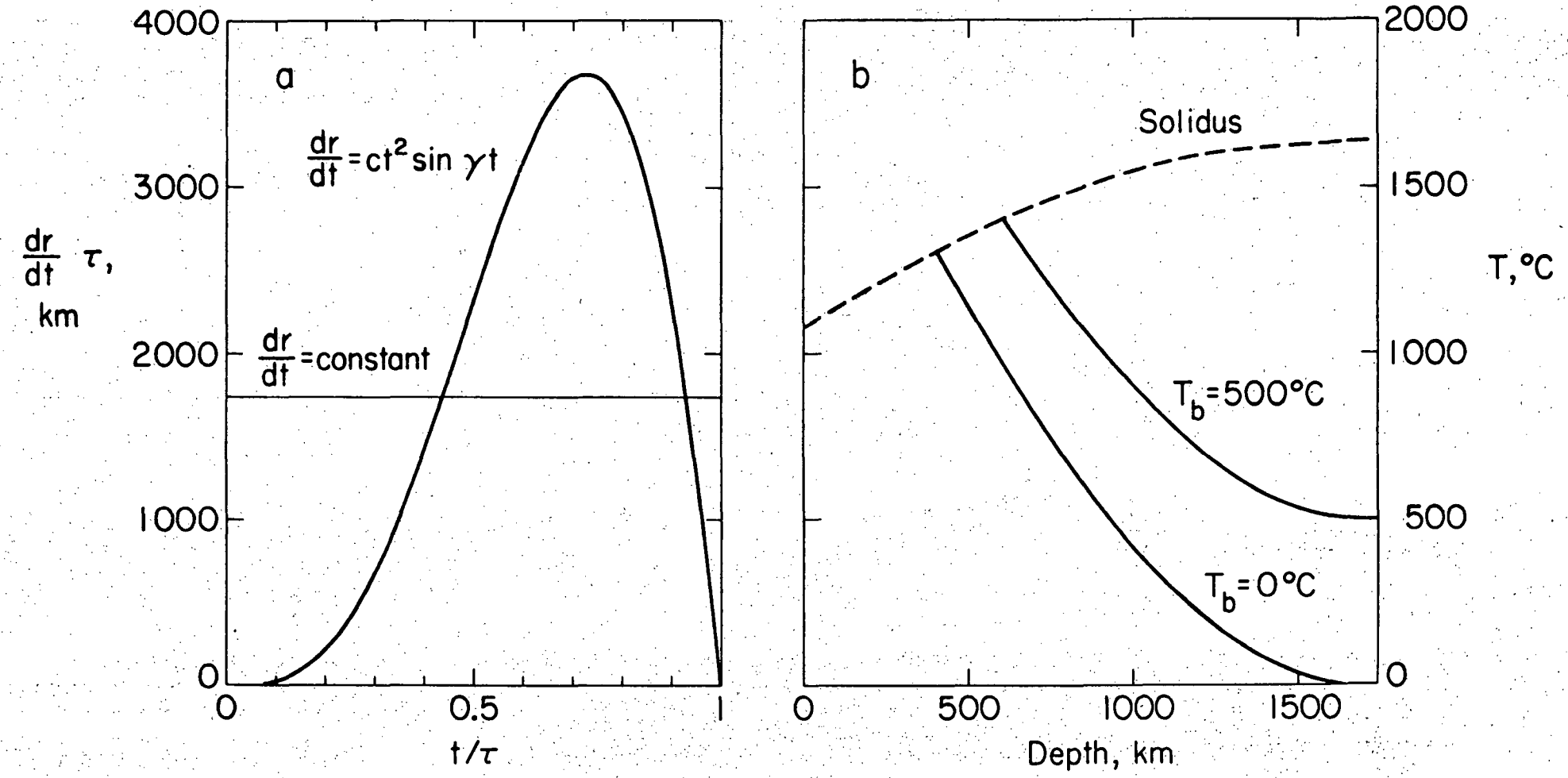
a
$\frac{dr}{dt} = ct^2 \sin \gamma t$
$\frac{dr}{dt}$ = constant
$\frac{dr}{dt}\ \tau$, km
4000
3000
2000
1000
0
0
0.5
1
t/τ
b
Solidus
T_b=500°C
T_b=0°C
2000
1500
1000
500
0
T, °C
0
500
1000
1500
Depth, km

Figure 3

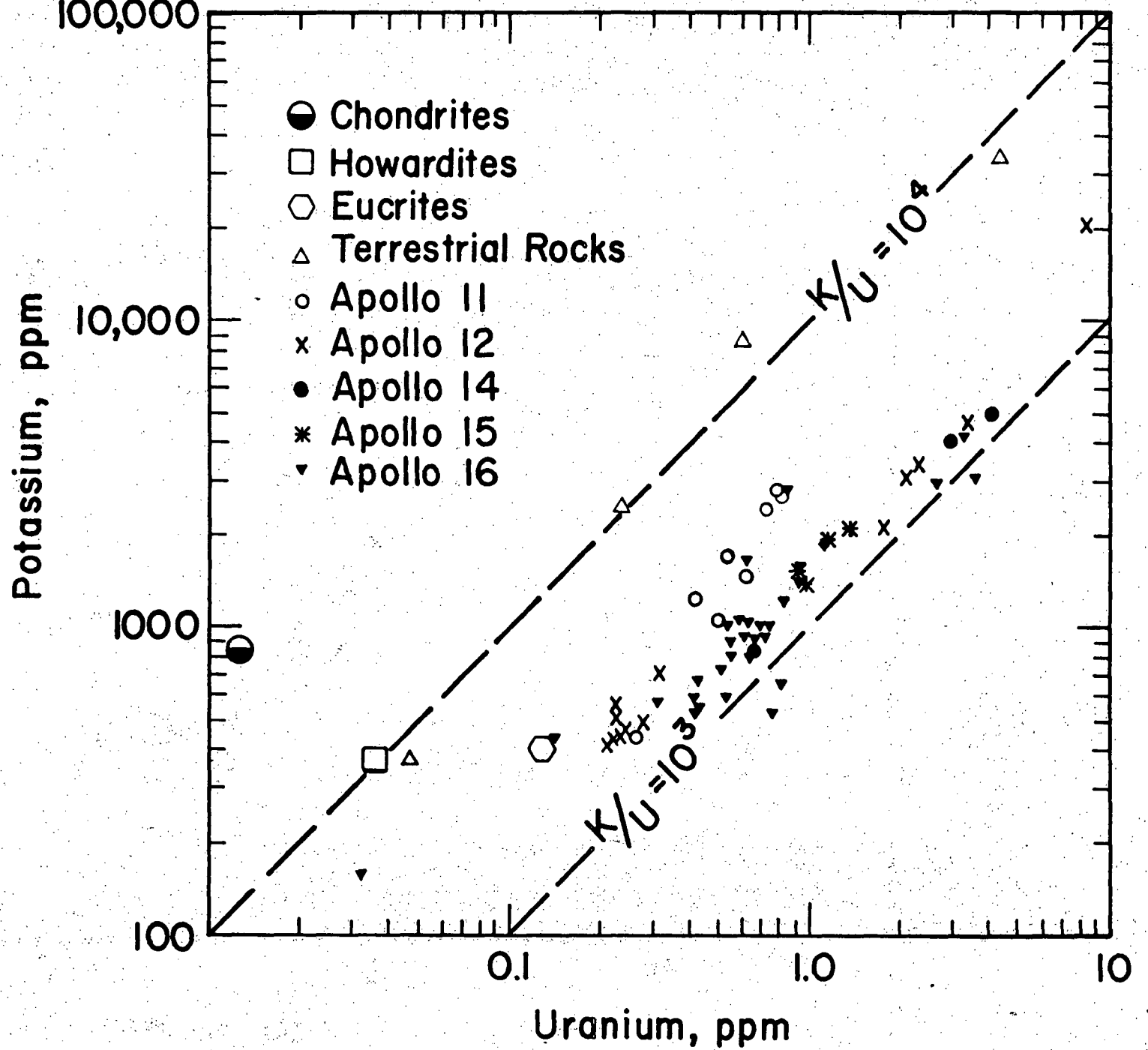
100,000
10,000
1000
100
Potassium, ppm
0.1
1.0
10
Uranium, ppm
Chondrites
Howardites
Eucrites
Terrestrial Rocks
Apollo 11
Apollo 12
Apollo 14
Apollo 15
Apollo 16
K/U = 10^4
K/U = 10^3

Figure 4

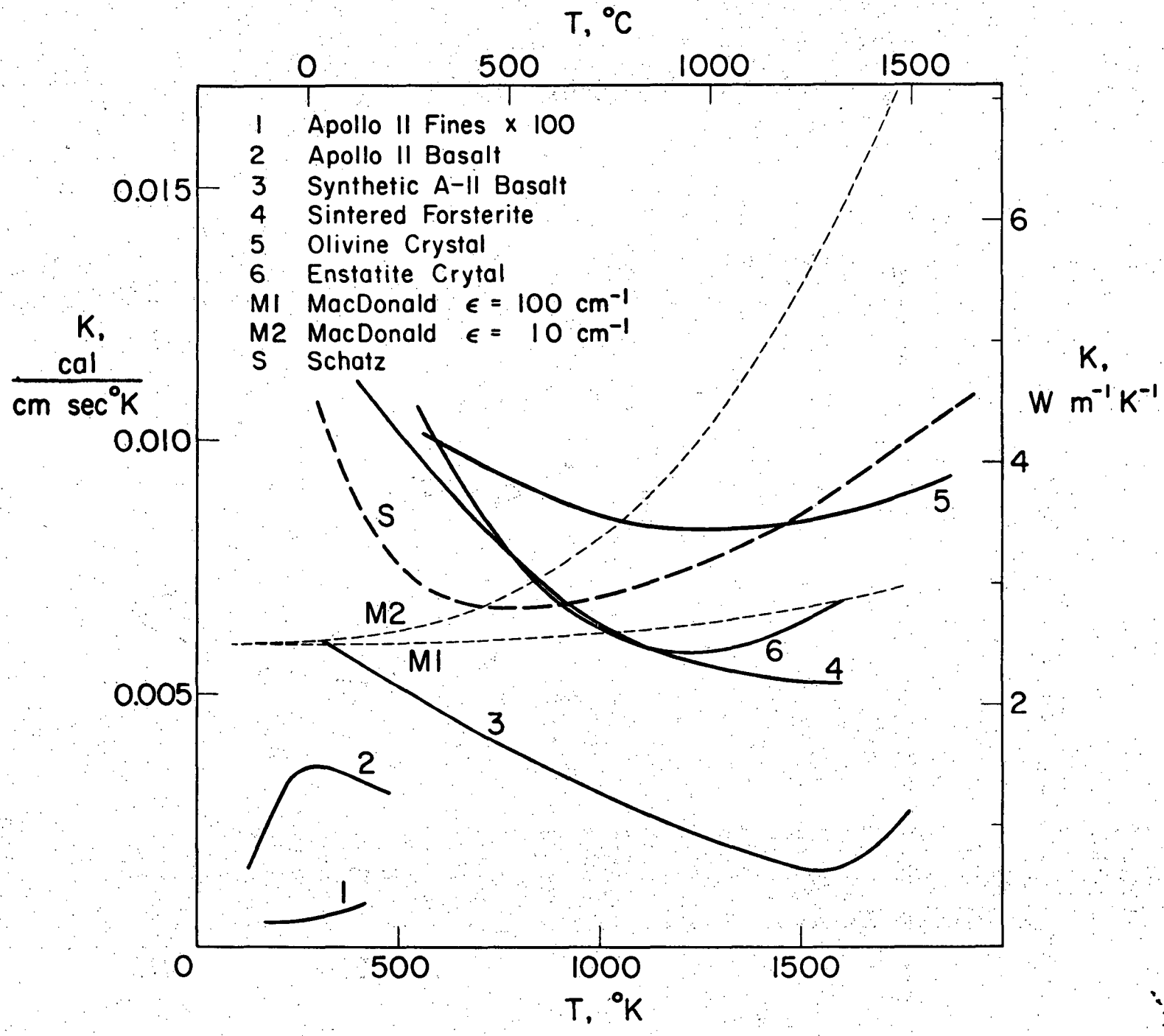
T, °C
0
500
1000
1500
1 Apollo II Fines x 100
2 Apollo II Basalt
3 Synthetic A-II Basalt
4 Sintered Forsterite
5 Olivine Crystal
6 Enstatite Crytal
M1 MacDonald ϵ = 100 cm⁻¹
M2 MacDonald ϵ = 10 cm⁻¹
S Schatz
K, cal / cm sec °K
0.015
0.010
0.005
K, W m⁻¹ K⁻¹
6
4
2
S
M2
M1
5
6
4
3
2
1
0
500
1000
1500
T, °K

Figure 5

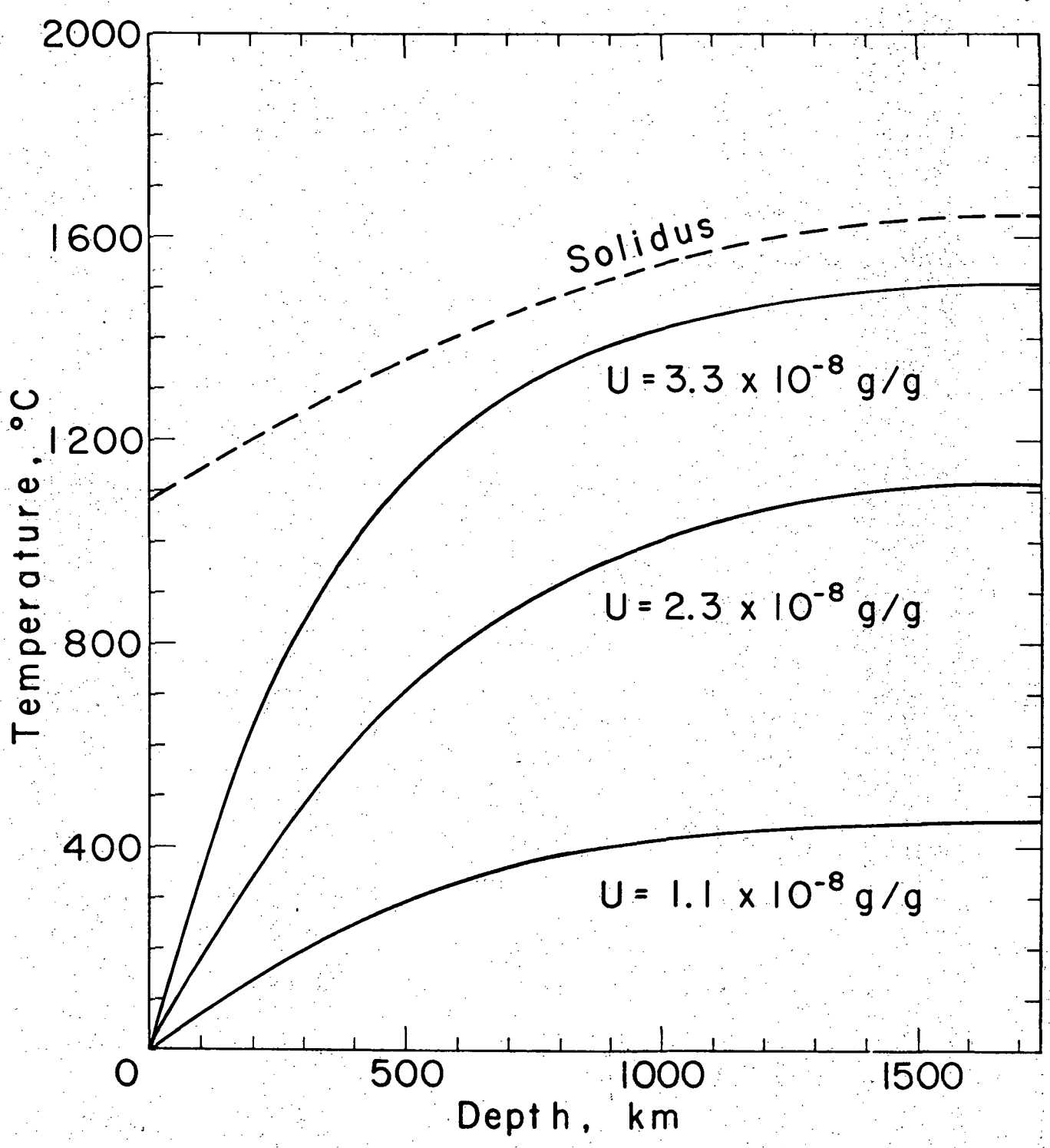
2000
1600
1200
800
400
0
500
1000
1500
Temperature, °C
Depth, km
Solidus
U = 3.3 x 10⁻⁸ g/g
U = 2.3 x 10⁻⁸ g/g
U = 1.1 x 10⁻⁸ g/g

Figure 6

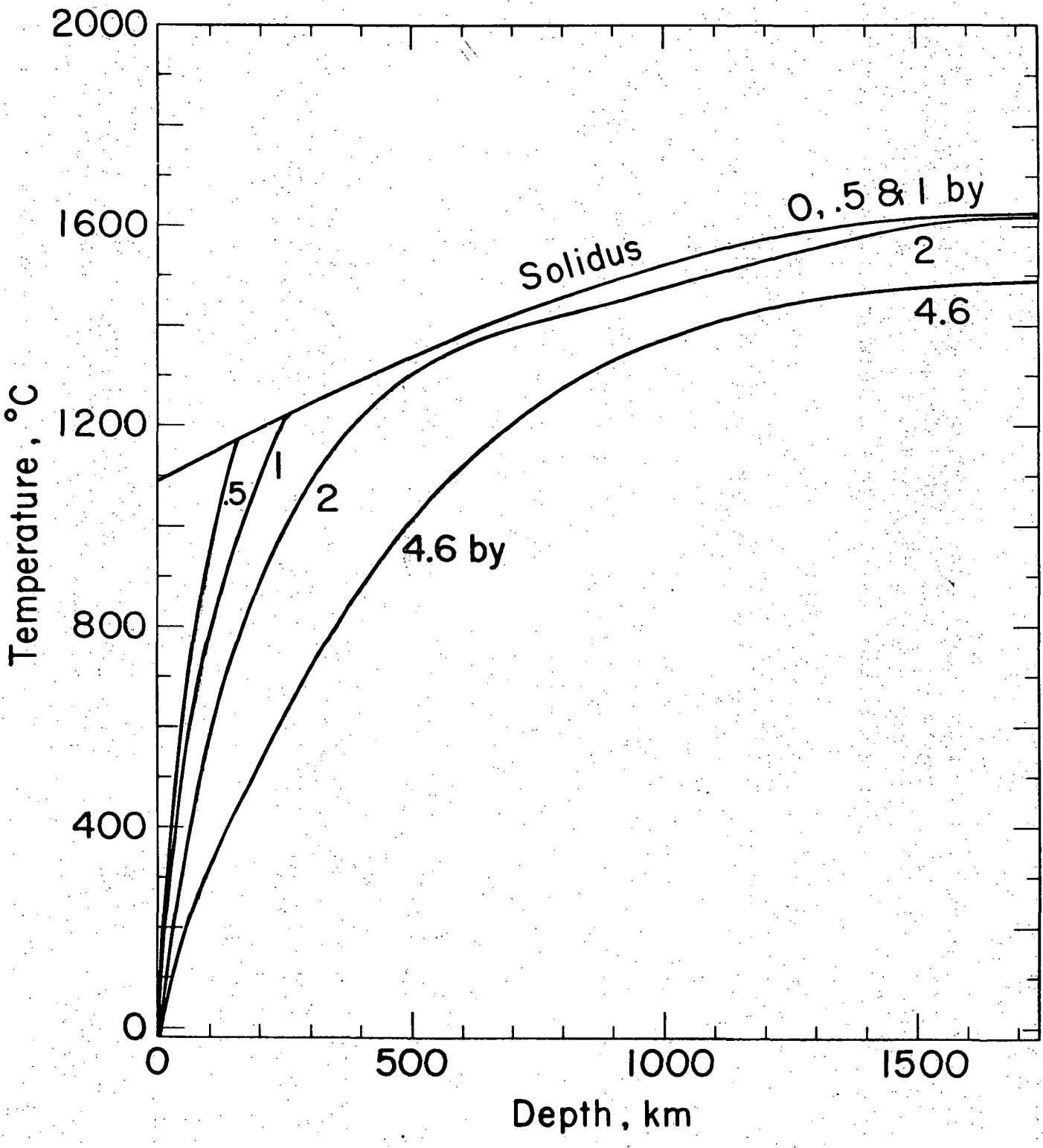
2000
1600
1200
800
400
0
Temperature, °C
0
500
1000
1500
Depth, km
Solidus
0, .5 & 1 by
2
4.6
.5
1
2
4.6 by

Figure 7

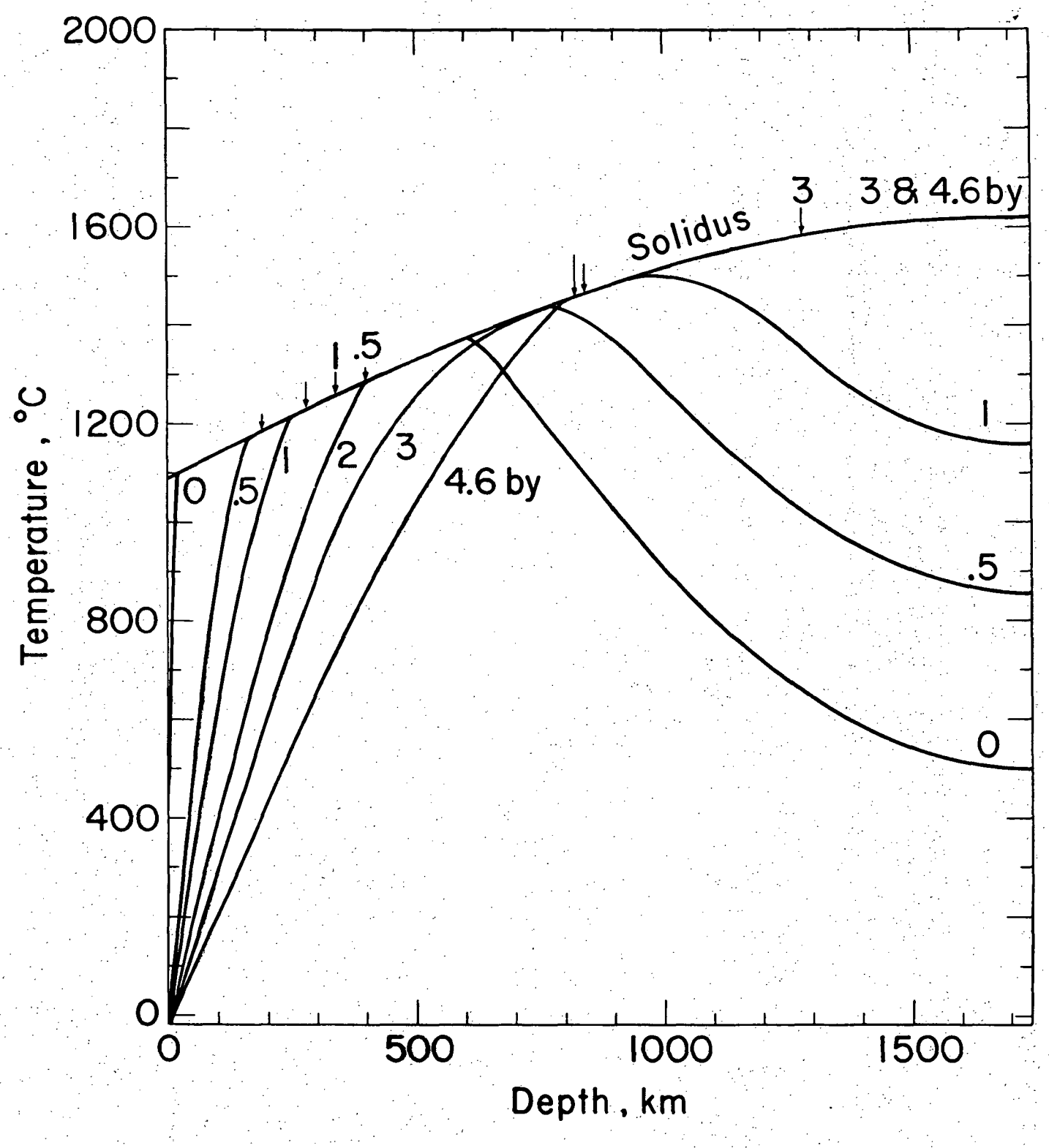
2000
1600
1200
800
400
0
Temperature, °C
0
500
1000
1500
Depth, km
Solidus
3
3 & 4.6by
1.5
1
2
3
4.6 by
0
.5
1
.5
0

Figure 8

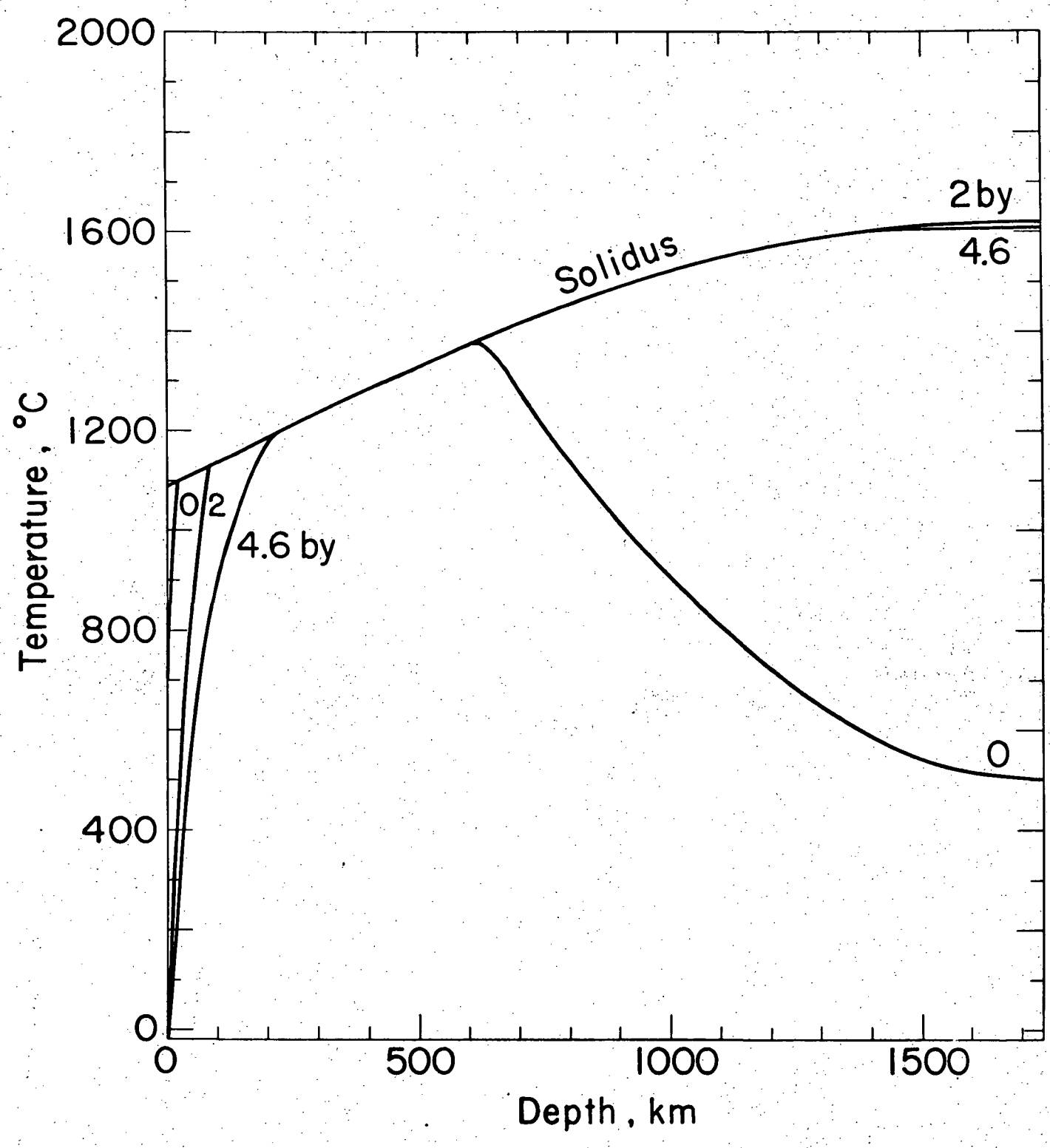
2000
1600
1200
800
400
0
Temperature, °C
0
500
1000
1500
Depth, km
Solidus
2by
4.6
0
2
4.6 by
0

Figure 9

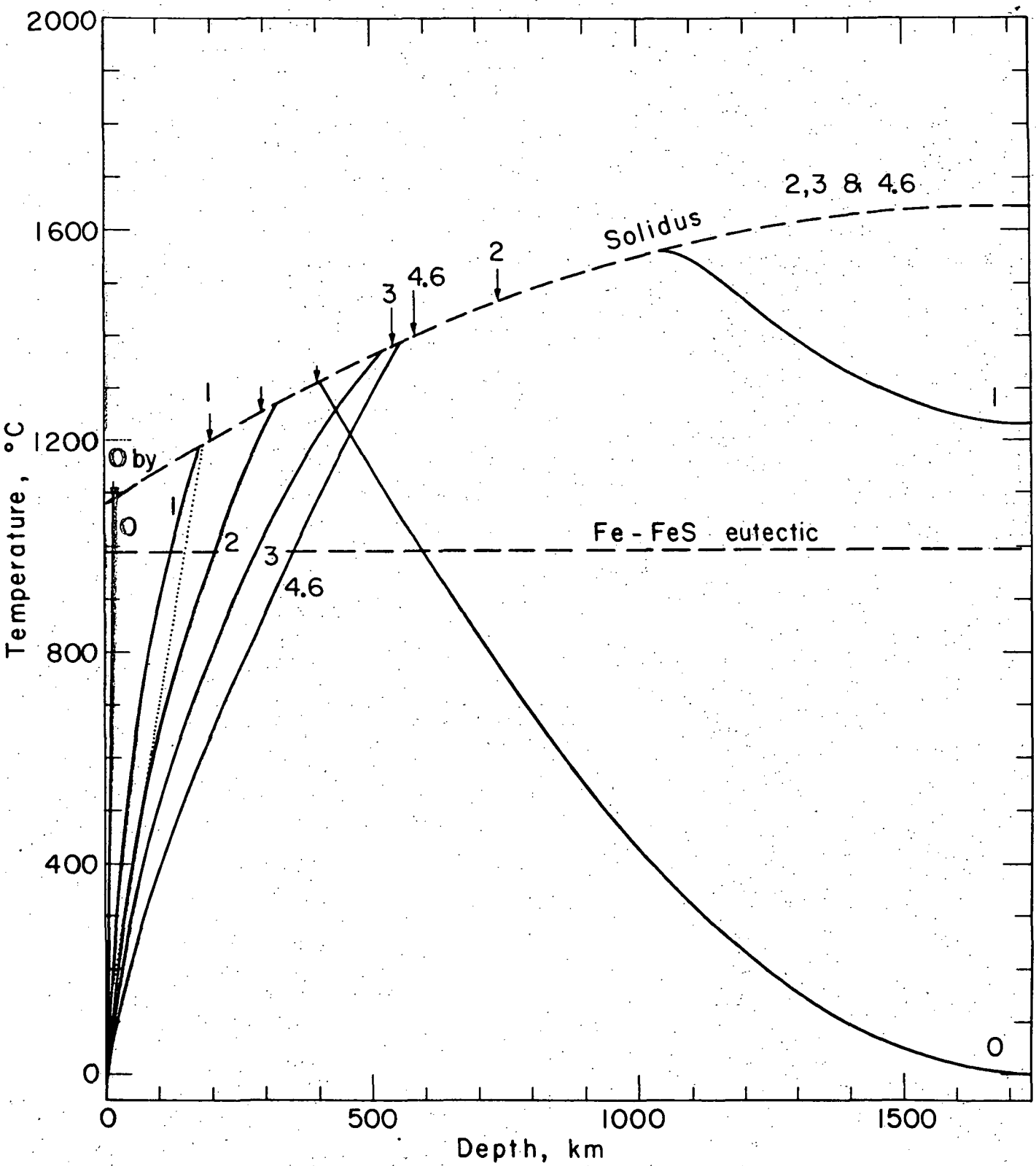
2000
1600
1200
800
400
0
Temperature, °C
0
500
1000
1500
Depth, km
2,3 & 4.6
Solidus
2
3
4.6
1
0 by
0
1
2
3
4.6
Fe - FeS eutectic
1
0

Figure 10

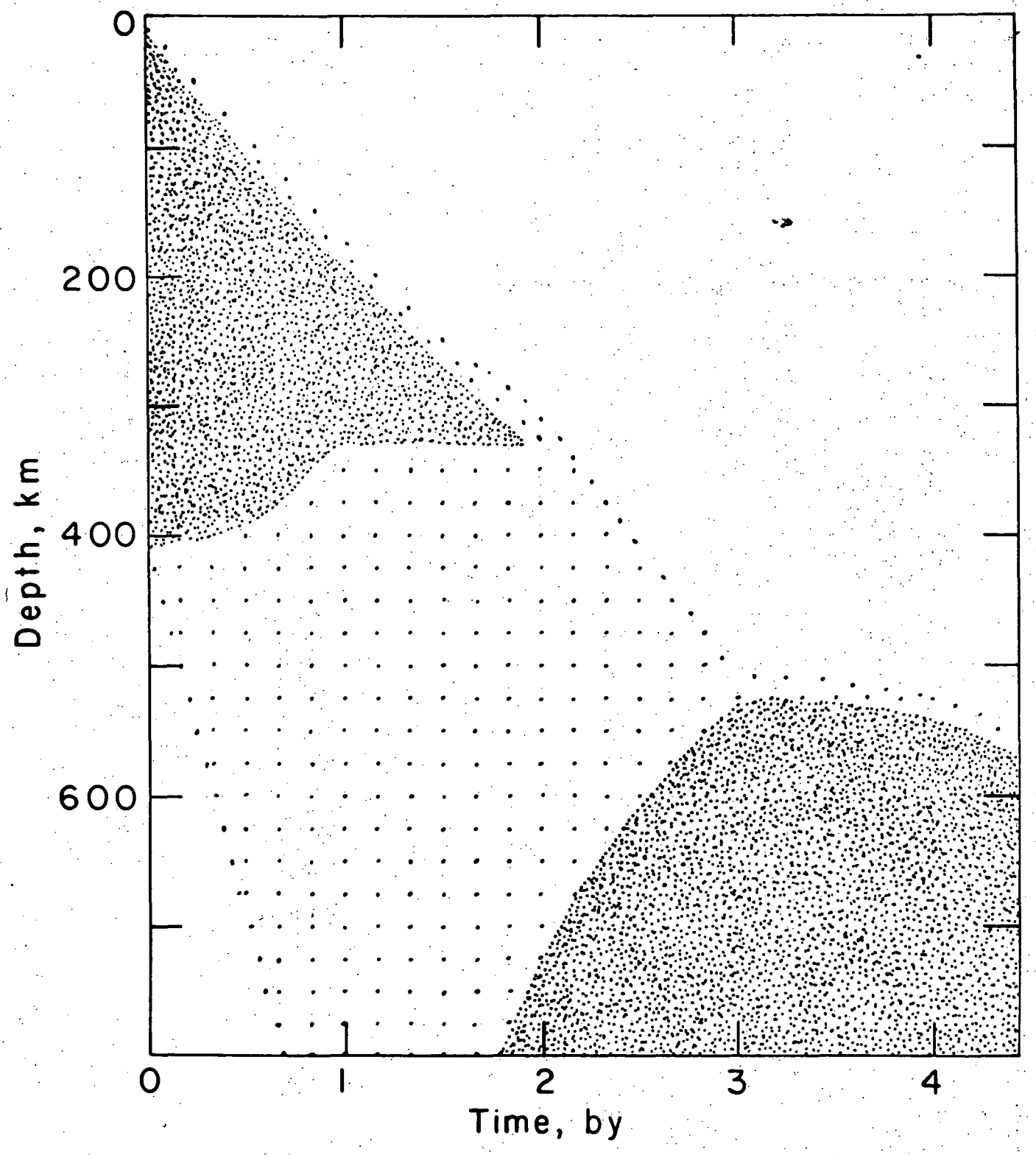

Figure 11

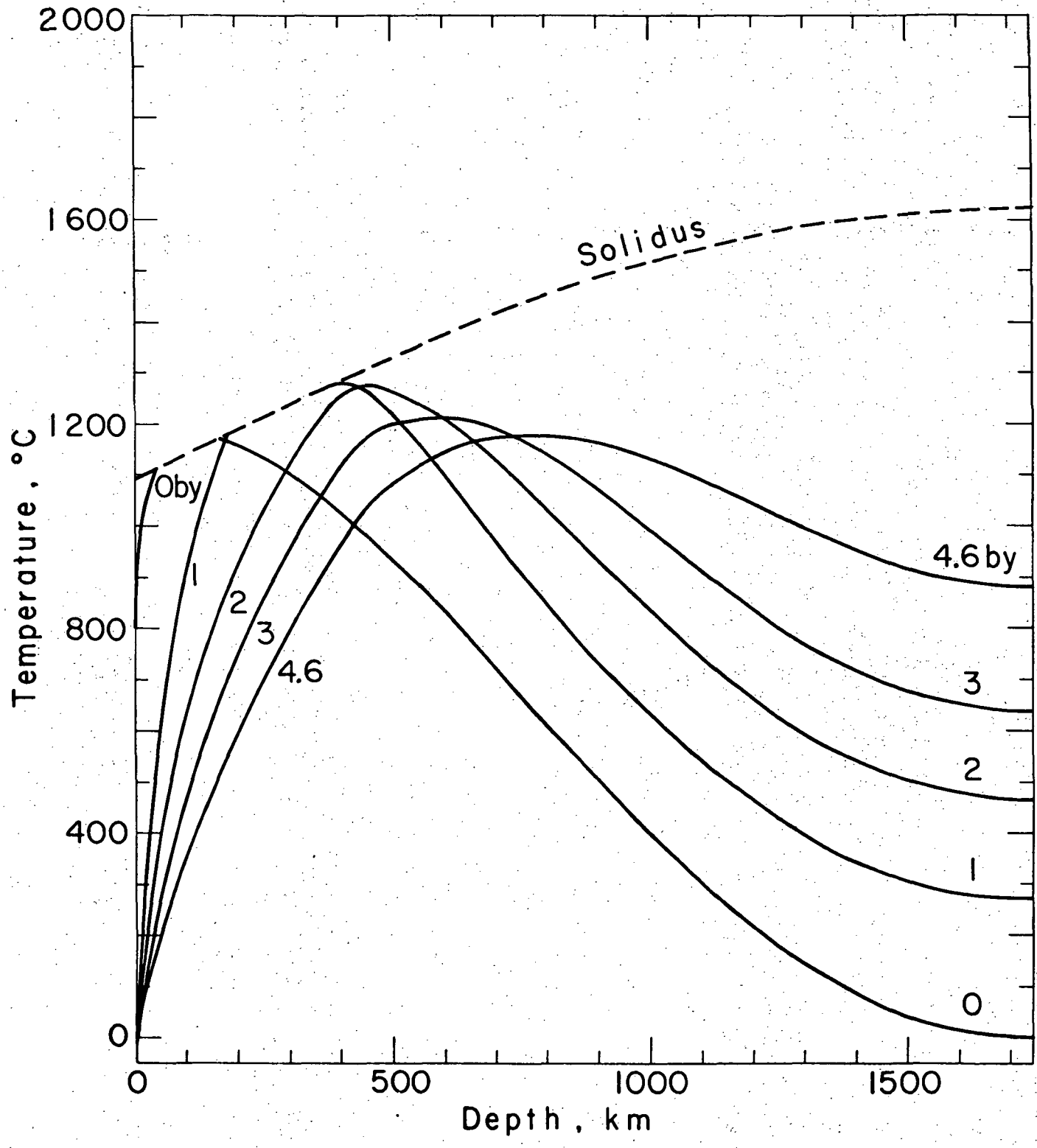
2000
1600
1200
800
400
0
Temperature, °C
0
500
1000
1500
Depth, km
Solidus
Oby
1
2
3
4.6
4.6by
3
2
1
0

Figure 12

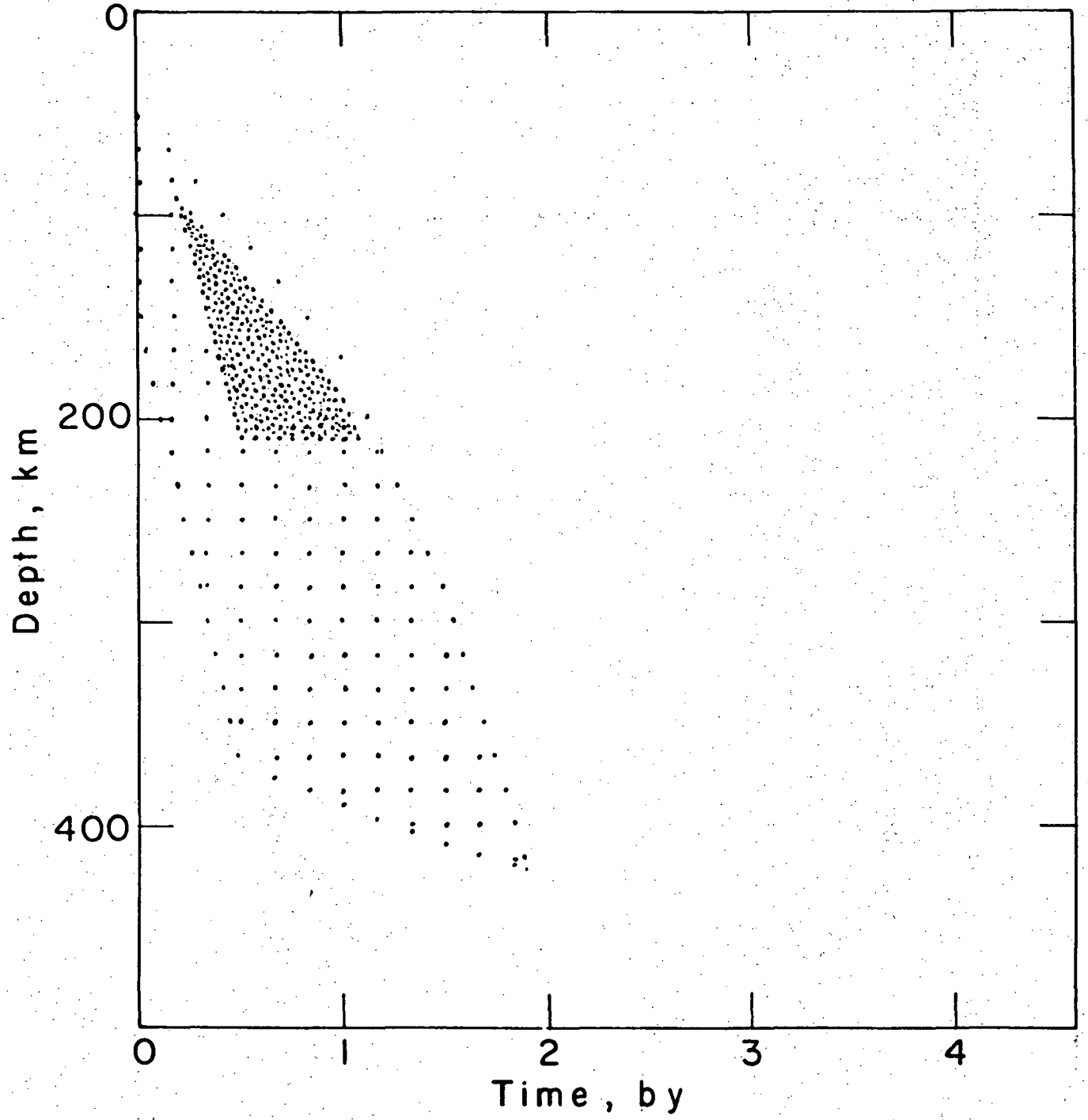

Figure 13

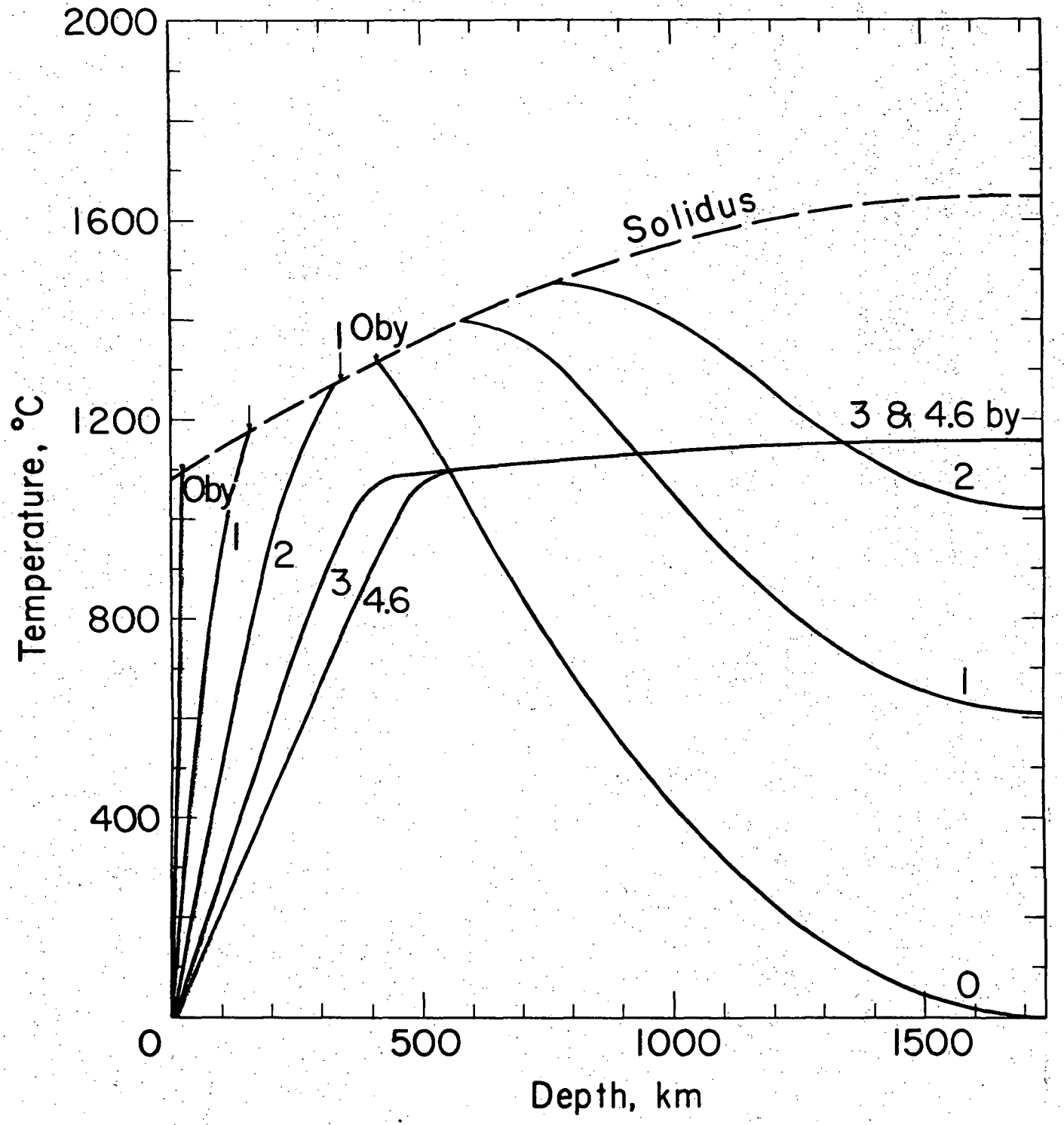
2000
1600
1200
800
400
0
500
1000
1500
Temperature, °C
Depth, km
Solidus
1 Oby
Oby
1
2
3
4.6
3 & 4.6 by
2
1
0

Figure 14

Physics of the Earth and Planetary Interiors, in press.

INTERNAL CONSTITUTION AND EVOLUTION OF THE MOON

Sean C. Solomon

M. Nafi Toksöz

Department of Earth and Planetary Sciences

Massachusetts Institute of Technology

Cambridge, Massachusetts 02139 U.S.A.

July, 1972

ABSTRACT

The composition, structure and evolution of the Moon's interior are narrowly constrained by a large assortment of physical and chemical data. Models of the thermal evolution of the Moon that fit the chronology of igneous activity on the lunar surface, the stress history of the lunar lithosphere implied by the presence of mascons, and the surface concentrations of radioactive elements, involve extensive differentiation early in lunar history. This differentiation may be the result of rapid accretion and large-scale melting or of primary chemical layering during accretion; differences in present-day temperatures for these two possibilities are significant only in the inner 1000 km of the Moon and may not be resolvable. If the Apollo 15 heat flow result is representative of the Moon, the average uranium concentration in the Moon is 50 to 80 ppb.

Density models for the Moon, including the effects of temperature and pressure, can be made to satisfy the mass and moment of inertia of the Moon and the presence of a low density crust inferred from seismic refraction studies only if the lunar mantle is chemically or mineralogically inhomogeneous. The upper mantle must exceed the density of the lower mantle at similar conditions by at least 5 percent. The average mantle density is that of a pyroxenite or olivine pyroxenite, though the density of the upper mantle may exceed 3.5 g/cm^3. The density of the lower mantle is less than that

of the combined crust and upper mantle at similar temperature and pressure, thus reinforcing arguments for early Moon-wide differentiation of both major and minor elements. The suggested density inversion is gravitationally unstable and implies stresses in the mantle 3 to 5 times those associated with the lunar gravitational field, a difficulty that can be explained or avoided by (i) adopting lower values for the moment of inertia and/or crustal thickness or (ii) by postulating that the strength of the lower mantle increases with depth or with time, both of which are possible for certain combinations of composition and thermal evolution.

A small iron-rich core in the Moon cannot be excluded by the Moon's mass and moment of inertia. If such a core were molten at the time lunar surface rocks acquired remanent magnetization, then thermal history models with initially cold interiors strongly depleted in radioactive heat sources as a primary accretional feature must be excluded. Further, the presence of K^{40} in an Fe-FeS core could significantly alter the thermal evolution and estimated present-day temperatures of the deep lunar interior.

1. INTRODUCTION

Our knowledge of the chemical and physical properties of the Moon is both extensive and detailed. Samples analyzed from 11 lunar landing sites to date and information from earth-based and lunar-orbital geochimical, optical and infrared experiments are being combined to give a broad understanding of the present state of a large fraction of the Moon's surface area. The properties of the bulk of the Moon and its interior are less well-defined, but by no means obscure. By necessity, study of the lunar interior must be largely indirect and the conclusions reached can rarely be definitive. Nonetheless, the quantity of data that can now be brought to bear on the particulars of the deep lunar interior is large. In this paper we shall apply these data to the questions of internal lunar structure, of compositional models for the subsurface lunar material, and of possible evolutionary routes by which the Moon might have reached its present state.

For several reasons, the Moon is a particularly suitable, and perhaps unique, body for investigating present-day constitution and models of evolution, both of which bear on the early history of planet-sized objects in the solar system. First, the surface to volume ratio for the Moon is large

relative to that for other terrestrial planets, so that observations made at or near the lunar surface have implications for a relatively large segment of the moon. The lunar crust, for instance, constitutes approximately 10 percent of the mass of the Moon; the corresponding figure for the Earth is about half a percent. Second, the record of the early history of the Moon's surface, particularly between 3 and 4 billion years ago, is well preserved. Finally, because of the Moon's size, the pressures and temperatures of the lunar interior are accessible in the laboratory, and thus measurements of important physical parameters at the conditions throughout the moon can be or have been made.

We begin with a critical summary of the available constraints on lunar constitution and evolution. The foremost constraint on the composition of the Moon comes from the chemistry of the lunar surface. Downward extrapolation can be made on the basis of the seismic velocity structure, models of petrogenesis, and considerations of the density of the lunar interior. The thermal evolution of the Moon, and the related history of melting and differentiation, must be consistent with the observed episodes of igneous activity at the lunar surface, with estimates of the stress history of

the lunar lithosphere, and with the present-day temperature profile inferred from heat flow and electrical conductivity measurements. An interesting but unconfirmed additional constraint would be the presence of an ancient lunar magnetic field of internal origin.

We next reconsider in detail possible models for the thermal evolution in the Moon. The single heat-flow measurement, if representative of the Moon as a whole, requires the average Moon to be more radioactive than presumed in most earlier models. Early upwards segregation of the heat sources in the Moon, either during a melting episode which followed a rapid accretion or as a primary accretional feature, is still required. Differences in present-day temperature or in strength of the deep lunar interior are perhaps the only means by which thermal history calculations can resolve whether the high values of radioactivity at the lunar surface are due to differentiation in an originally homogeneous moon or are partly the result of an inhomogeneous accretion process.

Using several estimates of present day temperature and the confirmed thickness of a low-density crust, we examine density models for the lunar interior that match the Moon's mean density and moment of inertia. Models with chemically uniform mantles, though marginally permitted by the present

uncertainty in the moment of inertia of the Moon, are not favored. To fit the moment of inertia, the upper mantle must be denser than the lower mantle. The magnitude of the required density reversal is probably unstable to solid-state creep, though there is less problem explaining the stress differences if the upper mantle is richer in Ca and Al than the lower or if the lower mantle was relatively depleted in radioactive elements at the time of a cold accretion. If the moment of inertia value holds up, then the lower mantle cannot have the same major element chemistry as the bulk Moon.

Finally, we briefly consider a few of the consequences of an iron-rich core in the Moon. Even if the lunar mantle is uniform, a small core is permitted by the moment of inertia. If a convecting core were an early feature in the Moon, several further constraints on the initial temperatures and heat sources in the Moon would be imposed.

2. CONSTRAINTS ON LUNAR STRUCTURE AND EVOLUTION

2.1 Petrology, Chemistry

The most direct evidence for the internal composition of the Moon comes from the chemistry, mineralogy, and inferred petrogenesis of the material returned from the lunar surface. Analysis of lunar rock and soil samples, together with the results of the orbital x-ray and gamma-ray spectrometer experiments, have shown the lunar surface to be comprised principally of three rock types: (1) iron-rich mare basalts, (2) nonmare basalts, also labeled KREEP and norite, rich in aluminum, radioactive elements and refractory trace elements, and (3) plagioclase-rich rocks (WOOD et al., 1971; HUBBARD and GAST, 1971; LSAPT, 1972).

Mare basalt samples have been returned from four different near-side mare sites to date. Experimental high-pressure, high-temperature studies (RINGWOOD and ESSENE, 1970; GREEN et al., 1971) indicate that mare basalts probably formed by variable amounts of partial melting at depths between 100 km and 500 km in a lunar mantle composed of pyroxene and possibly olivine. The sugesstion (GAST et al., 1970; HASKIN et al., 1970; PHILPOTTS and SCHNETZLER, 1970), based on the abundances of rare-earth

elements and on the negative europium anomaly in particular, that mare basalts were derived from a source rock rich in plagioclase is in apparent conflict with the high-pressure melting experiments mentioned above. Alternative explanations, not involving plagioclase in the source rock, for the europium anomaly have been advanced by GOLES et al. (1970) and RINGWOOD and ESSENE (1970), and experimentally supported by GRAHAM and RINGWOOD (1971).

Several modes of origin for nonmare basalts have been proposed, including a small degree of partial melting of a shallow, plagioclase-rich source (HUBBARD and GAST, 1971), more extensive melting of a plagioclase-pyroxine-olivine crust followed by crystal fractionation (WALKER et al., 1972), and impact melting of the upper several kilometers of a plagioclase-rich crust (GREEN et al., 1972). GREEN et al. (1972) have argued on chemical and mechanical grounds that the first two explanations are improbable. A similar thread in each of the above hypotheses is the notion of abundant plagioclase in the near-surface regions of the Moon at the time that nonmare basalts were formed. Nonmare or KREEP basalts may constitute a relatively minor, though important, fraction of lunar surface material. The gamma-ray spectrometer results (ARNOLD et al., 1972) have so far indicated only one major area on the Moon, the Oceanus

Procellarum-Mare Imbrium region, where the surface radioactivity is sufficiently high to suggest a sizeable KREEP component. About 20 percent KREEP and 80 percent mare basalt would match the data for that region (LSAPT, 1972).

Several authors (WOOD et al., 1970; ENGELHARDT et al., 1970; KING et al., 1970; SHORT, 1970; SMITH et al., 1970a) hypothesized, on the basis of plagioclase or plagioclase-rich fragments in the lunar soil, that plagioclase, predominantly anorthite, is an important constituent of the lunar highlands. This suggestion was confirmed by the Apollo 15 and 16 x-ray fluorescence experiment (ADLER et al., 1972a, b) which demonstrated significantly greater amounts of aluminum, most likely in feldspar, in the highlands than in mare material. Several of the highland regions exhibited Al/Si ratios appropriate to anorthositic gabbros and gabbroic anorthosites. The anorthosites and plagioclase-rich rocks owe their origin to complete or nearly complete melting of the outer regions of the Moon (WOOD et al., 1970, 1971; HUBBARD et al., 1971).

2.2 Seismic Velocity

The lunar seismic velocity distribution, obtained

from the travel times and amplitudes of seismic waves from artificial impacts on the Moon's surface, can be used both to delineate chemical layering and to infer roughly the composition in the outer 100 km of the Moon. The compressional velocity profile in the Fra Mauro region of the Oceanus Procellarum, constructed from data through the Apollo 16 mission (TOKSÖZ et al., 1972a,b), is shown in fig. 1. The very rapid rise of velocity with depth in the uppermost 10 km can reasonably be ascribed to a self-compaction effect, so that the velocity structure suggests three petrologically distinct layers: (i) a 25-km thick upper crust, with compressional velocity (at low porosity) 5 to 6 km/sec; (ii) a 40-km thick lower crust, with velocity 7 km/sec; and (iii) a mantle, with apparent velocity 8 km/sec. A thin (less than 20 km, say) high-velocity (9 km/sec) layer may also be present between the lower crust and normal mantle. The shear wave data support the proposed layered structure (TOKSÖZ et al., 1972b).

Comparison of the velocity profile with laboratory measurements of compressional velocity in lunar and terrestrial rocks at appropriate pressures allows some estimate of the most likely rock types for each layer (TOKSÖZ et al., 1972a,b). The velocities in the upper crust fall within the range of the velocities of mare and nonmare basalts (see

fig. 1), and thus the upper crust in the Procellarum region is probably similar in composition to basaltic rocks found at the surface. The lower crust has a velocity similar to those measured in terrestrial gabbros and anorthosites; the likelihood of abundant anorthositic gabbros in the lunar highlands and the spectral evidence for highland material underlying some mare craters (MCCORD et al., 1972) make such a material a strong candidate for the primary constituent of this layer. The high velocity in the layer immediately below the lower crust, if indeed such a layer is a widespread feature on the Moon, is greater than that of any common basic or ultrabasic rock on earth. A high-pressure form of the aluminum rich lower crust has been mentioned as a candidate material with the requisite velocity (ANDERSON and KOVACH, 1972; TOKSÖZ et al., 1972a,b). That the average velocity of the Moon's mantle, between about 70 and 130 km, is about 8 km/sec permits a wide range of rock types, including dunites, pyroxenites and exlogites, as candidates for the material of the bulk of the lunar mantle.

2.3 Mass, Moment of Inertia

Perhaps the only firm constraint on the constitution of the deep interior of the Moon is that of the limitations

on the lunar density distribution imposed by the Moon's total mass and moment of inertia. We discuss further below the importance of these two quantities and the application of physically reasonable density models to the question of lunar internal structure.

Following KAULA (1971), we shall adopt the values $GM = 4902.7 \pm .1\ km^3/sec^2$ for the product of the gravitational constant and the Moon's mass, and $R = 1737.5 \pm .6$ km for the mean lunar radius. This gives a mean density of $3.344 \pm .004\ g/cm^3$.

The precise value of the moment of inertia of the Moon about its axis of rotation is more controversial, though it is exceedingly important in limiting possible density models (SOLOMON and TOKSÖZ, 1968; RINGWOOD and ESSENE, 1970; UREY and MACDONALD, 1971). We shall use KAULA'S (1969) value of $C/MR^2 = .402 \pm .002$, which is based on the second degree zonal and sectorial harmonic coefficients in the lunar gravitational-field solution of MICHAEL et al., (1970). A more recent and somewhat more complete analysis by MICHAEL and BLACKSHEAR (1972) gave a nearly identical value. It should be noted that the JPL group (LORELL, 1970; LIU and LAING, 1971), using a different analysis technique, consistently reports values for C/MR^2 significantly less

than .400. We conclude that Kaula's stated uncertainty in C/MR^2 may be a bit low. A more accurate and precise value must await better far-side and high-latitude tracking data.

2.4 Electrical Conductivity and Temperature

Several techniques have recently been used for deducing the electrical conductivity structure and related properties of the lunar interior, including analysis of the Moon's response to transient magnetic field events from simultaneous magnetometer measurements on the anti-solar surface and in the free-streaming solar wind (DYAL and PARKIN, 1971; DYAL et al., 1972b), and analysis of the frequency-dependent transfer function of sunlit lunar surface to the free-stream magnetic field (SONETT et al., 1971). The inferred electrical conductivity profiles were converted to equivalent temperatures (ENGLAND et al., 1968) to show that temperatures in the outer 700 to 800 km of the Moon must be less than 1000°C (SONETT et al., 1971; DYAL and PARKIN, 1971). The more recent inversion of DYAL et al. (1972b) allows, in addition, temperatures in excess of 1000°C by as much as several hundred degrees at depths greater than 800 km. The temperature

curve of Sonett et al. has attracted particular attention. Conventional thermal history calculations have shown that models which realistically account for lunar igneous activity and probable chemical and physical parameters yield present-day temperatures significantly higher than the Sonett et al. or Dyal-Parkin values (HAYS, 1972; TOKSÖZ et al., 1972c; REYNOLDS et al., 1972), unless very efficient heat transfer by solid-state convection is invoked (TOZER, 1972).

There are several difficulties with the temperature estimates from electrical conductivity, however. REISZ et al. (1972) have argued that neglect of the boundary condition assymetry imposed by solar wind flow past the Moon may affect the conductivity models of Dyal and Parkin and particularly of Sonett and others. SILL (1972) has pointed out that at the highest frequencies of the data of SONETT et al. (1971), their assumption of uniform source field breaks down. A further complication of the sunlit surface magnetometer analysis not considered by Sonett and others is the compression of a remanent field, largely unknown, by the solar wind (SILL, 1972; DYAL et al., 1972). At least as serious an objection to these temperature estimates is the observation by HOUSLEY and MORIN (1972) and

DUBA et al. (1972) that the conductivity of the ENGLAND et al. (1968) olivine is controlled by ferric ions not likely to be important in the reduced environment of the Moon. Recalculation of temperature in the Moon from the Sonett et al. (1971) conductivity profile, using recent data for a ferric-ion-poor terrestrial olivine, gives temperatures in excess of 1000°C below 350 to 600 km (DUBA et al., 1972).

2.5 Other indicators of Temperature

There are several other observations that bear less quantitatively on the question of the temperature of the lunar interior. The foremost of these is the measured value of heat flow, 33 ± 5 erg/cm^{2}sec, at the Apollo 15 landing site (LANGSETH et al., 1972). Whether this surprisingly high value is a good indicator of the mean heat flow at the lunar surface is an important unanswered question. The high surface radioactivity in the Imbrium-Procellarum region (ADLER et al., 1972) suggests that the average lunar heat flow is probably somewhat lower.

That at least the outer portions of the Moon are relatively cool at present is implied by the low seismicity

of the Moon (LATHAM et al., 1971) and the absence of significant tectonic activity. The persistence for some 3 billion years of the gravity anomalies associated with mascons demands that a cool lithosphere several hundred kilometers thick has been a permanent feature on the Moon since mare formation (UREY, 1968). The location of moonquake activity at 800 km depth (LATHAM et al., 1971) and the high-frequency seismic waves observed on the lunar surface from those events indicate that the Moon can sustain shear stresses at considerable depth and that little or no partial melting is to be expected in the Moon's upper 800 km (TOKSÖZ et al., 1972a).

2.6 Lunar Chronology

Age-dating of lunar samples, particularly dating using Rb-Sr and Ar^{40}-Ar^{39} techniques (PAPANASTASSIOU et al., 1970; PAPANASTASSIOU and WASSERBURG, 1970, 1971a,b, 1972; WASSERBURG and PAPANASTASSIOU, 1971; LUNATIC ASYLUM, 1970; TURNER, 1970, 1970, 1972; TURNER et al., 1971; HUSAIN et al., 1972; and others), has provided a well-documented outline of lunar igneous activity. The time sequence of activity places strong constraints on the Moon's early history and, to a lesser extent, on its later evolution (PAPANASTASSIOU

and WASSERBURG, 1971a).

An approximate outline of events occurring on the lunar surface, taken from the works cited above, is given in fig. 2. The Rb-Sr fractionation requires a major episode of melting and differentiation very near the time of lunar formation (PAPANASTASSIOU and WASSERBURG, 1971a). This is a necessary feature of lunar evolution even if some of the chemical inhomogeneities in the Moon are the result of primary accretional layering (WASSERBURG and PAPANASTASSIOU, 1971). Much of the lunar crust may date from this time, although intense bombardment, remelting and brecciation may have altered most or all of the original rocks of the lunar crust. The record of activity between 4.5 and 3.7 billion years (b.y.) ago is sketchy and confusing, but some form of igneous activity in rocks 15415 at 4.1 b.y., 12013 at 4.0 b.y., and Apollo 14 rocks at 3.9 b.y. is well established. Certainly the major mare basins must have been created at some stage in this time interval; the relative ages of the mare basin excavations have been reasonably well resolved (e.g. MUTCH, 1970), but the absolute ages are controversial. The filling of the maria obviously postdated the formation of the mare basins. To date, the well-determined ages of mare basalts span a relatively narrow time interval between 3.2 and 3.7 b.y. ago (WASSERBURG and PAPANASTASSIOU, 1971).

The gravity anomalies attributed to mascons probably originated during this period. The failure to discover lunar igneous rocks younger than about 3.2 b.y. ago is an important constraint on the Moon's thermal history (PAPANASTASSIOU and WASSERBURG, 1971a). If melting occurred since that time, it must have been very localized in extent or confined to depths in excess of several hundred kilometers.

2.7 Magnetism of Lunar Rocks

The lunar crust has a relatively large but extremely variable magnetization. This has been verified by steady magnetic fields measured on the lunar surface (DYAL et al., 1970; 1972b) and by magnetic anomalies observed by the Apollo 15 orbital magnetometer (COLEMAN et al., 1972). Further, many returned lunar samples were found to display a fairly stable remanent magnetization (STRANGWAY et al., 1970; NAGATA et al., 1970; HELSLEY, 1970; RUNCORN et al., 1970; and others). On the basis of these observations, which appear to require 1000-γ fields on the lunar surface during the emplacement of rocks spanning a time interval of almost 1 b.y., several workers (RUNCORN et al., 1970; PEARCE et al., 1971, and others) have suggested the fields are internal in origin and thus indicate a molten conducting core between

3.2 and 4.0 b.y. ago. The debate over this conclusion has been heated, and many other explanations of the magnetization, including fields associated with the earth, with the solar wind, or with shock or thermal effects, have been offered. While the matter is not yet settled, the existence of a small iron-rich core in the Moon would have implications of great importance for models of lunar evolution. Some of these implications are explored later in this paper.

3. LUNAR THERMAL EVOLUTION

The thermal history of the Moon has been a popular subject, particularly since the Apollo missions (HAYS, 1972; WOOD, 1972; REYNOLDS et al., 1972; TOKSÖZ et al., 1972c; McCONNELL and GAST, 1972; TOZER, 1972; HANKS and ANDERSON, 1972). The major reason for the proliferation of papers in this field is the ever-growing collection of physical and chemical data which better define the range of acceptable thermal evolution models. We consider in this section all of the constraints on lunar evolution outlined above, and present thermal history models which closely fit these constraints. The purpose of such calculations can never be to

arrive at a definitive version of the thermal evolution of the moon. Rather, such models are to be used to test and to limit proposed features of lunar origin, lunar history and present-day lunar constitution.

This section represents an extension of our earlier paper (TOKSÖZ et al., 1972c). The computational technique used here is described fully in the earlier work. Briefly, a finite-difference scheme is employed to solve the equation for conservation of thermal energy in a spherically symmetric moon. The effects of melting, differentiation of radioactive heat sources, and simulated convection of molten material are included. Except where noted below, all physical parameters necessary for the calculation are as given in the original reference.

The thermal history models of TOKSÖZ et al. (1972c) were designed to match the chronology of lunar igneous activity, including the early extensive differentiation of the outer portions of the Moon and the extended episode of mare filling, and the evidence cited above for a relatively cool lunar interior today. The present-day heat flow on the lunar surface predicted in the models was about half the Apollo 15 value. We consider models below that are richer in radioactive elements but are otherwise similar to

earlier models in order to place limits on the bulk radioactivity of the Moon.

A separate, but related, question is whether the present constraints on thermal evolution sufficiently limit successful models to either favor or reject the hypothesis of primary chemical zoning, in particular of radioactive heat sources, during the accretion of the Moon (GAST et al., 1970; and others). We conclude that the answer is negative at present.

3.1 Evolution Models to Match Heat Flow

A single measurement of heat flow is a rather tenuous thread on which to hang a theory of lunar evolution. Experience on earth has taught us the folly of relying on one measurement to characterize even a small region. Still, the absence of water and significant tectonic activity argues somewhat against a great deal of local variability of sub-surface temperature. Perhaps more to the point, the Apollo 15 measurement constitutes at least half of the direct heat flow information we are likely to have for some time. That determination must be regarded at present as the best available value and possibly in the near future as one of two bounds on permissible values.

In considering thermal evolution models, several features of the models we presented earlier (TOKSÖZ et al., 1972c) are still required. The evidence for large-scale fractionation of at least the shallow portions of the MOon requires that the outer few hundred kilometers be at near-solidus temperatures at the time the Moon was formed (PAPANASTASSIOU and WASSERBURG, 1971a). This is most readily accomplished by rapid accretion (RINGWOOD, 1966; MIZUTANI et al., 1972; TOKSÖZ et al., 1972c); time scales as short as 100 to 1000 years must be involved or else the energy released by inelastic collisions would have had time to radiate back into space. The only forseeable means of avoiding the conclusion of rapid accretion is to postulate a strong pulse of heat from tidal dissipation, say from close approach of the Moon to the earth. While the energy released in the Moon by such an event may be of the right order of magnitude for melting (SINGER, 1970), the hypothesis is difficult to model quantitatively and to test.

We continue to start from initial temperature profiles derived from a simple model of the accretion process (HANKS and ANDERSON, 1969), and to maintain the scaling of radioactive elements $K/U = 2000$ and $Th/U = 4$ throughout the Moon. For a specified sequence of discrete stages of differentiation of radioactive elements, we may generate a

one-parameter family of thermal evolution models to assay the dependence of the model features on the bulk concentration of uranium in the Moon.

Two such one-parameter families are represented in figs. 3 and 4. The initial temperature distributions for the models of figs. 3 and 4 are 100-year accretion profiles with base temperatures, respectively, of 0°C and 500°C. Differentiation is simulated by upwards concentration at discrete times of all radioactive heat sources to the depth of deepest melting; after each differentiation the heat source concentration is assumed to decay exponentially with depth. The skin depth for the decay law is allowed to decrease with time. The skin depth of the last differentiation is set so that the present-day radioactivity at the lunar surface equals that of the average of soil samples from mare sites, about 1.2 ppm (SLIVER, 1970, 1971, 1972), with the exception that the skin depth is never taken less than the finite-difference grid spacing of 20 km. For the models of fig. 3, the last differentiation was 3.7 b.y. ago; for those in fig. 4 it was 3.0 b.y. ago.

Figs. 3 and 4 give the heat flow and two somewhat arbitrary measures of evolution and present-day state. The lithosphere, as defined in the figures, extends to the depth at which the temperature approaches to within 100°C of the

solidus. The "primordial core" contains undifferentiated material; i.e., at the time of last differentiation the primordial core was solid.

The Apollo 15 heat flow value of 33 ± 5 erg/cm^2-sec (LANGSETH et al., 1972) places rather narrow limits on bulk radioactivity of the Moon. For these famililies of evolution models, the average uranium concentration in the Moon must lie in the range 50 to 80 ppm. These values, and particularly the lower limit, are less than figures cited elsewhere (HANKS and ANDERSON, 1972), principally because of the more complete accounting here of heat of fusion and energy transfer by convection during melting. In particular, our earlier conclusion that the Moon appears to be less radioactive than most eucritic meteorites (CLARK et al., 1967; RIEDER and WÄNKE, 1969) is still valid.

Somewhat higher values of bulk radioactivity are required to reach a given value of heat flow in the models of fig. 3 than those of fig. 4. This is due to the more complete differentiation in the latter models. Because of the higher initial temperatures and the longer allowed differentiation period, the Moon is completely differentiated (i.e., a primordial core is absent) for all models in which the present uranium concentration exceeds about 45 ppb,

whereas the models of fig. 3 possess a primordial core for the entire range of radioactivity considered. A feature of all models matching the Apollo 15 heat flow is a relatively fixed vlaue for the present lithosphere thickness of 400 to 500 km.

The thermal history of a particular member of the family of fig. 3, the model with U = 70 ppb and a present-day heat flow of 33 erg/cm^2-sec, is given in Fig. 5. The time sequence of melting in the model is shown in fig. 6. It may be seen that the model satisfies the major constraints upon lunar evolution. The zone of melting deepens with time. The lithosphere during the first 2 b.y. thickens at the rate of about 160 km/b.y. In particular, the shallowest melting progresses from 155 to 245 km depth during the period of mare filling, in agreement with the depth of origin of mare basalts and with the need for a reasonably thick lithosphere to sustain the stresses associated with mascon gravity anomalies. Between 1 and 2 b.y. in the model, a convecting core develops due to the undifferentiated and relatively radioactive primordial material near the Moon's center. The convecting core grows to a radius of 1200 km at 3 b.y. and then slowly shrinks as the concentration of heat sources decays with time. The Moon is molten below 580 km depth at present in the model. The feature of a molten convecting core is

absent in models (such as those of fig. 4) in which the Moon differentiates completely and concentrates all of the radioactive heat sources toward the surface.

3.2 Models with Primary Accretional Zoning

The major features of the thermal evolution models discussed above can also be satisfied by models in which the decreasing concentration of radioactivity in the Moon is a primary feature associated with a chemically inhomogeneous accretion. Shown in figs. 7 and 8 is a thermal history model following closely one proposed by McCONNELL and GAST (1972). The radioactivity is stratified: if no differentiation had been allowed, the present-day abundance of uranium would be 120 ppb in the uppermost 200 km, 50 ppb in the next 250 km, and 10 ppb in the remainder of the Moon. The average present-day uranium concentration is thus 53 ppb. The ratios K/U and Th/U are held constant. The initial temperature profile is from a Hanks-Anderson accretion model with a base temperature of 0°C and an accretion time of 1000 years; the temperature barely exceeds the solidus between 40 and 140 km depth. Differentiation of radioactive elements is accomplished in four discrete steps between

0 and .9 b.y.

The temperature evolution in the upper few hundred kilometers of the moon is similar to models of comparable bulk radioactivity discussed earlier. The present-day heat flow is 32 erg/cm^2 sec and the Moon is everywhere at least 200°C below the solidus.

The difference in the behavior of the model of fig. 7 from those discussed earlier is that the center of the Moon in this model is tacitly assumed to have been relatively depleted in radioactive elements at cold temperatures. Thus the lunar center heats slowly and the Moon is everywhere solid at present. Whether a cold accretion can accompany primary chemical layering is an important question that must be answered by those advocating such a model. In particular such an origin is incompatible with a molten iron-rich core at an early stage in lunar history. If questions such as these can be resolved and if the Apollo 15 heat flow value holds up, then the temperatures in the deep lunar interior, if discernible, offer the only possible means by which thermal history calculations can distinguish primary accretional zoning from extensive in situ differentiation.

We emphasize that these two alternatives for early lunar conditions do not produce very different thermal regimes in the present-day Moon. Whatever the mechanism,

the high values of heat flow and surface radioactivity together with the requirement that the outer portions of the Moon are cool and have been so for 3 billion years require thermal models in which the radioactive elements are strongly enriched toward the lunar surface early in lunar history. The extensive Rb-Sr fractionation at a similar time requires some near-surface melting (WASSERBURG and PAPANASTASSIOU, 1971), and as yet the extent in depth of the early melting episode has not been established. We see no compelling reason why a major fraction of the lunar mass could not have participated in this early differentiation episode. Even a sub-solidus lunar interior does not rule out an originally homogeneous Moon. If the Moon is initially molten and all heat sources are removed from the lunar interior, or if initial temperature and bulk radioactivity are high enough so that the entire Moon is melted or partially melted within the first 1.5 b.y. and if convective heat transport and segregation of radioactive elements is permitted in the molten zone after melting is only one fourth complete, thermal evolution models satisfying the heat flow can be found which are everywhere solid today. (These models have their own difficulties: such efficient differentiation of heat sources seems improbable, and for some models the near surface temperatures during

the first 2 b.y. are probably too high to have sustained mascon-generated stresses.) Alternatively, convection by solid-state creep will give relatively cool present-day temperatures in the lunar interior without altering significantly the temperature distribution in the upper few hundred kilometers (TOZER, 1972; TOKSÖZ et al., 1972c).

4. DENSITY MODELS FOR THE LUNAR INTERIOR

Because the Moon's moment of inertia is very nearly that of a homogeneous sphere, little attention has been given recently to the density structure of the Moon's deep interior. This is understandable, since a first-order approximation of uniform density is reasonably accurate for most calculations of lunar properties. On the other hand, the physical and chemical evidence discussed above, especially the mean density and moment of inertia and the particulars of the lunar crust, sufficiently limit the range of possible lunar density profiles so that several interesting deductions may be made about the lunar mantle.

Below we formulate simple but plausible density models that are consistent with the latest values for the Moon's

mass and moment of inertia, with several estimates of temperature in the lunar interior, and with the thickness and low densities estimated for the lunar crust. It will be assumed throughout that density in the Moon is a function only of radius. Thus such interesting lateral variations in density associated with the departure of the center of mass from the center of figure (e.g., KAULA et al., 1972), with the differences in the Moon's principal moments of inertia (e.g., MICHAEL and BLACKSHEAR, 1972), and with the mascons (MULLER and SJOGREN, 1968) will be ignored.

4.1 Density of Crustal Rocks

An important aspect of a realistic density model for the Moon, particularly when calculating the moment of inertia, is the inclusion of the relatively thick lunar crust indicated by the seismic data. Knowledge of the major rock types of the crust and measurements or estimates of the density of such materials allows the mean crustal density to be inferred with reasonable accuracy.

The measured densities of mare basalts, corrected for porosity, are 3.3 to 3.4 g/cm^3 at standard temperature and pressure (KANAMORI et al., 1970; STEPHENS and LILLEY, 1970).

But the maria occupy no more than about one-fifth of the Moon's surface area and the density of the highlands must be somewhat less (O'KEEFE, 1968). The density of plagioclase-rich rocks is dominated by anorthite, with density $\rho = 2.76$ g/cm^3. Measured and model values of anorthosites and nonmare basalts are, respectively, 2.8 to 2.9 g/cm^3 and about 3.0 g/cm^3 (WOOD et al., 1970, 1971). Assuming a four to one ratio of plagioclase-rich highland rocks to mare basalts, the mean density of the upper crust of the Moon is about 3.0 g/cm^3 (cf. TURKEVICH, 1971). We shall adopt this value in calculations below.

The density of the lower crust is less certain, and we shall treat this quantity as a free parameter in the range 2.8 (nearly pure anorthite) to 3.4 g/cm^3 (mare basalt). We favor a narrower range of uncertainty, perhaps 3.0 to 3.1 g/cm^3, for several reasons. The terrestrial gabbros, norites and anorthosites with compressional velocities matching the velocity of the lower crust have densities in the ranges, respectively, 2.89 to 3.05 g/cm^3, 2.93 to 3.06 g/cm^3, and 2.71 to 2.81 g/cm^3 (PRESS, 1966; ANDERSON and LIEBERMANN, 1966). Further, the presence of a lower crust suggests that mascon gravity anomalies are more likely associated with relief along the interface between mare basalts and a less dense lower crust (CONEL and HOLSTRUM, 1968) than with relief

along a lunar "Moho" (WISE and YATES, 1970). Thus a lower crustal density of 3.0 to 3.1 g/cm^3 is quite reasonable; the higher value might be weighted slightly by the requirement that the lower crust be more dense than mare basalt liquids at near-liquidus temperatures (see WOOD et al., 1971).

4.2 Temperature

Density is a function of both pressure and temperature. The latter variable is especially important in a body as small as the Moon, and yet as the discussion above has indicated, temperature is only loosely constrained by several various observations, many of them qualitative in nature.

We treat the temperature distribution as imprecisely known, and calculate density models for several temperature profiles. Four such profiles are shown in fig. 9. Profile A is the present-day temperature distribution from fig. 5; the surface heat flow matches the Apollo 15 value. Profiles B and C are two present-day temperature distributions from TOKSÖZ et al. (1972c); the total range of final temperature profiles in the Toksöz et al. thermal history models is indicated by the shaded region if fig. 9 (only models with bulk uranium concentration equal to 23 ppb are included). Profile B (fig. 5 of Toksöz et al.) and profile C (fig. 12 of Toksöz

et al.) have the same initial temperature curve and bulk radioactivity; they differ in that the thermal evolution model resulting in profile C is based on the assumed dominance of solid-state convection as an energy transport mechanism below the lithosphere. Profile D is the temperature model of SONETT et al. (1971), roughly extrapolated to the Moon's center, and is included primarily for historical reasons as a representative "cool" Moon. Whatever life the model has is due to the vigorous arguments of TOZER (1972) that efficient energy transfer by solid-state creep would produce a present-day temperature profile not very different from that of Sonett and co-workers.

4.3 Construction of Density Models

A number of different density models have been calculated for layered, compressible, warm Moons. For each model, the equations of hydrostatic equilibrium and conservation of mass are integrated numerically using a fourth order Runge-Kutta method. The integration step-size in each layer is chosen so that the total mass and moment of inertia of the Moon can be calculated to four-figure accuracy. Temperature is taken from an assumed profile. Densities at each discrete depth are corrected for compression and thermal expansion.

No explicit account is made in the density calculation of partial melting where present in a temperature model.

In the lunar crust, compressibility and thermal expansion are assumed constant and are taken from reported measurements, corrected to low porosity, on mare basalts (STEPHENS and LILLEY, 1970, 1971; BALDRIDGE and SIMMONS, 1971). Values used are, respectively, 1.4 $Mbar^{-1}$ and $2.2 \times 10^{-5} °C^{-1}$. In the Moon's mantle, the pressure and temperature dependence of compressibility and thermal expansion are included. All parameters used are those of forsterite (SKINNER, 1962; KUMAZAWA and ANDERSON, 1969).

4.4 Models with Homogeneous Mantles

Suppose that the lunar mantle is chemically and mineralogically homogeneous, at least to the extent that the entire Moon from a depth of 65 km to the center has a uniform density at standard temperature and pressure. (As used below, "standard" temperature is -20°C, the near-surface temperature of the Moon according to LANGSETH et al., 1972.) If a temperature distribution in the Moon and densities, respectively ρ_1 and ρ_2, at standard conditions for the upper and lower crust are assumed, then the density ρ_3 of the homogeneous mantle follows from the total mass of the Moon, and the moment of

inertia may be readily calculated. However, since we regard the density of the lower crust as not well determined, it is more proper to state that ρ_3 and C/MR^2 are functions of ρ_2. This is illustrated in fig. 10 for the four different temperature models of fig. 9. Also shown is KAULA'S (1969) value for C/MR^2, with the uncertainty indicated by the zone of shading.

Several of the density distributions represented in fig.. 10 are shown in fig. 11. For profile D, the effects on density of temperature and pressure nearly balance out in the lunar interior; the total range of density is only about 1 percent in the mantle. For the warmer temperature profiles, temperature dominates pressure in the lithosphere while the pressure effect is slightly greater than that of temperature in the zone of melting and/or convection. The total variation of density due to pressure and temperature in the lunar mantle for these temperature profiles is 2 to 3 percent. The values of bulk modulus and thermal expansion used for profile B are also shown.

For temperature profiles as cool as profile D (SONETT et al., 1971), fig. 10 illustrates that the Moon's moment of inertia cannot be matched by a density model that has a uniform mantle and yet satisfies the Moon's total mass. For warmer temperature models, the moment of inertia can be fit to

within the present uncertainty over limited ranges of density values for the mantle and lower crust. For profile C, a value for C/MR^2 of .400 is obtained if ρ_2 exceeds 3.38 g/cm^3, a condition we previously deemed unlikely. This would require the density of the mantle, at zero pressure and near-surface temperature, to be about 3.40 g/cm^3. It is of note that this value is very close to the density of the model spinel pyroxenite (ρ = 3.42 g/cm^3) proposed by RINGWOOD and ESSENE (1970) as the material of the lunar mantle. For profiles B and A density models with ρ_2 greater than 3.18 and 3.27 g/cm^3, respectively, and uniform mantles give moments within the lower range of acceptable values (KAULA, 1969). These models have mantle densities, at standard conditions, in the range 3.42 to 3.45 g/cm^3. Such a density could be matched, for instance, by a Ringwood-Essene pyroxenite plus olivine with 100 Mg/(Mg + Fe) less than about 83 (cf. GREEN et al., 1971). The seismic velocity of the pyroxenite or an olivine with greater than 17 mole percent fayalite is too low to account for the possible 9 km/sec layer (ANDERSON and KOVACH, 1972), but is allowed by the most recent results indicating an 8 km/sec mantle.

That temperature profile A gives lower values for C/MR^2 but higher mantle densities than does profile B is due to the fact that higher temperatures in the former profile are

confined to the uppermost 600 km. The effect of this temperature difference may be seen in fig. 11. For the same values of ρ_1 and ρ_2, the mantle above 600 km is less dense and the lower mantle more dense using profile A than if temperature curve B is adopted. This illustrates what should have been obvious: we cannot make C/MR^2 arbitrarily large by increasing the hypothesized temperatures within the Moon. The temperature at depth will be limited by the appropriate melting curves and/or convection stabilization temperatures. A temperature distribution such as profile B maximizes the value of C/MR^2 for other density constraints fixed. We expect that all temperature curves designed to fit the Apollo 15 heat flow, for instance, will give C/MR^2 less than that of profile B unless a solidus curve substantially higher in temperature than the one used here is proposed.

For the temperature profile considered above, none of the density models with uniform mantles gives a value of C/MR^2 equal to .402. Given the present uncertainty in the Moon's moment of inertia, models with C/MR^2 as low as .3995 must be considered acceptable. For profiles C and D and other models invoking solid-state convection (TOZER, 1972), allowable values of C/MR^2 are reached only if the lower crust has an unusually high density. Similarly, density

models using warmer present-day temperatures including those consistent with the Apollo 15 heat-flow value, give acceptable moments of inertia for densities of the lower crust somewhat larger than may reasonably be expected. Thus, we consider below density models in which the mantle is inhomogeneous. Specifically, we treat two-layered mantle models that fit both the Moon's mass and moment of inertia. There are plausible physical explanations of such inhomogeneous mantles that bear strongly on the Moon's early evolution.

The conclusion that the mantle of the Moon is inhomogeneous, we should note, is dependent on the values assumed for the moment of inertia and the crustal thickness. From fig. 10, for instance, it may be seen that a value of .398 or .399 for C/MR^2 would favor a mantle uniform in density and major element chemistry for most temperature models proposed for the Moon. Alternatively, if the crust in the Fra Mauro region of Oceanus Procellarum is unusually thick, say because of the outpouring of a large volume of basaltic lava and the subsequent downbuckling of the crust, then a homogeneous mantle might be permitted even if C/MR^2 exceeds .400. For instance, models with a 30-km thick crust of density (at standard conditions) 2.9 to 3.1 g/cm^3 and a homogeneous mantle of density such as to fit the

total mass of the Moon give $C/MR^2 = .400$ to $.401$ if temperature profile B is used.

4.5 Models with Inhomogeneous Mantles

As a simple first approximation to an inhomogeneous lunar mantle, we consider the mantle to be composed of two homogeneous layers. If the densities of the crust and a temperature profile are assumed, then the densities of the upper and lower portions of the mantle are single-valued functions of the depth to the boundary between the two layers. To satisfy the mean lunar density and $C/MR^2 = .402$, the upper mantle must be denser than the lower mantle at similar pressure and temperature conditions. The precise density contrast between upper and lower mantle is a strong function of other parameters used in constructing the density model.

This is illustrated in fig. 12, where we plot ρ_3 and ρ_4, respectively the densities at standard conditions of the upper and lower mantle, versus the normalized radius of the lower mantle. Curves are shown for the several temperature distributions discussed earlier; densities of the upper mantle generally exceed 3.5 g/cm^3; lower mantle

densities are consistently less than 3.5 g/cm^3. These compare with a mean lunar density, at standard conditions, of 3.35 to 3.42 for the temperature models considered. Minimum density contrast occurs at a lower mantle radius of .7 to .8 R (350 to 500 km depth). This minimum contrast depends on the temperature model and the assumed lower crust density but is in the range .16 to .28 g/cm^3 for the curves shown in fig. 10.

A density reversal in the lunar mantle is, of course, gravitationally unstable. Thus for such a reversal to have persisted for several billion years requires that the Moon maintained considerable strength over that time period, at least to a depth somewhat in excess of the upper to lower mantle transition. This requirement, in view of the possibility that the deep lunar interior may convect by solid-state creep at moderate temperatures (TURCOTTE and OXBURGH, 1969; TOZER, 1972), strongly favors a thin upper mantle.

The limitations on mantle structure may be put in somewhate more quantitative form. Imagine that a thin dike of lower mantle material penetrates the upper mantle to the base of the crust. Then because of the density contrast, there will be a difference in pressure between the base of the dike and the base of the normal upper mantle. The maximum shear stress τ at the base of the dike, equal to

half the pressure difference, is plotted for each temperature-density profile in fig. 12 as a function of lower mantle radius. The smallest values of τ are 200 to 300 bars, depending on the temperature model; τ increases with the thickness of the upper mantle, though is still within 10 percent of its minimum value for $R/R_3 = .9$ (upper mantle thickness 110 km). Even the smallest values of these shear stresses are 2 to 5 larger than the creep strength of the lunar crust inferred from crater dimensions (BALDWIN, 1968) and the maximum shear stresses estimated to occur beneath mascons (CONEL and HOLSTRUM, 1968; O'KEEFE, 1968; WISE and YATES, 1970). Thus the density inversions indicated in fig. 12 would be unstable to solid-state creep, a conclusion that would be strengthened by considering the additional density decrease with depth due to the dominance of thermal expansion over compression (see fig. 11). We conclude that either (i) a value for C/MR^2 of .402 is untenable and KAULA'S (1969) lower limit of .400 is more probably an upper bound, (ii) the strength of lunar material increases with depth, or (iii) the strength of the lunar lithosphere increases with time and the density inversion implied by $C/MR^2 = .402$ is a feature more recent than the filling of the circular mare basins and than the formation of most craters. We consider these possibilities further below.

The density contrasts between upper and lower mantles in the models of fig. 12 were calculated using $C/MR^2 = .402$. If Kaula's lower limit of .400 is assumed, then the density contrast and implied shear stresses will be less for a given upper mantle thickness. For instance, if $\rho_1 = 3.0$ g/cm^3, $\rho_2 = 3.1$ g/cm^3 and temperature profile B is adopted, a thin (20 to 40 km thick) upper mantle with density 3.7 g/cm^3 at standard conditions will give $C/MR^2 = .400$; the lower mantle density is 3.43 to 3.44 g/cm^3 for such models. Such a thin dense layer fits with the suggestion of a high-velocity layer beneath the crust discussed above. Further, the maximum shear stresses associated with the gravitational instability are only 40 to 80 bars. It is not improbable that the upper 100 km of the Moon could have supported such stresses for the required several billion years.

4.6 Possible Explanations of a Density Inversion

The boundary between upper and lower mantle, if valid, represents a chemical and/or mineralogical transition. At least three possible explanations, not completely independent, of such a transition may be envisioned: (1) The upper mantle consists of a high-pressure version of the lower crust (cf. ANDERSON and KOVACH, 1972). The crust-

mantle boundary is a phase boundary associated with the breakdown of plagioclase. (2) The upper mantle is the residuum left behind after melting and fractionation of the lunar crust. The upper mantle-lower mantle boundary represents the lower limit of melting in an early period of lunar igneous activity. (3) As a result of a differentiation process involving the bulk of the Moon, the upper mantle is richer in Fe (SMITH et al., 1970b) or in Ca and Al (in high-pressure phases) than the lower mantle.

The possibility that the upper mantle is merely a high-pressure form of the lunar crust is explored in fig. 13. Shown there are the stability fields of mineral assemblages for mare basalt (RINGWOOD and ESSENE, 1970) and a terrestrial gabbroic anorthosite (GREEN, 1970); also shown are the ranges of reported stability boundaries for the plagioclase end members. All of these curves are extrapolations from higher temperatures and pressures and must be considered approximate at best. Superimposed on the phase boundary diagrams are several possible temperature curves for the shallow portions of the Moon; also indicated are the pressures at the base of the upper and lower crust.

It is immediately apparent that if a high density form of the aluminum-rich lower crust constitutes the upper mantle,

then the crust-mantle interface is probably not an equilibrium boundary. It might, however, be a rate-process boundary. Though the transition zone for the plagioclase-rich material in fig. 13 is wide, it is not necessary that the accompanying density increase be a gradual one uniformly distributed over the transition interval. The work of ITO and KENNEDY (1970) on the basalt-eclogite transition in an olivine tholeiite suggests that the largest density jump within the transition of the calcium-rich lunar material will occur at pressures near to or somewhat less than the anorthite breakdown boundary. Thus the crust-mantle boundary could conceivably be a phase boundary with a substantial density contrast if a rate-limiting temperature curve intersects the P-T curve of the largest density increase at a pressure corresponding to 65 km depth. The metastable boundary would have been frozen in when the temperature at 65 km cooled below the rate-limiting value, an event which might have occurred relatively recently in lunar history.

If the upper mantle and lower crust do not have the same composition, but the upper mantle is richer in Al and Ca than the lower mantle, then the density contrast between upper and lower mantle may still be due to the instability of feldspar in the lunar interior. To illustrate

this we have drawn in fig. 5, superimposed on the thermal history diagram, the approximate boundary between feldspathic and spinel pyroxenite for the mare-basalt parent material proposed by RINGWOOD and ESSENE (1970). The deduction to be drawn from the figure is that the spinel pyroxenite assemblage would have become stable in the upper mantle only 1 to 2 b.y. after lunar origin. The earliest phase change would have occurred at the base of the lithosphere, and it is possible that gravitational sinking of chunks of the transformed lithosphere into the underlying molten zone maintained the lithosphere thickness at a nearly constant value for some time. The transformation to the dense assemblage for most of the upper mantle might then have occurred later than suggested by fig. 5 and thus the shear stresses of fig. 12 might be marginally permissible.

If both the crust and upper mantle are richer in Al and Ca than the lower mantle, then the Moon must have undergone a complicated differentiation process involving most if not all of the lunar mass either during or shortly after accretion. Suppose, however, that the higher density upper mantle is residual material remaining after the melting episode during which the lunar crust was formed. Then a natural question to ask is whether the lower mantle has

the same major element composition as the average of crust and upper mantle, i.e. whether an evolutionary sequence calling for accretion of the Moon from material homogeneous in density and differentiation *in situ* of the crust and upper mantle is permitted by the constraints of mass and moment of inertia. A requirement of such an evolution is that the density of the lower mantle equal the average density of crust and upper mantle and, thus, the mean density of the Moon, all densities measured at standard conditions. The mean density of the Moon at standard conditions is indicated by an arrow in the lower left of fig.12 for each temperature profile of fig. 3. The lower mantle density ρ_4 is at least .7 percent less than the mean lunar density $\bar{\rho}$ for profiles C and D. For profiles A and B, ρ_4 lies within .5 percent of $\bar{\rho}$ if R_3/R exceeds, respectively, .90 and .86, corresponding to depths to the lower mantle of 170 and 240 km; the upper mantle density must exceed 3.6 g/cm^3.

The calculations above have neglected two phenomena which affect the comparison of ρ_4 with $\bar{\rho}$: melting and solid-solid phase transformations. If portions of the lower mantle are molten, then we should raise ρ_4 before comparison with the average density of the presumably solid crust and upper mantle. (This latter density will

still equal the value of $\bar{\rho}$ shown in fig. 12, but the mean lunar density at standard conditions will not.) Limited data indicate that the change in density of a rock upon melting at zero pressure is about 10 percent (SKINNER, 1966); because of the larger compressibility of the liquid phase (MURASE and SUZUKI, 1968), this density change will decrease with pressure. Estimates of the volume change at melting obtained by combining thermodynamic data (ROBIE and WALDBAUM, 1968) with the slopes of the melting curves for feldspars, pyroxenes and olivines (BOYD and ENGLAND, 1963; BOYD et al., 1964; AKIMOTO et al., 1967) lie in the range 3 to 9 percent at 20 kb pressure. Thus at depths below 400 km in the Moon a volume change of perhaps no more than 6 percent upon melting should be expected. Further, it is unlikely that there are extensive regions of complete melting; heat transfer by convective transport would quickly cool a thoroughly molten zone. We expect that 20 to 25 percent melting by volume is a generous upper limit to the extent of melting. For larger melt concentrations, upwards migration of the liquid phase would be anticipated. To sum up, it is unlikely that melting will affect density by more than about 1.5 percent; because none of our thermal models has a present-day temperature profile that shows melting shallower than about 500 km, the effect of melting on lower mantle density will be to increase our estimate of ρ_4 for profiles A and B by about .5 to 1.5 percent, depending on the choice of depth to the lower mantle.

The effect of solid-solid phase changes on ρ_4 is critically dependent on the assumed composition. The basalt-eclogite transition in mare basalts is accompanied

by a density increase estimated to be between 7 and 11 percent (RINGWOOD and ESSENE, 1970; GREEN et al., 1971). The more plagioclase-rich highland and lower crustal material should have a larger density jump. The breakdown of pure anorthite involves an increase of density of 27 percent GREEN (1970) estimated that a terrestrial gabbroic anorthosite should give an 11 percent density rise after disappearance of plagioclase. A reasonable estimate for the density difference between the high pressure and low pressure forms of average lunar crustal material is 10 percent.

The lunar crust constitutes 10 percent of the mass and 11 percent of the volume of the Moon. If the lower mantle is isochemical with a mix of crust and upper mantle, then the correction to ρ_4 which we must apply due to pressure-induced phase changes depends on the thickness of the upper mantle. We assume the upper mantle is devoid of Al and Ca; then the density increase in the lower mantle due to the phase-transformed crustal material is the correction to be considered subtracted from ρ_4. Lower mantle radii of .9R, .8R, and .7R would imply, for instance, that lunar crustal composition amounts to, respectively, 39, 22 and 16 percent by volume of the lower mantle. Thus ρ_4 should be lowered by, respectively, 3.9, 2.2 and 1.6 percent for the above values of R_3.

Let us reconsider whether ρ_4 can equal the average density of crust and upper mantle if all densities are measured at standard conditions. For temperature profiles C and D, there is no correction to ρ_4 due to partial melting, but ρ_4 should be lowered if solid-solid phase transformations are considered. Thus ρ_4 must be less than the average density of crust and upper mantle by about 4 percent or more for these temperature models. For profiles A and B, corrections due both to partial melting and to solid-solid transitions must be made. Following the arguments given above, we corrected ρ_4 for these effects for the density models of fig. 12 associated with temperature profile B. This corrected ρ_4 (see fig. 12) shows a relative maximum at about $R_3/R = .7$, but for all values of R_3/R, ρ_4 is at least 2 percent less than the average density of crust and upper mantle. A similar conclusion can be made for profile A models.

Thus for all temperature models considered, a value for C/MR^2 of .402 can be met only if the lower mantle of the Moon is less dense at standard conditions than the combined crust and upper mantle. This could be achieved by smaller amounts of Al and Ca or of Fe in the lower mantle than in the average crust-upper mantle material. In either case, the composition of the lower mantle does

not match the bulk composition of the Moon and extensive differentiation of the Moon, either during or somewhat later than the time of accretion, is required. This conclusion has been reached by other workers (HUBBARD and GAST, 1971) using somewhat different reasoning.

That primary accretional zoning of major elements in the Moon is a strong possibility lends some support to thermal evolution models with primordial zoning of radioactive elements. Further, if the contrast in heat sources between a radioactive upper mantle and a lower mantle poor in radioactivity is sufficiently large, then temperature in the lower mantle might have remained cool throughout lunar history. In the model of fig. 7, for instance, the Moon below 450 km has never been molten and present-day temperature decreases with depth throughout much of the lower mantle. This type of model may offer a solution to the stresses implied at the base of the upper mantle by inhomogeneous density models designed to match the Moon's moment of inertia. The strength of the lower mantle in such a thermal model has been greater than that of the lunar crust for most of the Moon's history and has consistently been an increasing function of depth below 400 to 700 km.

5. ON A CORE

The existence of a predominantly-iron core, and the requirement that it be molten from 3 to 4 b.y. ago, would place interesting constraints on early lunar history. In particular, for the lunar center to be at a temperature above, say, the Fe-FeS eutectic (BRETT and BELL, 1969) at 4 b.y. ago, either the Moon must have formed at such a temperature to begin with or have formed at somewhat cooler temperatures (~500°C) and have begun with substantial radioactivity at depth. In either case, Moon-wide differentiation is strongly suggested.

A thermal history model such as that of fig. 5 is consistent with this idea. Temperatures .5 b.y. after lunar origin exceed the Fe-FeS eutectic, also shown in the figure, throughout most of the Moon. Thus core formation by melting, sinking and aggregation of iron-rich droplets is achieved prior to the formation of the oldest lunar rocks possessing remanent magnetization. Thermal history models such as that of fig. 7, with initially cold interiors depleted in radioactive elements, are inconsistent with an early molten core. A feature common to most, if not all, thermal evolution models yielding formation of an Fe-FeS core prior to 4 b.y. ago is that the core should still be

molten or partially molten today. Thus depending on the sulfur content of the core, one might have to invoke some argument other than core solidification (e.g. decay of heat sources) to explain the lack of appreciable dipole magnetic field associated with the Moon at present.

The presence today of even a pure-iron core is not precluded by the moment of inertia. Limits can be placed on the size of such a core, but the limits depend upon several assumed properties. Assuming values for the densities of the core and the upper and lower crust, and adopting a present-day temperature profile, one may calculate the density of the mantle, assumed homogeneous, and moment of inertia from the total mass of the Moon. This is done in fig. 14 for two rough limits. In the optimistic curve, the lower crust is given a density of 3.4 g/cm^4, the temperature distribution is taken from a thermal evolution model with initially molten Moon with present-day bulk uranium concentration 23 ppb, and the core is taken to be 12 percent less dense than iron (modeled after the earth's outer core, see PRESS, 1970). In the pessimistic curve, the lower crust is given a density of 3.0 g/cm^3, the temperature distribution is that of SONETT et al. (1971), and the core is taken to be pure iron. The predicted C/MR^2 for the pessimistic model is too low and requires an inhomogeneous

mantle even if no core is present. The optimistic model allows a small core (R_c/R = .14, or .005 of the lunar mass) even with a homogeneous mantle. For such a core, the mantle density (at standard conditions) is lowered about .3 percent from the core-free value. Using a temperature model with higher radioactivity so as to satisfy the Apollo 15 heat flow would allow an even smaller core (R_c/R = .09) without postulating an inhomogeneous mantle.

If the Moon contains a small iron-rich core with additional sulfur, then the suggestion of LEWIS (1971) and HALL and MURTHY (1971) that potassium would have to be enriched in an Fe-FeS melt relative to silicates has important implications for thermal evolution. This is illustrated in fig. 15. In fig. 15a is shown the thermal evolution for an initially molten moon with U = 11 ppb, K/U = 2000, and Th/U = 4. All radioactive elements are concentrated toward the lunar surface shortly after the time of lunar formation. The model predicts a solid Moon today and a surface heat flow of 10 erg/cm^2-sec. In fig. 15b is shown the thermal evolution for a moon with the same initial temperature profile and U and Th abundance, but a chondritic K/U ratio of 80 000 (WASSERBURG et al., 1964). The near-surface radioactive heat generation is the same as in fig. 15a, but 39/40 of the potassium is assumed to

remain in a 340 km radius core. The result, while not profound, is spectacular. Heat from the additional potassium is sufficient to keep most of the Moon melted throughout its history. The Moon is molten below 300 km at present and the surface heat flow is 17 erg/cm^2-sec. These calculations are not intended to be realistic: the Moon is not chnodritic and an iron core, if present, should probably not be currently molten. Rather these results are intended to demonstrate the importance of properly accounting for all heat sources in performing thermal history calculations.

6. CONCLUSIONS

A wide assortment of data now constrain models of the composition, structure, and evolution of the Moon's interior. We have quantitatively examined some of these constraints and the suite of lunar models consistent with them. Our findings include the following:

(1) Models of the thermal evolution of the Moon that fit the chronology of surface igneous activity, the need for a cool, rigid lithosphere since the formation of mascons, and the surface concentrations of radioactive

elements all involve extensive differentiation and upwards concentration of radioactive heat sources early in lunar history. This differentiation may be either a primary accretional feature or a product of nearly Moon-wide melting.

(2) If the Apollo 15 heat-flow value of 33 ± 5 erg/cm^2-sec (LANGSETH et al., 1972) is representative of the Moon, then the average concentration of uranium in the Moon is currently 65 ± 15 ppb, assuming the Th/U and K/U ratios of lunar surface rocks hold throughout the interior. Such models have lithospheres 400 to 500 km thick at present and may or may not be partially melted at greater depths. We caution, however, that rigid application of surface heat flow as a constraint on the Moon's thermal evolution should await the Apollo 17 heat-flow experiment.

(3) Thermal history calculations are only marginally useful for distinguishing between primary accretional zoning of radioactive heat sources and an early melting episode including extensive differentiation. The major difference between the two sets of models is the temperature of the innermost 1000 km, a region of the Moon for which

independent information from seismic velocity or electrical conductivity studies is currently lacking.

(4) Density models for the Moon, including the effects of pressure and temperature, can be made to satisfy the mass of the Moon, KAULA'S (1969) value for C/MR^2 of .402 ± .002, and the presence of a low-density crust some 65 km thick (TOKSÖZ et al., 1972a, b) only if the mantle of the Moon is chemically inhomogeneous. Specifically, the density of the upper mantle must exceed the density at similar pressure and temperature of the lower mantle by a minimum of 5 percent. The need for an inhomogeneous mantle can be avoided if C/MR^2 is less than .400 or, alternatively, if the average lunar crust is considerably thinner than in the Fra Mauro region of Oceanus Procellarum. For models with homogeneous mantles, the mantle density is equal to that of a pyroxenite or olivine pyroxenite, in agreement with seismic velocity (TOKSÖZ et al., 1972a, b) and petrological (RINGWOOD and ESSENE, 1970) considerations. For the more likely models with inhomogeneous mantles, the upper mantle density probably exceeds 3.5 g/cm^3. If the upper mantle was the source region for mare basalts, then considerations of mantle

mineralogy based on assumed densities (e.g. GREEN et al., 1971) will need revision.

(5) The density inversion suggested for the mantle of the Moon is gravitationally unstable. To match $C/MR^2 = .402$, the maximum shear stress at the base of a column or dike of lower mantle penetrating the upper mantle must be 2 to 5 times the maximum stresses associated with the Moon's gravity field. Such stresses could not generally have persisted throughout lunar history, suggesting (i) C/MR^2 for the Moon is more properly .400 or less; or (ii) the high-density of the upper mantle is a feature more recent than the last major episode of melting and igneous activity, and is perhaps a result of a Ca-Al rich upper mantle passing through a phase boundary during cooling; or (iii) the deep interior has always been relatively cool and capable of supporting reasonably large stress differences, a suggestion which can only be satisfied by thermal models invoking primary depletion of heat sources in the interior of a moon accreted at cold temperatures (GAST and McCONNELL, 1972).

(6) From the density contrast between upper and lower mantle

required if $C/MR^2 = .402$, the lower mantle must be less dense at standard temperature and pressure than the combined crust and upper mantle. This conclusion is strengthened by considering the possible effects on density of partial melting and solid-solid phase transitions. Thus models of lunar evolution calling for homogeneous accretion and in situ differentiation of the crust and upper mantle are ruled out, and primary or early moon-wide differentiation of the major elements (especially Fe, Ca, Al) is required.

(7) A small iron-rich core and a chemically uniform mantle are permitted for some temperature models and for some values of crustal density. The radius of the core can be no more than 14 percent of the lunar radius if the mantle is homogeneous. The presence of a heavy core in the Moon exacerbates the problems of density inversion and implied stresses required by the moment of inertia.

(8) Confirmation of an iron-rich core in the Moon, and the need for it to have been molten between 3 and 4 b.y. ago to have generated an internal lunar magnetic field, would have very important implications for

lunar thermal evolution. The initial temperature in the deep interior of the Moon would have to exceed 1000°C or, if cooler, would have to be sufficiently rich in radioactive heat sources so that such a temperature is reached in the first .5 b.y. Further, the likely presence of K^{40} in an Fe-FeS core would alter the distribution of heat sources commonly assumed in thermal history calculations and would probably yield a molten core at present.

ACKNOWLEDGEMENTS

This research was supported by National Aeronautics and Space Administration Grant NGL 22-009-187.

REFERENCES

ADLER, I., J. TROMBKA, J. GERARD, P. LOWMAN, R. SCHMADEBECK, H. BLODGET, E. ELLER, L. YIN, R. LAMOTHE, P. GORENSTEIN and P. BJORKHOLM (1972a), Science 175, 436.

ADLER, I., J. TROMBKA, J. GERARD, P. LOWMAN, R. SCHAMDEBECK, H. BLODGET, E. ELLER, L. YIN, R. LAMOTHE, G. OSSWALD, P. GORENSTEIN, P. BJORKHOLM, H. GURSKY and B. HARRIS (1972b), Science 177, 256.

AKIMOTO, S., E. KOMADA and I. KUSHIRO (1967), J. Geophys. Res. 72, 679.

ANDERSON, D.L. and R.L. KOVACH (1972), Phys. Earth Planet. Interiors, in press.

ANDERSON, O.L. and R.C. LIEBERMANN (1966), Sound velocities in rocks and minerals, VESIAC State-of-the-Art Report No. 7885-4-X (Willow Run Laboratories, University of Michigan), 189 pp.

ARNOLD, J.R., L.E. PETERSON, A.E. METZGER and J.I. TROMBKA (1972), Gamma-ray spectrometer experiment. In: Apollo 15 Preliminary Science Report (National Aeronautics and Space Administration, Washington, D.C.), 16-1.

BALDRIDGE, W.S. and G. SIMMONS (1971), Geochim. Cosmochim. Acta, Suppl. 2, 2317.

BALDWIN, R.B. (1968), Icarus 9, 401.

BIRCH,F. and P. LE COMTE (1960), Am. J. Sci. 258, 209.

BOETTCHER, A.L. and P.J. WYLLIE (1968), Geochim. Cosmochim. Acta 32, 999.

BOYD, F.R. and J.L. ENGLAND (1963), J. Geophys. Res. 68, 311.

BOYD, F.R., J.L. ENGLAND and B.T.C. DAVIS (1964), J. Geophys. Res. 69, 2101.

BRETT, R. and P.M. BELL (1969), Earth Planet. Sci. Letters 6, 479.

CLARK, R.S., M.W. ROWE, R. GANAPATHY and P.K. KURODA (1967), Geochim. Cosmochim. Acta 31, 1605.

COLEMAN, P.J., JR., G. SCHUBERT, C.T. RUSSELL and L.R. SHARP (1972), The particles and fields subsatellite magnetometer experiment. In: Apollo 15 Preliminary Science Report (National Aeronautics and Space Administration, Washington, D.C.), 22-1.

CONEL, J.E. and G.B. HOLSTRUM (1968), Science 162, 1403.

DUBA, A., H.C. HEARD and R.N. SCHOCK (1972), Earth Planet. Sci. Letters, in press.

DYAL, P. and C.W. PARKIN (1971), Geochim. Cosmochim. Acta, Suppl. 2, 2391.

DYAL, P., C.W. PARKIN and P. CASSEN (1972b), Geochim. Cosmochim. Acta, Suppl. 3, in press.

DYAL, P., C.W. PARKIN, C.W. SNYDER and D.R. CLAY (1972a), Nature 236, 381.

DYAL, P., C.W. PARKIN and C.P. SONETT (1970), Science 169, 762.

ENGLELHARDT, W. VON, J. ARNDT, W.F. MÜLLER and D. STÖFFLER (1970), Geochim. Cosmochim. Acta, Suppl. 1, 363.

ENGLAND, A.W., G. SIMMONS and D. STRANGWAY (1968), J. Geophys. Res. 73, 3219.

GAST, P.W., N.J. HUBBARD and H. WIESMANN (1970), Geochim. Cosmochim. Acta, Suppl. 1, 1143.

GOLES, G.G., K. RANDLE, M. OSAWA, R.A. SCHMITT, H. WAKITA, W.D. EHMANN and J.W. MORGAN (1970), Geochim. Cosmochim. Acta, Suppl. 1, 1165.

GRAHAM,A.L.and A.E. RINGWOOD (1971), Earth Planet. Sci. Letters 13, 105.

GREEN, D.H., A.E. RINGWOOD, N.G.WARE AND W.O. HIBBERSON (1972), Geochim. Cosmochim. Acta, Suppl. 3, in press.

GREEN, D.H., A.E. RINGWOOD, N.G. WARE, W.O. HIBBERSON, A. MAJOR and E. KISS (1971), Geochim. Cosmochim. Acta, Suppl. 2, 601.

GREEN, T.H. (1970), Phys. Earth Planet. Interiors 3, 441.

HALL, H.T. and V.R. MURTHY (1971), Earth Planet. Sci. Letters 11, 239.

HANKS, T.C. and D.L. ANDERSON (1969), Phys. Earth Planet. Interiors 2, 19.

HANKS, T.C. and D.L. ANDERSON (1972), Phys. Earth Planet. Interiors, in press.

HARIYA, Y. and G.C. KENNEDY (1968), Am. J. Sci. 266, 193.

HASKIN, L.A., R.O. ALLEN, P.A. HELMKE, T.P. PASTER, M.R. ANDERSON, R.L. KOROTEV and K.A. ZWEIFEL (1970), Geochim. Cosmochim. Acta, Suppl. 1, 1213.

HAYS, J.F. (1967), Carnegie Inst. Yearbook 65, 234.

HAYS, J.S. (1972), Phys. Earth Planet. Interiors 5, 77.

HELSLEY, C.E. (1970), Geochim. Cosmochim. Acta, Suppl. 1, 2213.

HOUSLEY, R.M. and F.J. MORIN (1972), The Moon 4, 35.

HUBBARD, N.J. and P.W. GAST (1971), Geochim. Cosmochim. Acta, Suppl. 2, 999.

HUBBARD, N.J., C. MEYER, JR., P.W. GAST and H. WIESMANN (1971), Earth Planet. Sci. Letters 10, 341.

HUSAIN, L., O.A. SCHAEFFER and J.F. SUTTER (1972), Science 175, 428.

ITO, K. and G.C. KENNEDY (1971), An experimental study of the basalt-garnet granulite-eclogite transition. In: J.G. Heacock, ed., The Structure and Physical Properties of the Earth's Crust, Amer. Geophys. Un. Mon. 14, 303.

KANAMORI, H., A. NUR, D.H. CHUNG and G. SIMMONS (1970), Geochim. Cosmochim. Acta, Suppl. 1, 2289.

KAULA, W.M. (1969), Science 166, 1581.

KAULA, W.M. (1971), EOS, Trans. Amer. Geophys. Un. 52, IUGG1.

KAULA, W.M., R.E. LINGENFELTER, G. SCHUBERT, W.L. SJÖGREN, and W.R. WOLLENHAUPT (1972), EOS, Trans. Amer. Geophys. Un. 53, 440.

KING, E.A., JR., M.F. CARMAN and J.C. BUTLER (1970), Geochim. Cosmochim. Acta, Suppl. 1, 599.

KUMAZAWA, M. and O.L. ANDERSON (1969), J. Geophys. Res. 74, 5961.

LANGSETH, M.G., JR., S.P. CLARK, JR., J.L. CHUTE, JR., S.J. KEIHM and A.E. WECHSLER (1972), Heat-flow experiment. In: Apollo 15 Preliminary Science Report (National Aeronautics and Space Administration, Washington, D.C.), 11-1.

LATHAM, G., M. EWING, J. DORMAN, D. LAMMLEIN, F. PRESS, N. TOKSÖZ. G. SUTTON, F. DUENNEBIER and Y. NAKAMURA (1971), Science 174, 687.

LEWIS, J.S. (1971), Earth Planet. Sci. Letters 11, 130.

LIU, A.S. and P.A. LAING (1971), Science 173, 1017.

LORELL, J. (1970), The Moon 1, 190.

LSAPT (Lunar Sample Analysis Planning Team)(1972), Science 176, 975.

LUNATIC ASYLUM (1970), Earth Planet. Sci. Letters 9, 137.

McCONNELL, R.K., JR. and P.W. GAST (1972), The Moon 5, in press.

McCORD,T.B., M.P. CHARETTE, T.V. JOHNSON, L.A. LEBOFSKY, C. PIETERS and J.B. ADAMS (1972), J. Geophys. Res. 77, 1349.

MICHAEL, W.H., JR. and W.T. BLACKSHEAR (1972), The Moon 3, 388.

MICHAEL, W.H., JR., W.T. BLACKSHEAR and J.P. GAPCYNSKI (1970), Results on the mass and gravitational field of the Moon as determined from dynamics of lunar satellites. In: B. Morando, ed., Dynamics of Satellites (1969) (Springer-Verlag, Berlin), 42.

MIZUTANI, H., T. MATSUI and H. TAKEUCHI (1972), The Moon 4, 476.

MULLER, P.M. and W.L. SJOGREN (1968), Science 161, 680.

MURASE, T. and T. SUZUKI (1966), J. Fac. Sci. Hokkaido Univ., Ser. 7, 2, 273.

MUTCH, T.A. (1970), Geology of the Moon, A Stratigraphic View (Princeton University Press, Princeton, N.J.), 324 pp.

NAGATA, T., Y. ISHIKAWA, H. KINOSHITA, M. KONO, Y. SYONO and R.M. FISHER (1970), Geochim. Cosmochim. Acta, Suppl. 1, 2325.

NEWTON, M.S. and G.C. KENNEDY (1968), Am. J. Sci. 266, 728.

O'KEEFE, J.A. (1968), Science 162, 1405.

PAPANASTASSIOU, D.A. and G.J. WASSERBURG (1970), Earth Planet. Sci. Letters 8, 269.

PAPANASTASSIOU, D.A. and G.J. WASSERBURG (1971a), Earth Planet. Sci. Letters 11, 37.

PAPANASTASSIOU, D.A. and G.U. WASSERBURG (1971b), Earth Planet. Sci. Letters 12, 36.

PAPANASTASSIOU, D.A. and G.J. WASSERBURG (1972), Earth Planet. Sci. Letters 13, 368.

PAPANASTASSIOU, D.A., G.J. WASSERBURG AND D.S. BURNETT (1970), Earth Planet. Sci. Letters 8, 1.

PEARCE, G.W., D.W. STRANGWAY and E.E. LARSON (1971), Geochim. Cosmochim. Acta, Suppl. 2, 2451.

PHILPOTTS, J.A. and C.C. SCHNETZLER (1970), Geochim. Cosmochim. Acta, Suppl. 1, 1471.

PRESS, F. (1966), Seismic velocities. In: S.P. Clark, Jr., ed., Handbook of Physical Constants, Geol. Soc. Am. Mem. 97, 195.

PRESS, F. (1970), Phys. Earth Planet. Interiors 3, 3.

REISZ, A.C., D.L. PAUL and T.R. MADDEN (1972), The Moon 4, 134.

REYNOLDS, R.T., P.E. FRICKER and A.L. SUMMERS (1972), Thermal history of the Moon. In: J.W. Lucas, ed., Thermal Characteristics of the Moon (MIT Press, Cambridge, Mass.), 303.

RIEDER, R. and H. WÄNKE (1969), Study of trace element abundance in meteorites by neutron activation. In: P.M. Millman, ed., Meteorite Research (D. Reidel, Dordrecht, Holland), 75.

RINGWOOD, A.E. (1966), Geochim. Cosmochim. Acta 30, 41.

RINGWOOD, A.E. and E. ESSENE (1970), Geochim. Cosmochim. Acta, Suppl. 1, 769.

ROBIE, R.A. and D.R. WALDBAUM (1968), U.S. Geol. Surv. Bull. 1259, 256 pp.

RUNCORN, S.K., D.W. COLLINSON, W. O'REILLY, M.H. BATTEY, A. STEPHENSON, J.M. JONES, A.J. MANSON and P.W. READMAN (1970), Geochim. Cosmochim. Acta, Suppl. 1, 2369.

SHORT, N.M. (1970), Geochim. Cosmochim. Acta, Suppl. 1, 865.

SILL, W.R. (1972), The Moon 4, 3.

SILVER, L.T. (1970), Geochim. Cosmochim. Acta, Suppl. 1, 1533.

SILVER, L.T. (1971), Second Lunar Science Conf. (unpublished proceedings).

SILVER, L.T. (1972), Geochim. Cosmochim. Acta, Suppl. 3, in press.

SINGER, S.F. (1970), EOS, Trans. Amer. Geophys. Un. 51, 637.

SKINNER, B.J. (1962), U.S. Geol. Surv. Prof. Paper 450D, 109.

SKINNER, B.J. (1966), Thermal expansion. In: S.P. Clark, Jr., ed., Handbook of Physical Constants, Geol. Soc. Am. Mem. 97, 75.

SMITH, J.V., A.T. ANDERSON, R.C. NEWTON, E.J. OLSEN and P.J. WYLLIE (1970b), J. Geol. 78, 381.

SMITH, J.V., A.T. ANDERSON, R.C. NEWTON, E.J. OLSEN. P.J. WYLLIE , A.V. CREWE, M.S. ISAACSON and D. JOHNSON (1970a), Geochim. Cosmochim. Acta, Suppl. 1, 897.

SOLOMON, S.C. and M.N. TOKSÖZ (1968), Phys. Earth Planet. Interiors 1, 475.

SONETT, C.P., D.S. COLBURN, P. DYAL, C.W. PARKIN, B.F. SMITH, G. SCHUBERT and K. SCHWARTZ (1971), Nature 230, 359.

STEPHENS, D.R. and E.M. LILLEY (1970), Geochim. Cosmochim. Acta, Suppl. 1, 2427.

STEPHENS, D.R. and E.M. LILLEY (1971), Geochim. Cosmochim. Acta, Suppl. 2, 2165.

STRANGWAY, D.W., E.E. LARSON and G.W. PEARCE (1970), Geochim. Cosmochim. Acta, Suppl. 1, 2435.

TOKSÖZ, M.N., F. PRESS, K. ANDERSON, A. DAINTY, G. LATHAM, M. EWING, J. DORMAN, D. LAMMLEIN, G. SUTTON, F. DUENNEBIER, and Y. NAKAMURA (1972a), Science 176, 1012.

TOKSÖZ, M.N., F. PRESS, K. ANDERSON, A. DAINTY, G. LATHAM, M. EWING, J. DORMAN, D. LAMMLEIN, G. SUTTON, F. DUENNEBIER and Y. NAKAMURA (1972b), Geochim. Cosmochim. Acta, Suppl. 3, in press.

TOKSÖZ, M.N., S.C. SOLOMON, J.W. MINEAR and D.H. JOHNSTON (1972c), The Moon 4, 190 and 5, 249.

TOZER, D.C. (1972), The Moon 5, in press.

TURCOTTE, D.L. and E.R. OXBURGH (1969), Nature 223, 250.

TURKEVICH, A.L. (1971), Geochim. Cosmochim. Acta, Suppl. 2, 1209.

TURNER, G. (1970), Geochim. Cosmochim. Acta, Suppl. 1, 1665.

TURNER, G. (1971), Earth Planet. Sci. Letters 11, 169.

TURNER, G. (1972), Earth Planet. Sci. Letters 14, 169.

TURNER, G., J.C. HUNEKE, F.A PODOSEK and G.J. WASSERBURG (1971), Earth Planet. Sci. Letters 12, 19.

UREY, H.C. (1968), Science 162, 1408.

UREY, H.C. and G.J.F. MACDONALD (1971), Origin and history of the moon. In: Z. Kopal, ed., Physics and Astronomy of the Moon, 2nd Ed. (Academic Press, New York), 213.

WALKER, D., J. LONGHI and J.F. HAYS (1972), Geochim. Cosmochim. Acta, Suppl. 3, in press.

WASSERBURG, G.J., G.J.F. MACDONALD, F. HOYLE and W.A. FOWLER (1964), Science 143, 465.

WASSERBURG, G.J. and D.A. PAPANASTASSIOU (1971), Earth Planet. Sci. Letters 13, 97.

WISE, D.U. and M.T. YATES (1970), J. Geophys. Res. 75, 261.

WOOD, J.A. (1972), Icarus 16, 229.

WOOD, J.A., J.S. DICKEY, JR., J.B. MARVIN and B.N. POWELL (1970), Geochim. Cosmochim. Acta, Suppl. 1, 965.

WOOD, J.A., U.B. MARVIN, J.B. REID, JR., G.J. TAYLOR, J.F. BOWER, B.N. POWELL and J.S. DICKEY, JR. (1971), Smithsonian Astrophysical Observatory Special Report 333, 275 pp.

FIGURE CAPTIONS

Figure 1. Observed compressional velocity profile in the Moon (hatched lines) compared with laboratory measurements of velocity as a function of pressure in lunar (numbered) and terrestrial (named) rocks. The lunar profile is from TOKSÖZ et al. (1972a,b), where the sources of laboratory data are given in full.

Figure 2. A schematic summary of those aspects of the history of the lunar surface relevant to the questions of the constitution and evolution of the Moon's interior. Sources for this summary are given in the text. Items included near the top of the figure are well documented; entries are progressively more speculative toward the bottom.

Figure 3. The variation of some features of the Moon with average present-day uranium concentration for a family of lunar thermal history models. All models start from an initial temperature profile of TOKSÖZ et al. (1972c) and given by a model of accretion at 0°C over a 100 year time interval with an accretion rate from HANKS and ANDERSON (1969), assume Th/U = 4 and K/U = 2000 throughout

the Moon today, and include the effects of simulated convection and differentiation upon melting. The last major differentiation was at .9 b.y. after origin. Definitions of primordial core and lithosphere are given in the text. The box outlines the range of uranium concentrations that match the Apollo 15 heat flow of 33 ± 5 erg/cm^2-sec (LANGSETH et al., 1972). Circles denote the specific models which were investigated and from which the curves were drawn.

Figure 4. The variation with average present-day uranium concentration of heat flow, and dimensions of present-day lithosphere and primordial core for a suite of thermal history models starting from an initial temperature curve based on accretion at 500°C and assuming the last major differentiation to have been 1.6 b.y. after lunar origin. All other parameters and symbols are identical to those in fig. 3.

Figure 5. A model of temperature in the Moon as a function of time since lunar origin. Time, in billions of years, is indicated by the number adjacent to each profile. The initial temperature distribution is calculated from a simple model of the accretion

process (TOKSÖZ et al., 1972c); accretion at 0°C over a 100 year time span are assumed. The Moon is partially or completely molten at those depths where the temperature profile lies along the solidus of mare basalt (RINGWOOD and ESSENE, 1970). The depth range for complete melting is delimited by the small arrows above the solidus. Also shown are the Fe-FeS eutectic temperature (BRETT and BELL, 1969) and the phase boundary between feldspathic and spinel pyroxenite in the model lunar mantle composition of RINGWOOD and ESSENE (1970).

Figure 6. The extent of melting as a function of time in the thermal model of fig. 5. Heavy stippling denotes complete fusion; lighter stippling indicates partial fusion.

Figure 7. Thermal evolution in a Moon derived from inhomogeneous accretion. The initial temperature profile follows from a presumed cold (0°C) accretion over a 1000 year time interval. Primary zoning of radioactivity is assumed; see text. Other parameters and symbols are identical to those of fig. 5.

Figure 8. The extent of melting in the thermal model of fig. 7. Notation as in fig. 6.

Figure 9. Some estimates of present-day temperature in the Moon. Profile A is the final temperature curve from fig. 5. Profiles B and C are from TOKSÖZ et al. (1972c); the range of present-day temperature profiles in their models is indicated by the stippled region. Profile D is from SONETT et al. (1971). The solidus is that of mare basalt (RINGWOOD and ESSENE, 1970).

Figure 10. The variation of the moment of inertia C/MR^2 and the density ρ_3 of the mantle as a function of the density ρ_2 of the lower crust for models of the lunar density profile with homogeneous mantles. The letters A through D correspond to the temperature profiles of fig. 9. A density of 3.0 g/cm^3 is assumed (see text) for the upper crust. The shaded region indicates the limits of uncertainty in the observed moment of inertia of the Moon (KAULA, 1969).

Figure 11. The variation of density with radius in the Moon for several models with homogeneous mantles. The letters A through D correspond to the temperature profiles of fig. 9. A density of 3.0 g/cm^3

is assumed for the upper and lower crust. Shown also are the values of bulk modulus K (in Mbar) and thermal expansion α (in $10^{-5}{}^{\circ}C^{-1}$) used in conjunction with the density distribution appropriate to temperature profile B.

Figure 12. The variation of densities ρ_3 and ρ_4 of the upper and lower mantle as a function of the normalized radius of the lower mantle. Density models match the mass and moment of inertia of the Moon. Densities of 3.0 and 3.1 g/cm^3 are adopted for the upper and lower crust, respectively. The letters A through D correspond to the temperature profiles of fig. 9. Also shown are the average density of the Moon at standard conditions (arrows at lower left) for each temperature distribution and the maximum shear stress τ implied by the density inversion in the lunar mantle (see text). The dotted line is ρ_4 for profile B corrected for the effects of partial melting and solid-solid phase transformations (see text).

Figure 13. Several estimates of the temperature distribution in the shallow portions of the Moon superimposed on potentially important phase transition

boundaries. Extrapolations of the pressure-temperature boundaries for the first appearance (with increasing pressure) of garnet and the disappearance of plagioclase are shown as solid lines for Apollo 11 basalt (RINGWOOD and ESSENE, 1970) and as alternating short and long dashes for a terrestrial gabbroic anorthosite (GREEN, 1970). The range of equilibrium boundaries, also extrapolated, reported in the literature for Albite = Jadeite + Quartz (BIRCH and LE COMTE, 1960; NEWTON and KENNEDY, 1967; BOETTCHER and WYLLIE, 1968) and Anorthite = Grossularite + Kyanite + Quartz (HAYS, 1967; HARIYA and KENNEDY, 1968) are shown as stippled bands. Temperature profiles include that of SONETT et al. (1971) (dashed), the range of present-day temperatures in the models of TOKSÖZ et al. (1972c), and the range of temperatures spanned by a number of thermal history models generated to match the Apollo 15 heat flow (LANGSETH et al., 1972).

Figure 14. The effect of an iron-rich core of radius R_c on the moment of inertia C/MR^2 and the mantle density ρ_3 in two models of the Moon with homogeneous mantles. In the "optimistic" model,

the lower crust is assumed to be relatively dense (3.4 g/cm^3) and temperature curve B is adopted. In the "pessimistic" model, a lower crustal density of 3.0 g/cm^3 and temperature profile D are used.

Figure 15. The effect of K^{40} in an Fe-FeS core on thermal history. (a) Temperature evolution in an initially molten Moon with average U concentration = 11 ppb, Th/U = 4 and K/U = 2000 at present. (b) Temperature evolution in a Moon similar to (a) except that K/U = 80,000 in the bulk Moon, but K/U = 2000 everywhere except in a core of radius R_c = .2R.

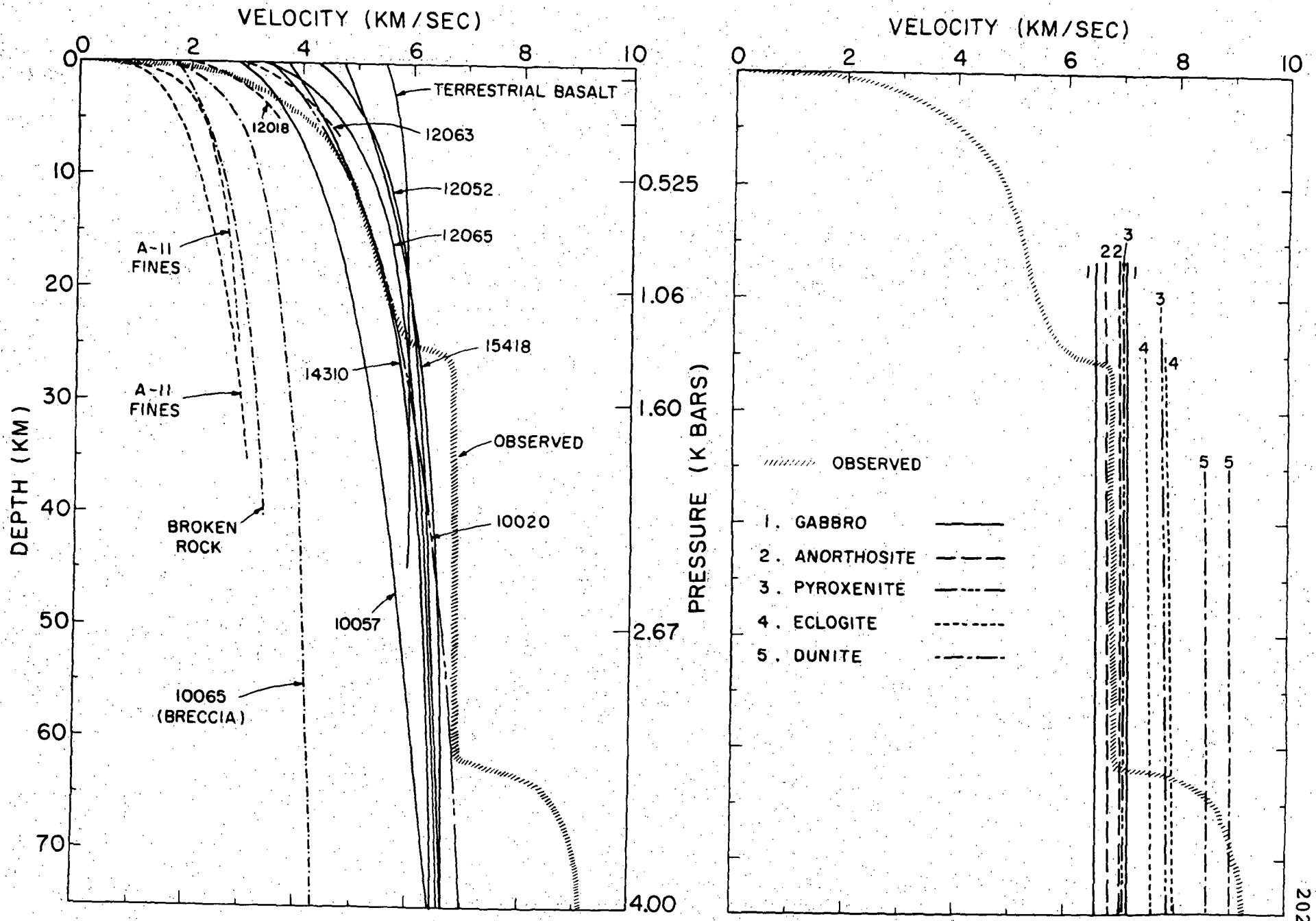
VELOCITY (KM/SEC)
0
2
4
6
8
10
DEPTH (KM)
10
20
30
40
50
60
70
PRESSURE (K BARS)
0.525
1.06
1.60
2.67
4.00
TERRESTRIAL BASALT
12018
12063
12052
12065
15418
14310
OBSERVED
10020
10057
10065
(BRECCIA)
A-11
FINES
A-11
FINES
BROKEN
ROCK
VELOCITY (KM/SEC)
OBSERVED
1. GABBRO
2. ANORTHOSITE
3. PYROXENITE
4. ECLOGITE
5. DUNITE
202

Figure 1

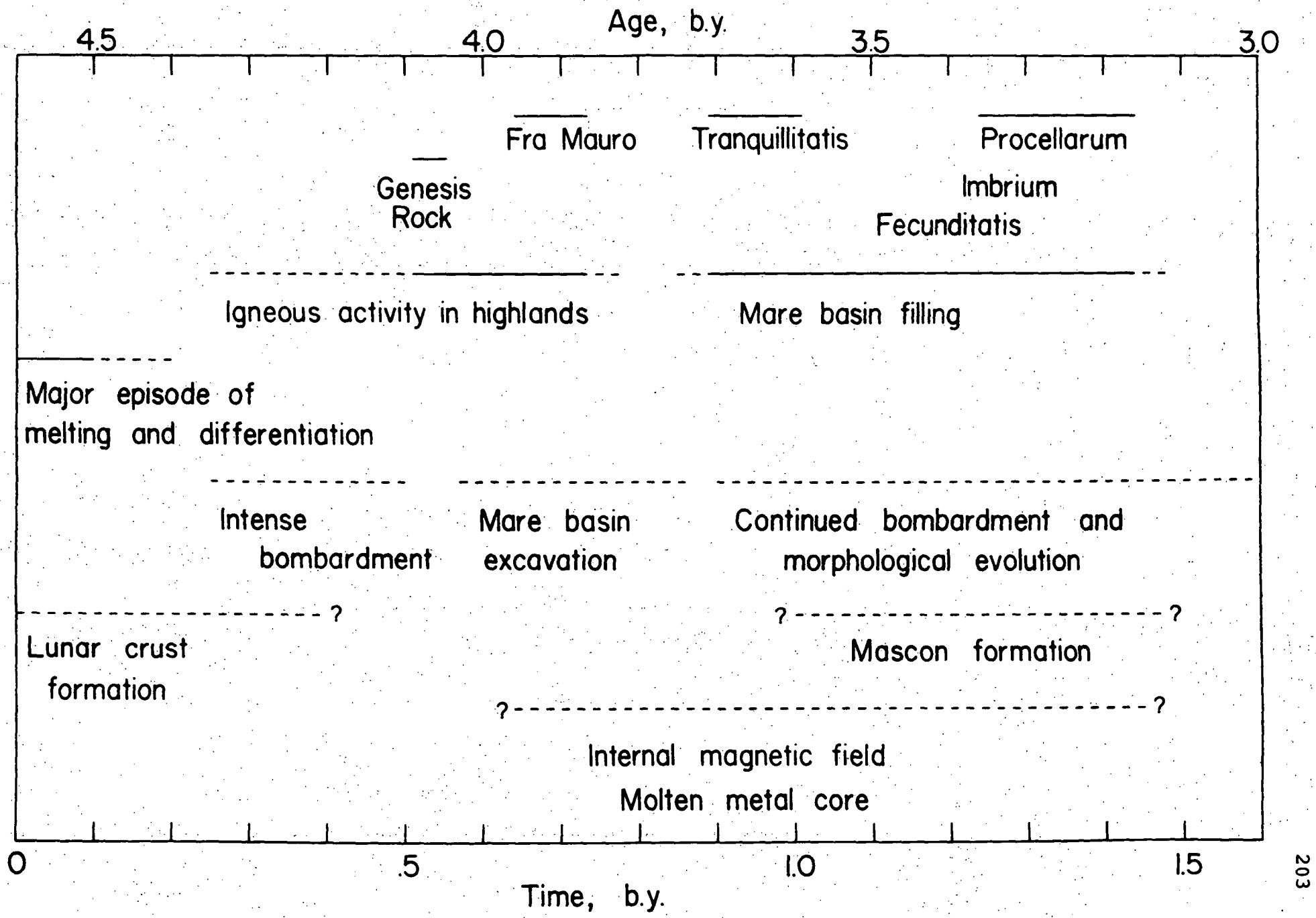
Age, b.y.
4.5
4.0
3.5
3.0
Fra Mauro
Tranquillitatis
Procellarum
Genesis Rock
Imbrium
Fecunditatis
Igneous activity in highlands
Mare basin filling
Major episode of melting and differentiation
Intense bombardment
Mare basin excavation
Continued bombardment and morphological evolution
Lunar crust formation
Mascon formation
Internal magnetic field
Molten metal core
0
.5
1.0
1.5
Time, b.y.

Figure 2

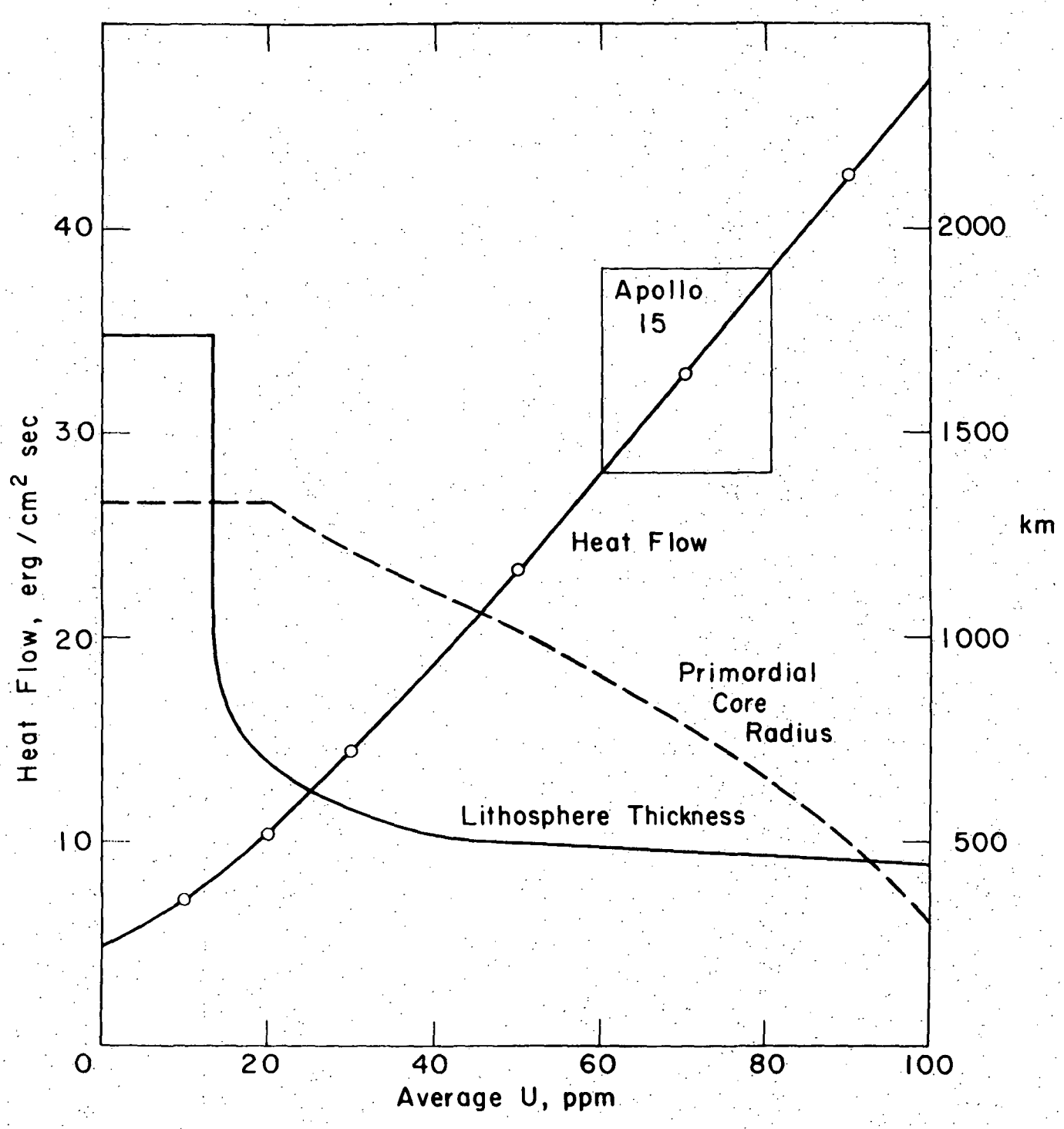
Heat Flow, erg/cm² sec
40
30
20
10
0
20
40
60
80
100
Average U, ppm
2000
1500
1000
500
km
Apollo
15
Heat Flow
Primordial
Core
Radius
Lithosphere Thickness

Figure 3

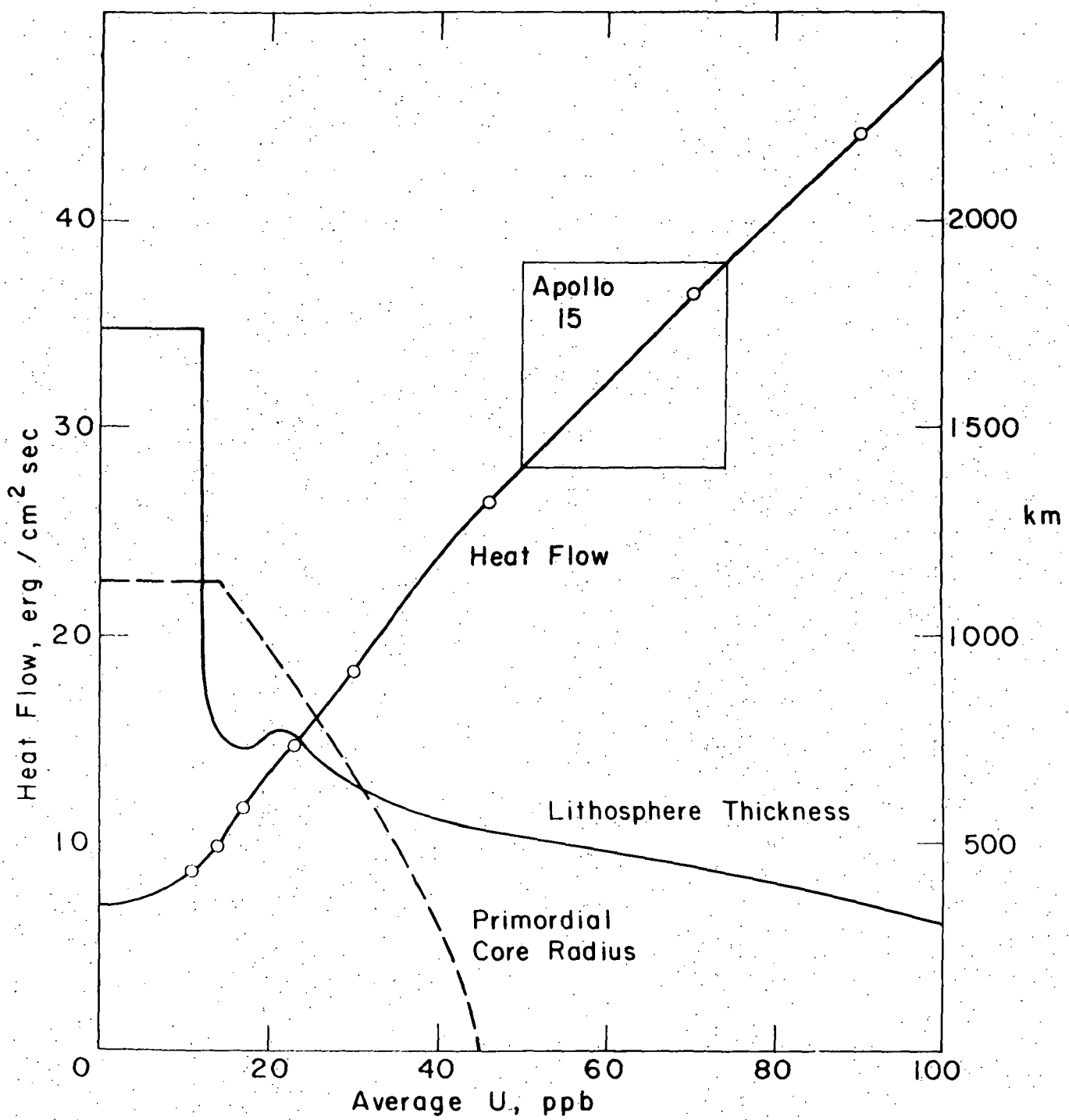
Apollo
15
Heat Flow
Lithosphere Thickness
Primordial
Core Radius
Heat Flow, erg / cm² sec
km
Average U, ppb
0
10
20
30
40
500
1000
1500
2000
0
20
40
60
80
100

Figure 4

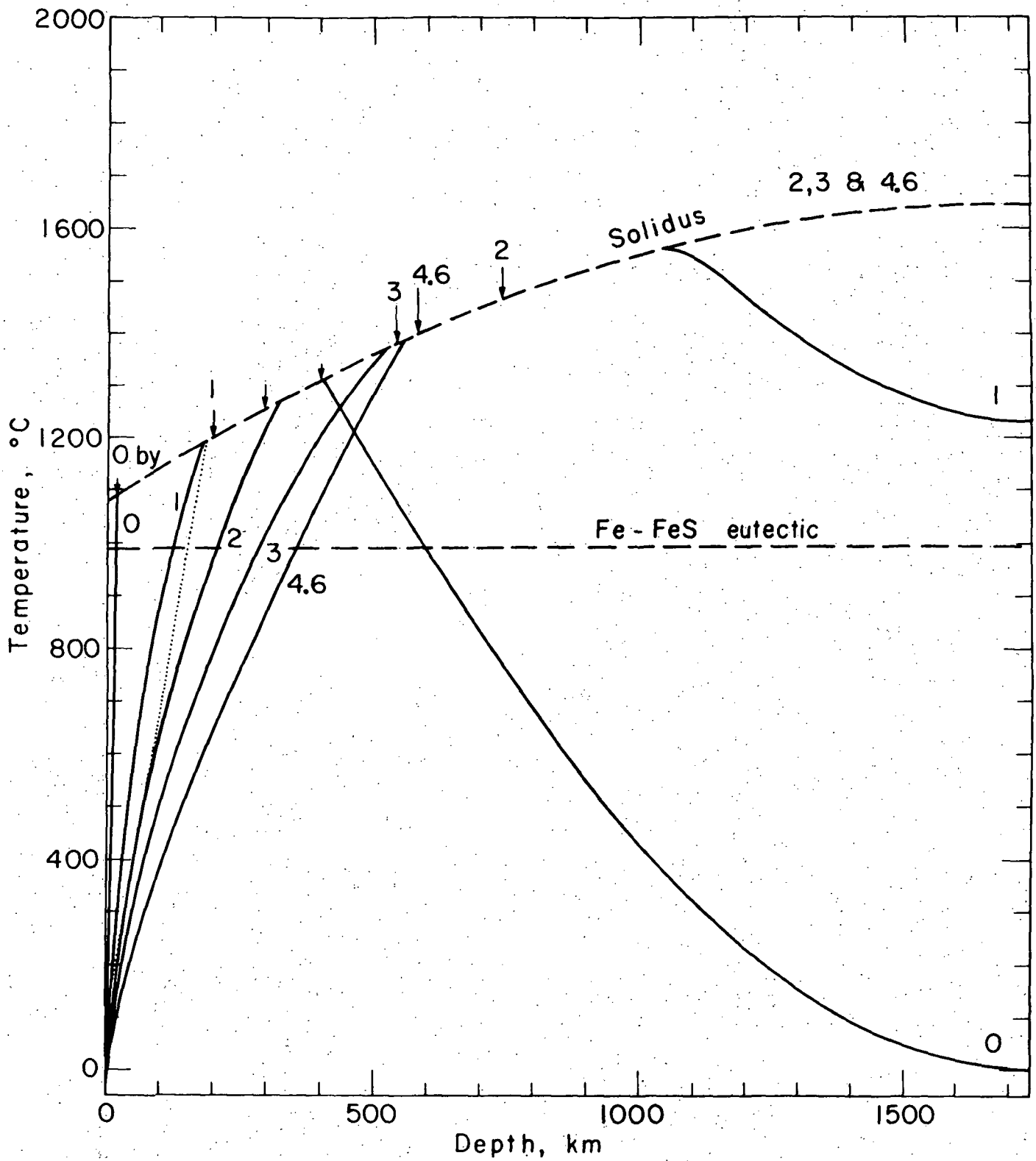
2000
1600
1200
800
400
0
Temperature, °C
0
500
1000
1500
Depth, km
2,3 & 4.6
Solidus
Fe - FeS eutectic
0 by
0
1
2
3
4.6
1
2
3
4.6
1
0

Figure 5

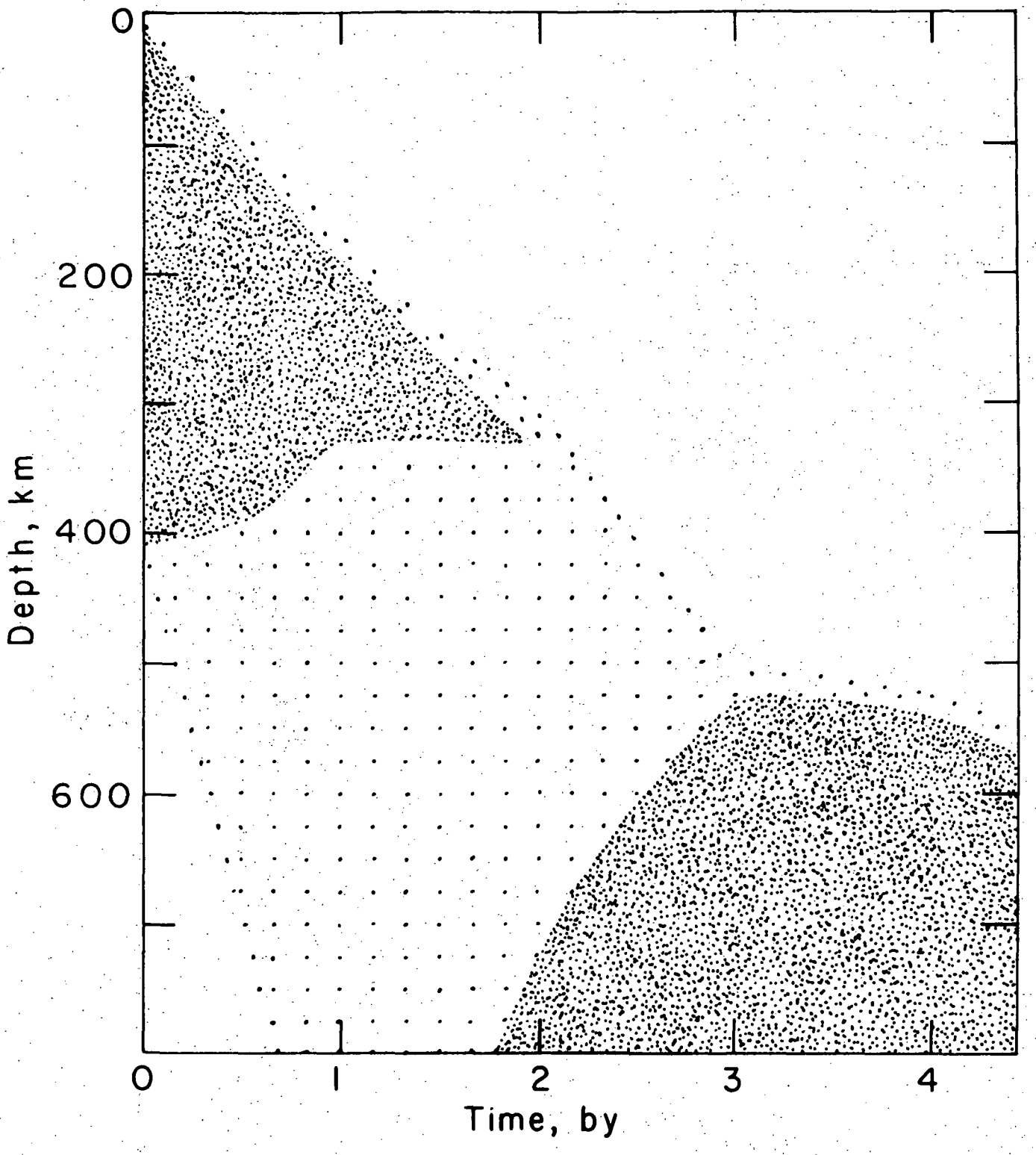

Figure 6

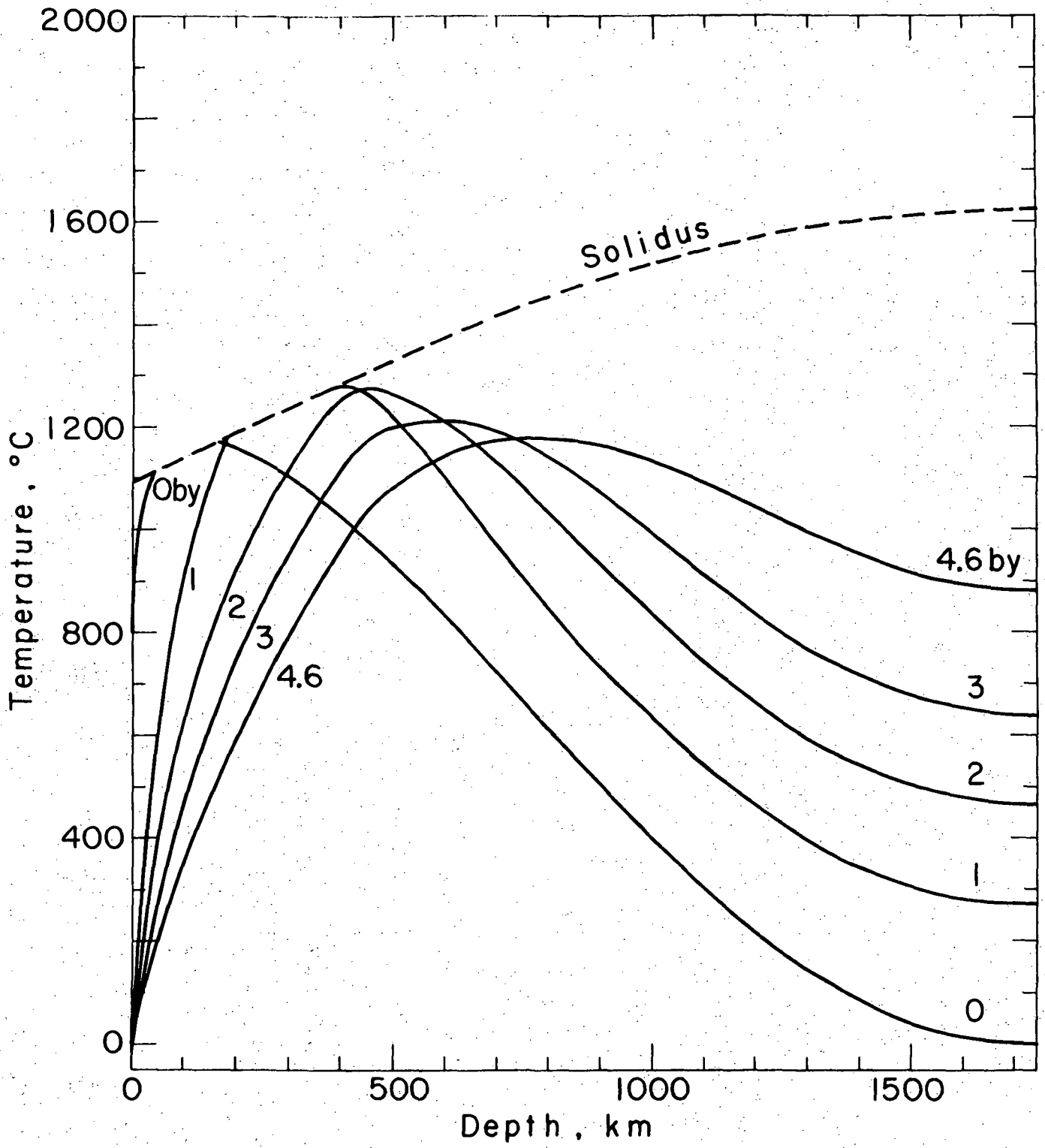
2000
1600
1200
800
400
0
Temperature, °C
0
500
1000
1500
Depth, km
Solidus
Oby
1
2
3
4.6
4.6by
3
2
1
0

Figure 7

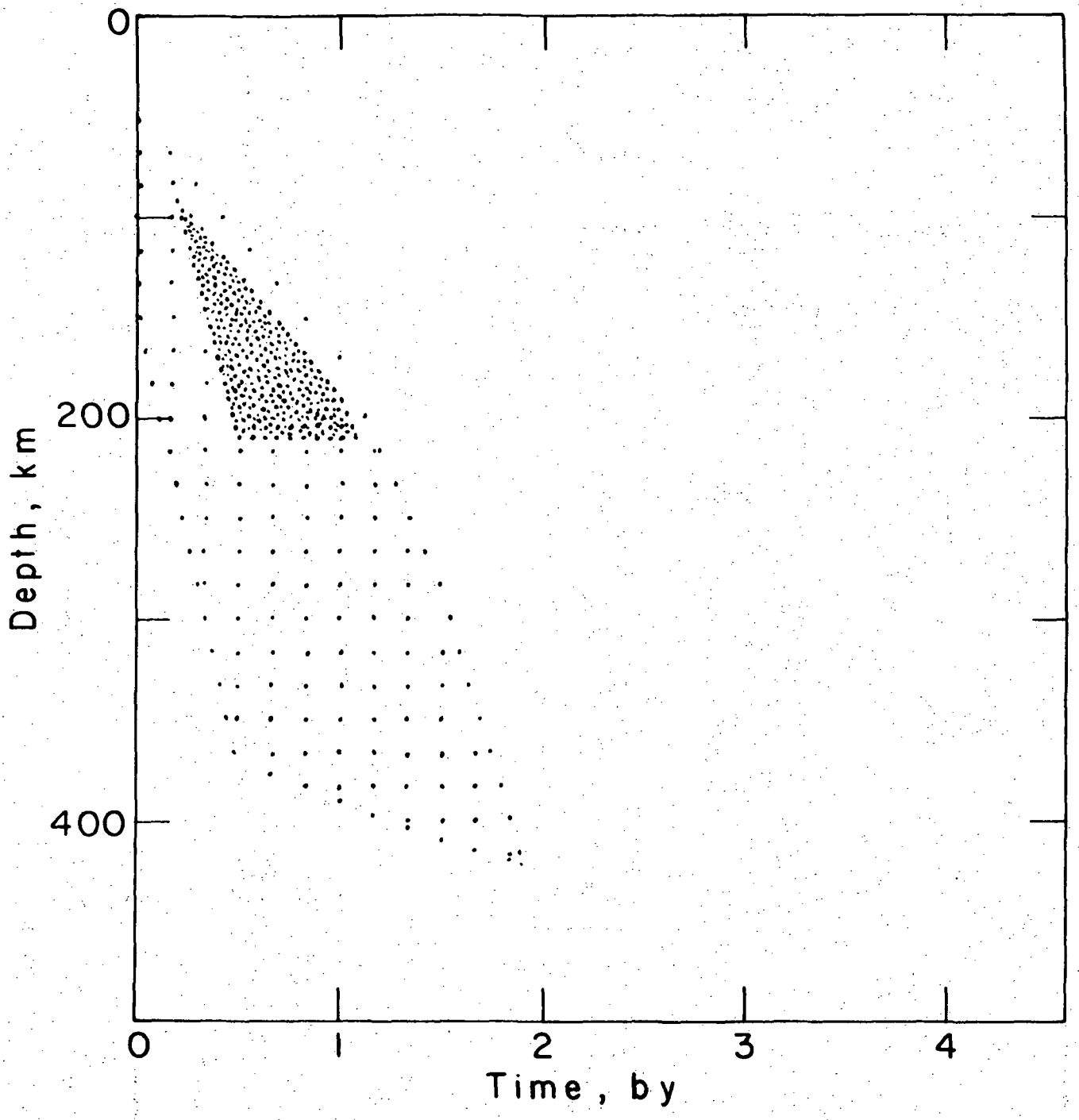

Figure 8

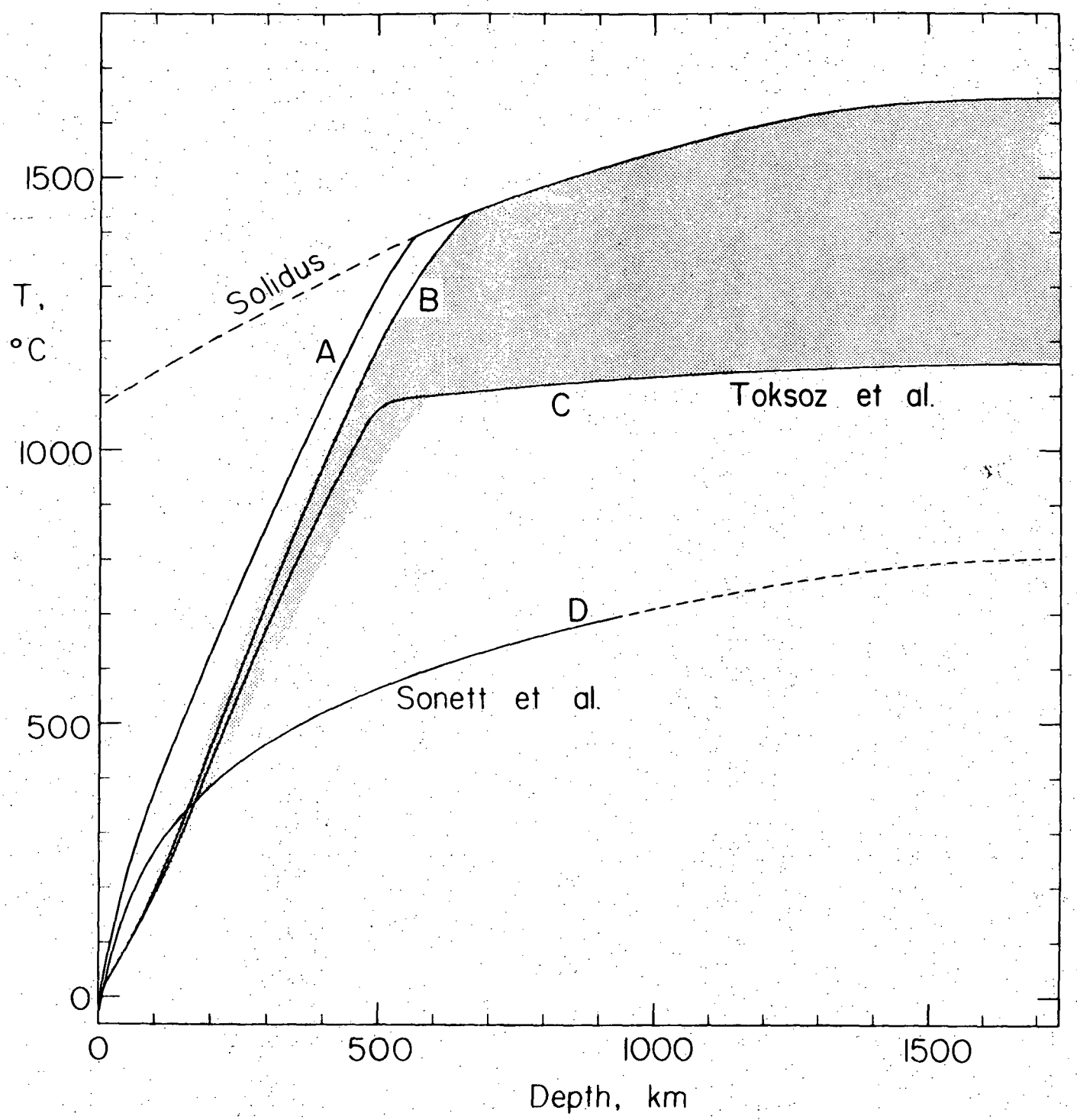
1500
1000
500
0
T,
°C
Solidus
A
B
C
Toksoz et al.
D
Sonett et al.
0
500
1000
1500
Depth, km

Figure 9

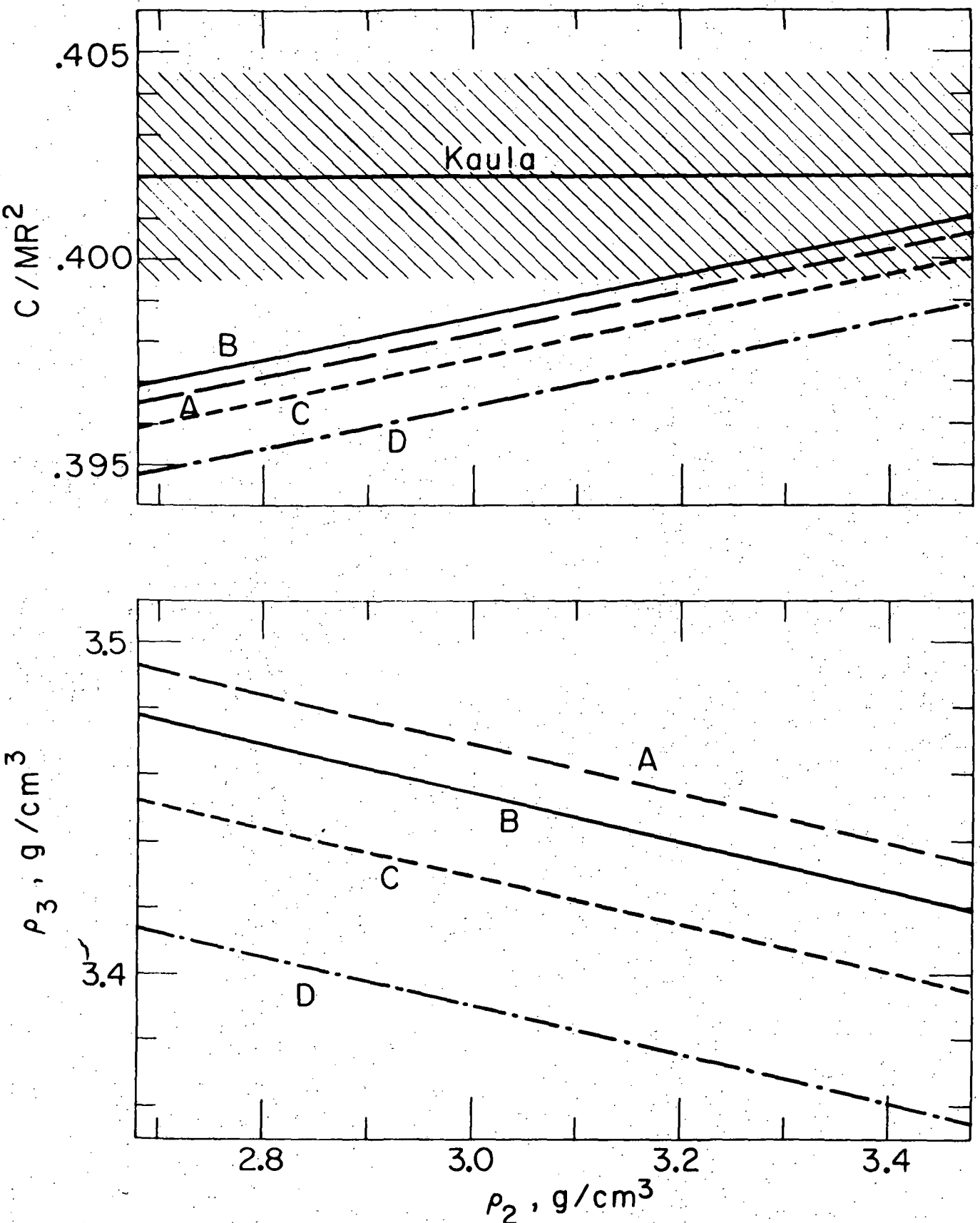
.405
.400
.395
C/MR²
Kaula
B
A
C
D
3.5
3.4
ρ₃, g/cm³
A
B
C
D
2.8
3.0
3.2
3.4
ρ₂, g/cm³

Figure 10

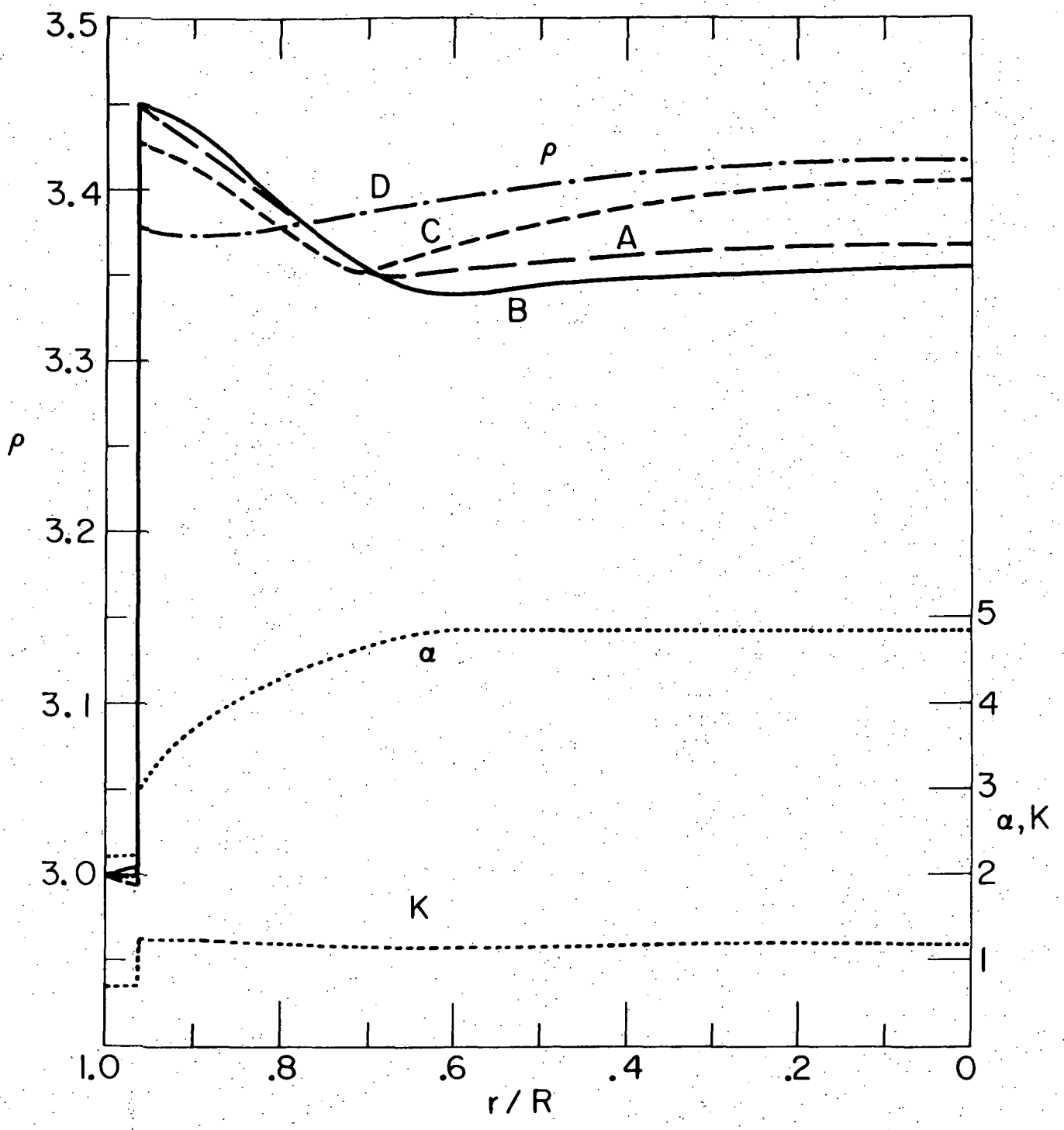

Figure 11

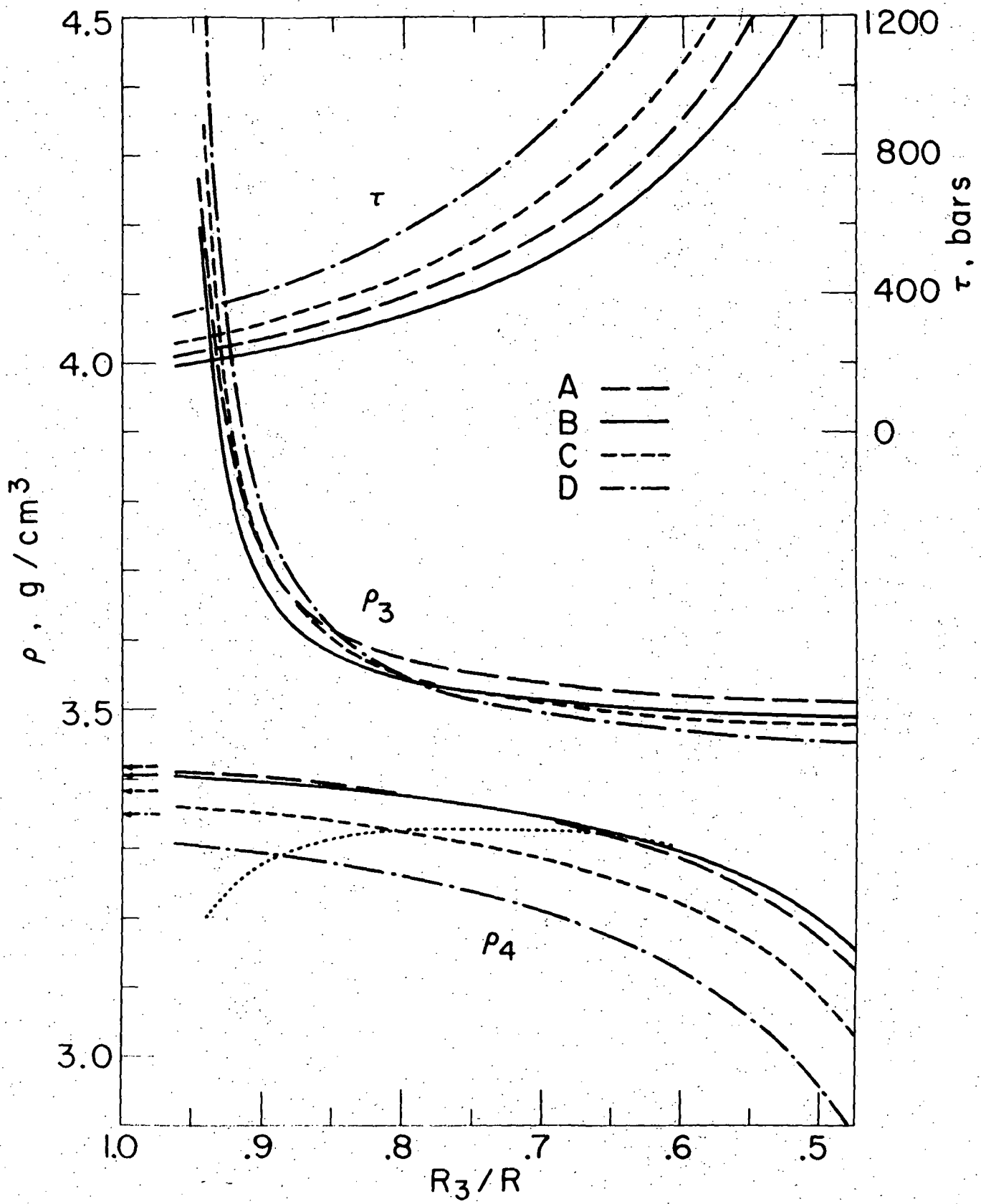

Figure 12

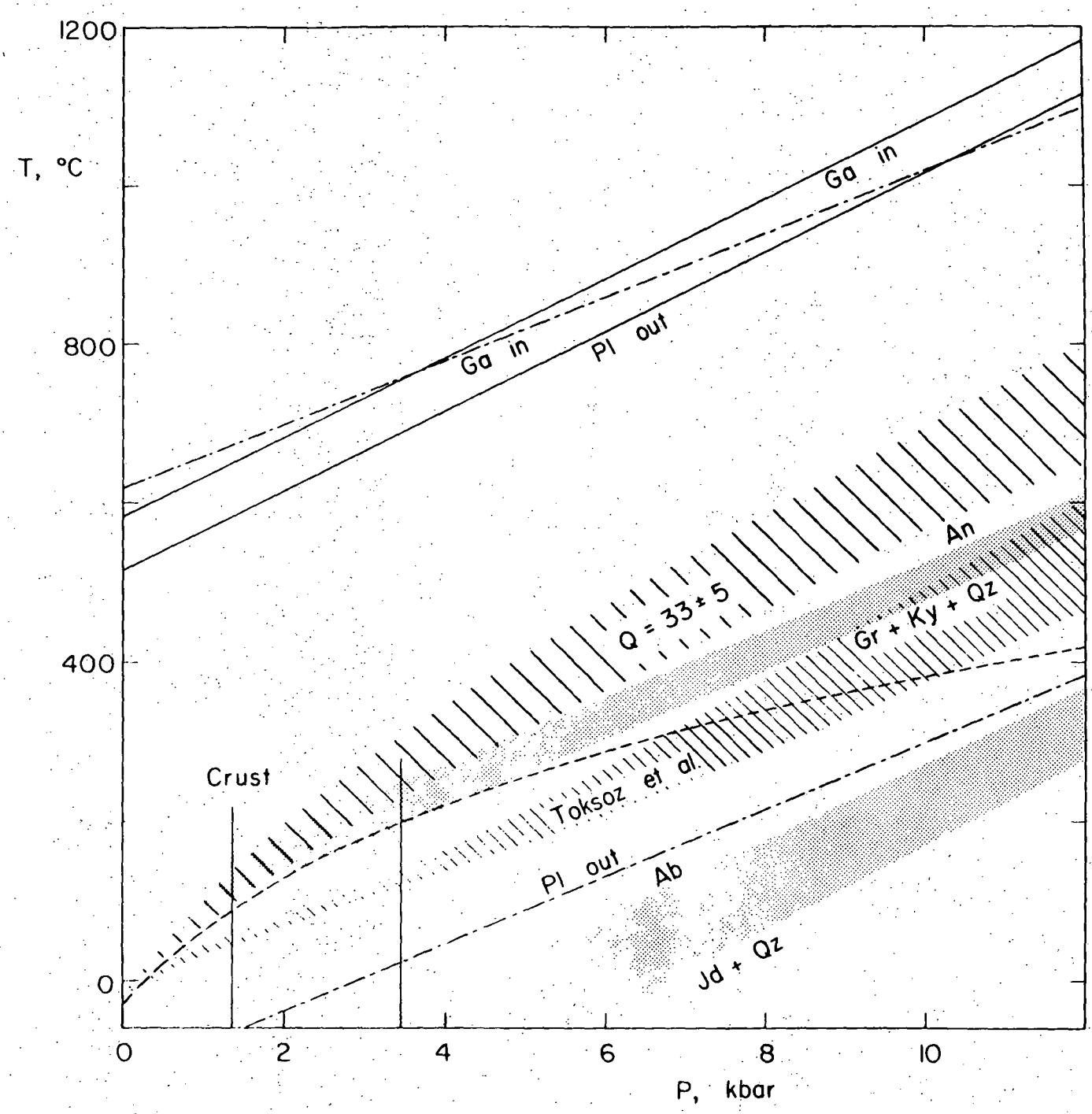
1200
800
400
0
T, °C
0
2
4
6
8
10
P, kbar
Ga in
Ga in
Pl out
Q = 33 ± 5
An
Gr + Ky + Qz
Crust
Toksoz et al.
Pl out
Ab
Jd + Qz

Figure 13

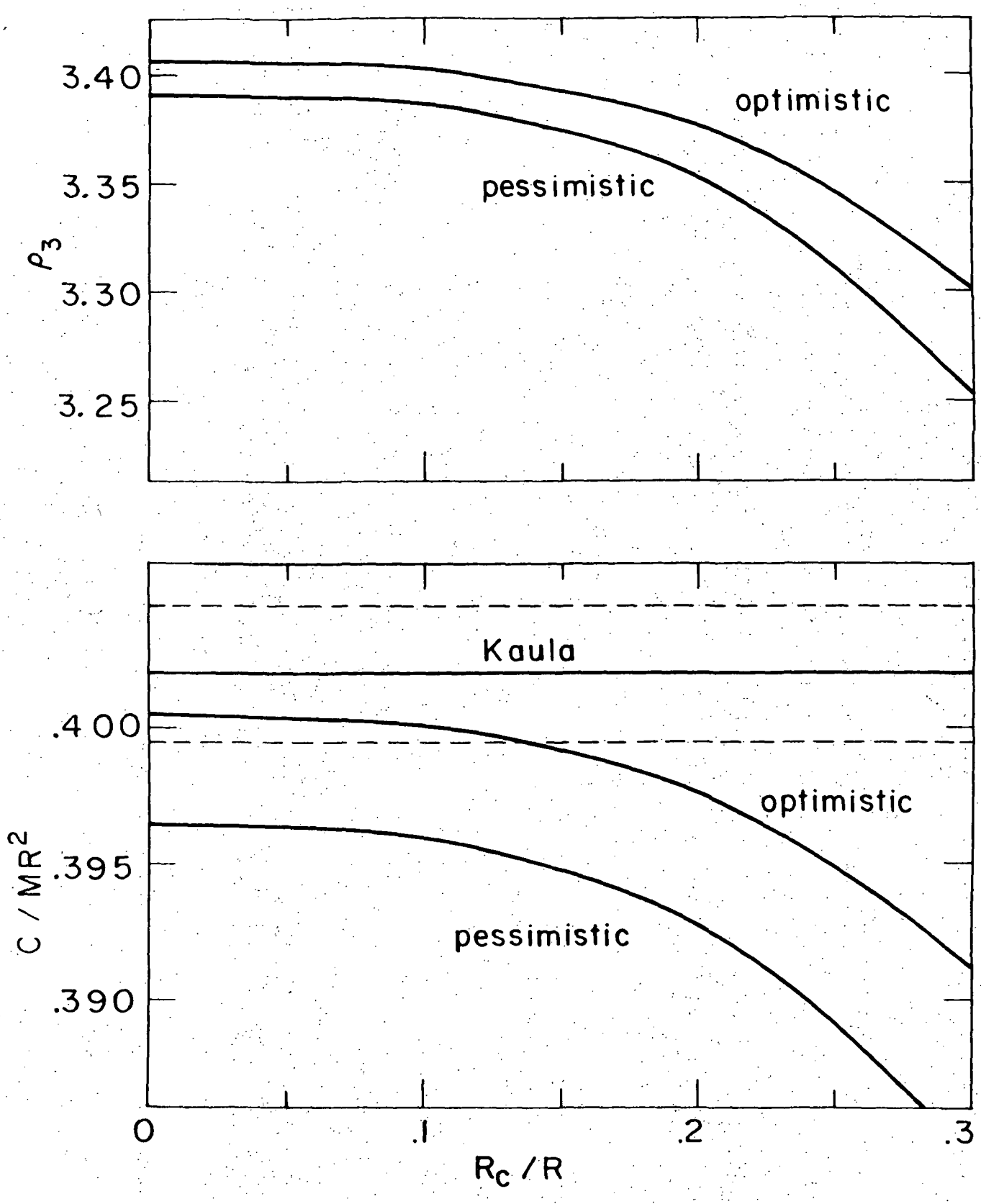
3.40
3.35
3.30
3.25
ρ_3
optimistic
pessimistic
Kaula
.400
.395
.390
C / MR^2
optimistic
pessimistic
0
.1
.2
.3
R_c / R

Figure 14

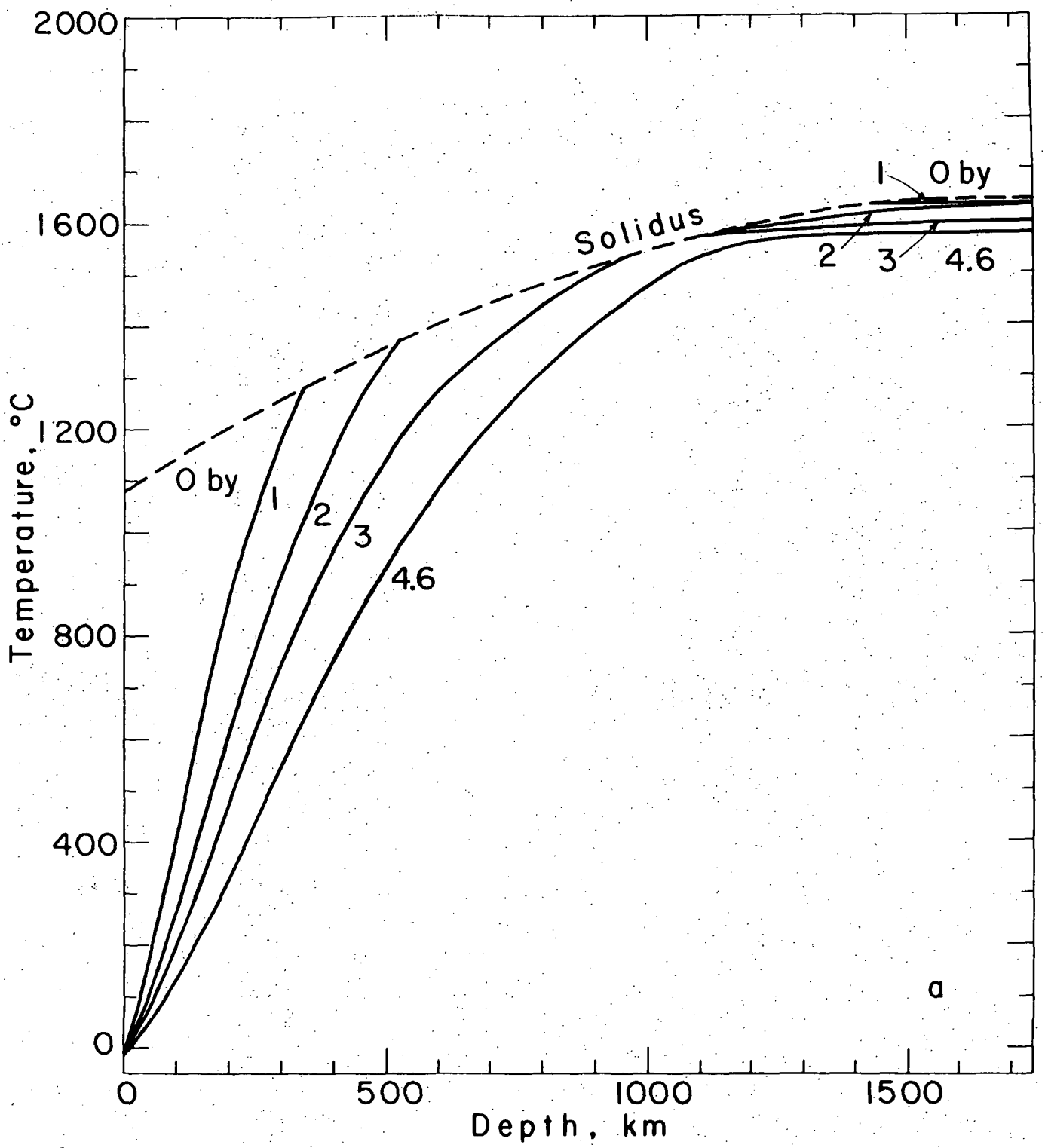
2000
1600
1200
800
400
0
Temperature, °C
0
500
1000
1500
Depth, km
Solidus
0 by
1
2
3
4.6
a

Figure 15a

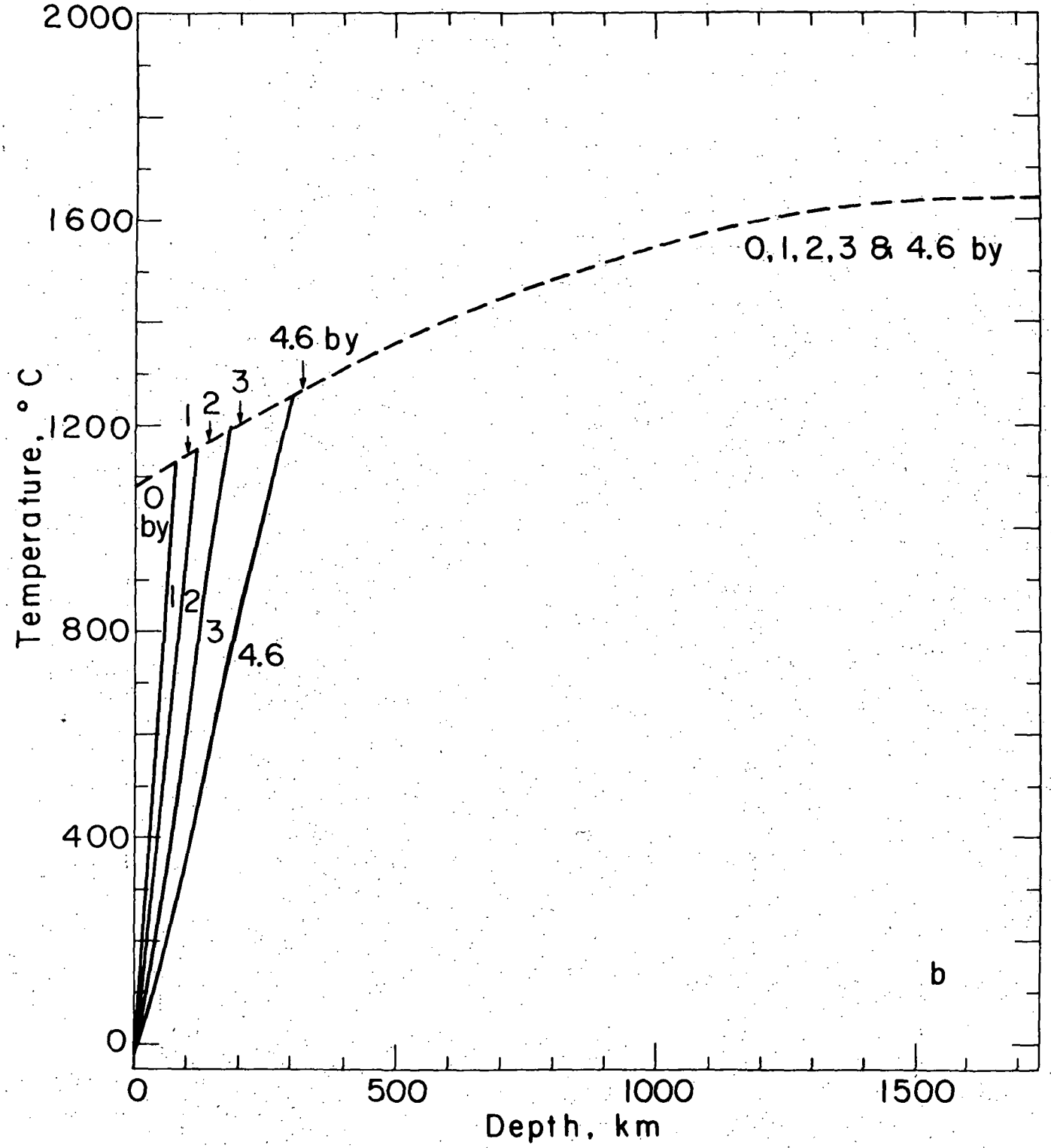
2000
1600
1200
800
400
0
Temperature, °C
0
500
1000
1500
Depth, km
0,1,2,3 & 4.6 by
4.6 by
3
2
1
0 by
1
2
3
4.6
b

Figure 15b